UNIVERSITY OF OKLAHOMA

GRADUATE COLLEGE

SEISMIC DATA MULTI-SPECTRAL ANALYSIS, ATTENUATION ESTIMATION AND SEISMIC SEQUENCE STRATIGRAPHY ENHANCEMENT APPLIED TO CONVENTIONAL AND UNCONVENTIONAL RESERVOIRS

A DISSERTATION

SUBMITTED TO THE GRADUATE FACULTY

in partial fulfillment of the requirements for the

Degree of

DOCTOR OF PHILOSOPHY

By

FANGYU LI
Norman, Oklahoma
2017

SEISMIC DATA MULTI-SPECTRAL ANALYSIS, ATTENUATION ESTIMATION AND SEISMIC SEQUENCE STRATIGRAPHY ENHANCEMENT APPLIED TO CONVENTIONAL AND UNCONVENTIONAL RESERVOIRS

A DISSERTATION APPROVED FOR THE
CONOCOPHILLIPS SCHOOL OF GEOLOGY AND GEOPHYSICS

BY

_____
Dr. Kurt J. Marfurt, Chair

_____
Dr. Xingru Wu

_____
Dr. Norimitsu Nakata

_____
Dr. Xiaowei Chen

_____
Dr. Oswaldo Davogustto

© Copyright by FANGYU LI 2017
All Rights Reserved.

To my wife Mingyang Liu

You are my Rock.

ACKNOWLEDGMENTS

A PhD is never a gift from others, but that requires struggling. Earning the "Dr." title has been the objective of the past four years of my life, although many benefits have occurred along the way. I have obtained deeper understanding, curiosity, creativity, perseverance, tenacity, and motivation. From the bottom of my heart, I sincerely acknowledge those who have been my faithful and reliable companions during this wonderful journey.

I would like to express the deepest appreciation to my PhD advisor, the committee chair, Dr. Kurt Marfurt, who has guided me to explore the world of Geophysics and always been supportive and encouraging not only for my research but also for my future career. I could not expect a better advisor, who has an everlasting passion to research, respects his students as friends, shares his sense of humor to boost morale, and is always patient. I am so proud to be a student of Dr. Marfurt, who will always be an idol for my future life.

I also want to express my sincere gratitude to my committee members: Dr. Xingru Wu, Dr. Nori Nakata, Dr. Xiaowei Chen, and Dr. Oswaldo Davogustto for their insightful comments and encouragement. Dr. Chen is an expert in global geophysics, and she taught me seismology, which improves my understandings of passive seismic processing and analysis. I would like to thank Dr. Nakata for agreeing to be my committee member. Without his support, the whole process would be more challenging, his insightful ideas help guide my research. Dr. Davogustto provided suggestions not only for my research, but also insights into planning my career and balancing my life. I deeply appreciate his time and effort. Dr. Wu is an expert in petroleum enginerring, and contributes his

perspective to the committee. He is a professional from whom I have learned a lot. It is my honor to have them all on my committee.

I want to express my thanks to all the teammates of the Attribute Assisted Seismic Processing and Interpretation (AASPI) consortium for their supports: Bo Zhang, Shiguang Guo, Tao Zhao, Tengfei Lin, Huailai Zhou, Bin Lyu, Xuan Qi, Sumit Verma, Bradley Wallet, Marcus Cahoj, Gabriel Machado, Abdulmohsen AlAli, Lennon Infante, Thang Ha, Bryce Hutchinson, Olanrewaju Aboaba, Murphy Cassel, Megan Gunther, Robert Hardisty, David Lubo Robles, Rafael Pires de Lima, Saurabh Sinha, Swetal Patel, Yuji Kim, Sean O'Bleness, and many others whose names are not listed. Especially, I want to appreciate all the co-authors of my conference abstracts and journal papers, without whom the things I have accomplished would be more limited.

I also want to thank the entire staff of ConocoPhillips School of Geology and Geophysics (CPSGG): Rebecca Fay, Ginny Gandy-Guedes, Ginger Leivas, Leah Moser, Amber Roberts, Donna S. Mullins, Nancy Leonard, Teresa Hackney, Wei Wang and Jocelyn Cook for their help and supports.

I thank my parents for everything they have done for me. Finally, I want to thank my wife, Mingyang Liu. She has always been encouraging and supportive throughout my PhD studies and in my life in general.

TABLE OF CONTENTS

LIST OF TABLES

LIST OF FIGURES

ABSTRACT

Seismic data are an essential resource for interpretation, providing abundant information about geological structures, sedimentation, stratigraphy and reservoir quality. Geophysicists have dedicated tremendous efforts in fully utilizing the information content in seismic data.

Time series analysis and frequency (spectral) analysis are the two most common tools used to characterize seismic data. Multi-spectral analysis highlights geological features at different scales. The spectral sensitivity is not only from the tuning effects, but also from the geological structures and rock properties, including attenuation. To analyze the additional information in the spectral components rather than in the broad-band data, I begin by examining the spectrally limited coherence responses of multiple stages of incised valleys of Red Fork formation, Anadarko Basin, Oklahoma. Later, I combine covariance matrices for each spectral component, add them together, and compute multi-spectral coherence images.

Spectral ratio and frequency shift methods are traditional attenuation estimation methods. However, the assumptions of each method introduce errors and instabilities into the results. I propose a modified frequency shift method to estimate attenuation (the reciprocal of the quality factor, Q), that relaxes some of these assumptions. Synthetic and field applications show robust and accurate results. Thin-bed layering also modifies the spectra, causing simple attenuation estimation to be inaccurate. To address this limitation, I use well logs based impedance inversion results to calculate a spectral correction for elastic variability in the spectra prior to estimating the inelastic attenuation contribution. The spectral correction can be viewed as a pre-conditioning step, following which both spectral ratio and frequency shift methods can produce better results.

Traditional attenuation estimation methods work well in high porosity and high permeability gas sands. However, the well accepted squirt model does not apply to low permeability shale reservoirs. Rather, micro-cracks generate strong geometric or scattering attenuation, which combined with the intrinsic attenuation produced by TOC (total organic carbon) result in complicated spectral responses. Rather than estimating *Q*, I evaluate a suite of attenuation attributes. Even though the mechanism underlying may be unknown, these attenuation attributes can be statistically linked to the production and geology.

Using the classic Fourier transform, the available spectral band often falls between 10 and 80 Hz. Nevertheless, interpreters observe lower frequency patterns in the data, for example, a 200 ms thick (5 Hz) pattern of low reflectivity sandstone and a 400 ms thick (2.5 Hz) pattern of high reflectivity responses (e.g. sabkhas or cyclothems). I introduce an adaptive intrinsic mode decomposition method called variational mode decomposition to analyze the "rhythm" in the seismic data. The intrinsic modes are defined as combinations of AM modulated signals, which are analyzed in the frequency domain with carrier frequencies (that fall within the 10-80 Hz limit), to characterize the buried stratigraphy information seen in the longer wavelength patterns. Because intrinsic modes are able to model seismic signals, but unable to model the noise component, the random noise lies within the residual of the intrinsic mode decomposition. Unlike filtering methods with predefined parameters, I develop a fully data-driven denoising method to suppress random noise, thereby enhancing the data quality.

CHAPTER 1
MULTI-SPECTRAL ANALYSIS[1]

ABSTRACT

Seismic coherence is routinely used to delineate geologic features that might otherwise be overlooked in conventional seismic amplitude volumes. In general, one wishes to interpret the most broadband data possible. However, because of the thickness tuning effects, certain spectral components often better illuminate a given feature with higher signal-to-noise ratio than others. Clear images of channels and other stratigraphic features that may be buried in the broad-band data may "light up" at certain spectral components. For the same reason, coherence attributes computed from spectral voice components (equivalent to a filter bank) also often provide sharper images, with the "best" component being a function of the tuning thickness and the reflector alignment across faults. While one can co-render three coherence images using RGB blending, a display of the information contained in more than three volumes in a single image is difficult. I address this problem by summing a suite of structure-oriented covariance matrices computed from spectral voices resulting in a "multi-spectral" coherence algorithm.

I demonstrate the value of multi-spectral coherence by comparing it to both RGB blended volumes and the coherence computed from spectrally balanced, broad-band seismic amplitude volume from a mega−merge survey acquired over the Red Fork

---

[1]*The first part of this chapter is published as - Li, F., J. Qi, , and K.J. Marfurt, 2015, Attribute mapping of variable-thickness incised valley-fill systems: The Leading Edge, **34**(1), 48-52. The second part of this chapter has been submitted for publication in Interpretation.*

Formation of the Anadarko Basin, Oklahoma. The multi-spectral coherence images provide better images of channel incisement and are less noisy than those computed from the broad-band data. Multi-spectral coherence also provides several advantages over RGB blended volumes: first, one can combine the information content from more than three spectral voices; second, only one volume needs to be loaded into the workstation; and third, the resulting gray-scale images can be co-rendered with other attributes of interest, for example, petrophysics parameters, plotted against a polychromatic color bar.

INTRODUCTION

Twenty years after its inception in the mid-1990s, seismic coherence volumes are routinely used to delineate structural and stratigraphic discontinuities such as channels, faults and fractures, to highlight incoherent zones such as karst collapse and mass transport complexes, and to identify subtle tectonic and sedimentary features that might otherwise be overlooked on conventional amplitude volumes (Ogiesoba and Hart, 2009; Sun et al., 2010; Li et al., 2015; Qi et al., 2017). Estimates of seismic coherence (Bahorich and Farmer, 1995; Marfurt et al., 1998; Gersztenkorn and Marfurt, 1999; Lu et al., 2005; Wu, 2017; Yan et al., 2017) that highlight changes in seismic waveform or amplitude across a discontinuity provide quantitative measures of the geological discontinuity.

In general, the quality of a coherence image is a direct function of the quality of the seismic amplitude from which it is computed. For this reason, the most important step in coherence computation is to ensure that the processed data exhibit high bandwidth, are accurately imaged, and are free of multiples and other types of coherent noise. Once in the interpreter's hands, many seismic amplitude volumes benefit from subsequent post-stack structure-oriented filtering and spectral balancing (Chopra and Marfurt, 2007).

The broad-band seismic response of a given geological feature is composed of its response of its constituent spectral bands. However, such boundaries and edges computed from broad-band seismic data does not give a measure of the vertical scale of the discontinuity. Through constructive and destructive interference, the resulting vertical and horizon slices often represent the response of the strongest, or dominant frequency corresponding to the structure and stratigraphy of given time tuning thickness in the analysis window.

Spectral decomposition methods transform a 1D seismic amplitude trace into 2D time-frequency spectral magnitude and phase components (Partyka et al., 1999). Certain spectral components will exhibit a higher signal-to-noise ratio than others. In addition, thin beds that are tuned might be expected to better exhibit discontinuities at their higher amplitude tuning frequency than at other frequencies (Peyton et al., 1998). For the same reason, spectral attributes of relatively narrow band components often delineate anomalous geological features that are otherwise buried within the broad-band seismic response.

Not all spectral components contain signal, while others may be overly contaminated by noise. For example, Fahmy et al. (2005) recognized that a deep reservoir tuned at 11 Hz was masked by strong, higher-frequency multiples. By simply removing this high frequency components they could obtain a clear image of the reservoir and perform an accurate AVO analysis. Gao (2013) noticed that subtler structural details in reservoirs are revealed using a higher frequency wavelet as the spectral probe. Abele and Roden (2005) found that the curvature computed at certain spectral components better correlated to microseismic events than others. Sun et al. (2010) used discrete frequency coherence cubes in fracture detection and found that high frequency components can provide greater details.

Recently, Li and Lu (2014) showed that coherence computed from different spectral components can be combined to provide a qualitative measure of the scale of geological discontinuities such as faults, channels, caves, and collapse features. I propose a multi-spectral coherence method to map variations of thickness and edges to map the different stage fills of incised valley system. I use RGB color blending technique to

integrate attributes computed at different spectral components. The data volume is part of mega-merge survey from CGGVeritas over the Anadarko Basin, Oklahoma, and incorporates a survey which was one of the first applications of spectral decomposition interpreted by Peyton et al. (1998) using 36 Hz spectral component and full band coherence. While my analysis of mega-merge survey corresponds well with the original incised valley interpretation, the improved data quality due to the surface consistent deconvolution and statics as well as the larger migration aperture results in much sharper channel images.

METHODOLOGY

The Covariance Matrix and Energy Ratio Coherence

Gersztenkorn and Marfurt (1999) describe the first implementation of coherence based on the eigenvectors of the covariance matrix. Since then, several details have been modified, including computing the covariance matrix, **C**, from the analytic trace, composed of the original data, **d**, and its Hilbert transform, $\mathbf{d^H}$ along structural dip:

$$C_{mn} = \sum_{k=-K}^{K}\left[d(t_k, x_m, y_m)d(t_k, x_n, y_n) + d^H(t_k, x_m, y_m)d^H(t_k, x_n, y_n)\right], \qquad (1.1)$$

where t_k is the time of a structurally interpolated sample at a distance (x_m,y_m) to the analysis point at $(x=0, y=0,t=0)$. Computing the eigenvectors of **C** provides a means of computing a Karhunen-Loève filtered version of the data, $\mathbf{d_{KL}}$ and $\mathbf{d^H_{KL}}$. If the data **d** have been previously spectrally balanced, the broadband energy ratio coherence (Chopra and Marfurt, 2007), s_{bb}, can then be defined as

$$s_{bb} = \frac{\sum_{m=1}^{M}\sum_{k=-K}^{K}\left\{\left[d_{KL}(t_k, x_m, y_m)\right]^2 + \left[d_{KL}^H(t_k, x_m, y_m)\right]^2\right\}}{\sum_{m=1}^{M}\sum_{k=-K}^{K}\left\{\left[d(t_k, x_m, y_m)\right]^2 + \left[d^H(t_k, x_m, y_m)\right]^2\right\}}. \quad (1.2)$$

Filter Banks and Spectral Decomposition

Hardage (2009) recognized that because of the variable signal-to-noise ratio at different frequencies, that faults were more easily identified in his data on the low frequency components that were less contaminated by strong interbed multiples. The continuous wavelet transform can be viewed as the application of a suite of filter banks to the original seismic data. Li and Lu (2014) and Honorio et al. (2016) computed coherence from a suite of spectral components and combined them using RGB color blending, resulting in not only improved discontinuity images, but also an estimate at which spectral bands the discontinuities occurred. The main limitation of this approach is that only three spectral components can be co-rendered at any one time.

To address this limitation, Dewett and Henza (2015) combined multiple coherence attributes images using self-organizing maps. Each energy-ratio coherence volume was computed along structure from spectral voices, **u(f):**

$$u(f_l, t_k, x_m, y_m) = a(f_l, t_k, x_m, y_m)\exp[i\varphi(f_l, t_k, x_m, y_m)], \quad (1.3)$$

which is constructed using a spectral decomposition algorithm, where **a** is the spectral magnitude and **φ** the spectral phase of each component.

Sui et al. (2015) also noted the value of multispectral coherence and 3-component limitations of RGB display, and computed coherence based on spectral magnitudes, $a(f_l,t_k,x_m,y_m)$, using the covariance matrix

$$C_{mn} = \sum_{l=1}^{L}\sum_{k=-K}^{K}\left[a(f_l, t_k, x_m, y_m)a(f_l, t_k, x_n, y_n)\right]. \quad (1.4)$$

By not using the phase component, the covariance matrix is less sensitive to dip, allowing the use of a simpler, non-structure-oriented computation.

I build on the above work, but rather than use the spectral magnitude computed along time slices used in Equation 1.4, I use the spectral voices and their Hilbert transforms computed along structure described by Equation 1.3 to obtain the covariance matrix (Marfurt, 2017):

$$C_{mn} = \sum_{l=1}^{L} \sum_{k=-K}^{K} \begin{bmatrix} u(t_k, f_l, x_m, y_m)u(t_k, f_l, x_n, y_n) \\ +u^H(t_k, f_l, x_m, y_m)u^H(t_k, f_l, x_n, y_n) \end{bmatrix}. \quad (1.5)$$

I will then compute coherence from the original broad-band data, from each spectral voice component, and compare them to the multispectral coherence computed using Equation 1.5.

DATA DESCRIPTION

The study area is located in the eastern part of Anadarko Basin, Oklahoma (Figure 1.1). Pennsylvanian rocks throughout most of the Anadarko Basin are dominated by shallow shelf marine clastics. The target is the Red Fork sand of Middle Pennsylvanian age which lies at an approximate depth of 2700 m (~9000 ft) and is composed of clastic facies deposited in deep-marine (shale/silt) to shallow water fluvial-dominated environment. The Red Fork sand is sandwiched between limestone layers, with the Pink Lime on the top and the Inola Lime on the bottom. The Oswego Lime that lies above the Pink Lime and the Novi Lime that lies below the Inola Lime, are very prominent reflectors that can be readily mapped on the seismic amplitude data, providing an approximation to a fixed geologic time. The Upper Red Fork incised valley system consists of multiple

stages of incision and fill, resulting in a stratigraphically complex internal architecture (del Moro et al., 2013).

The survey of interest was recorded at various times, beginning in the mid-1990s. CGGVeritas acquired licenses for these surveys, shot infill data in 2009 where necessary, and carefully reprocessed them, resulting in a mega−merge survey. In addition to more modern statics and deconvolution algorithms, the most significant advantage of the mega-merge survey is the inclusion of a wider migration aperture, providing the diffraction energy needed to image faults and stratigraphic edges (Del Moro et al., 2013; Li et al., 2015). The incised valleys are characterized by discontinuous reflections of varying amplitude which are difficult to interpret laterally (Peyton et al., 1998). It is difficult to interpret the Red Fork incised valley using traditional interpretation techniques (auto picking horizons, amplitude mapping, etc.). Individual stages of fill are almost impossible to identify.

ATTRIBUTE EXPRESSION ON VALLEY FILL

Figure 1.2 displays Red Fork stratal slices through the seismic amplitude and coherence volumes. Vertical slices through the seismic amplitude provide an indication of erosion, but do not allow one to identify the various stages of valley fill. The coherence attribute in Figure 1.2b was computed volumetrically from the broad-band seismic data after spectral balancing using 5-trace, 11-sample (±20 ms), and as expected, image the boundaries of the valley as well as some internal incisements; however, the overall internal detail is diffuse. The main reason of this lack of detail is that the coherence was computed from the broad-band seismic amplitude data volume, and thus measures a mix

of valley fill stages in the same image. In contrast, lateral changes in sedimentary layers and channel incisement of a given thickness are often better imaged near their tuning thickness.

The Red Fork incised valley can be mapped by using spectral components between about 20 Hz and 50 Hz. Peyton et al. (1998) chose 36-Hz amplitude slice as the best images of the valley throughout the survey area resulting in the image shown in Figure 1.3. Their coherence example, represents channel features illuminated by the dominant frequency components.

The cartoon by Laughlin et al. (2002) in Figure 1.4 shows how thicker and thinner stratigraphic features will be tuned in at correspondingly lower or higher frequency components. In practice, the interpreter animates through a suite of spectral components and stops the animation when a particular feature of interest is well delineated. The same strategy should be also adopted in valley fill analysis. Figure 1.5 shows the dominant frequency map of Red Fork formation. Different types of geological structures and different stages of valley fill each with its own tuning thicknesses give rise to anomalies at different dominant frequencies.

MULTISPECTRAL ANALYSIS

Spectral magnitudes and coherences corresponding to these tuned frequencies provide clearer images. Though the spectral decomposition reveals more details, it generates a series of maps or volumes at different frequencies, which are analyzed one by one or through animation. Blending RGB (red-green-blue) images have long been used to express multiple spectral components in a single image (Balch, 1971). A more recent

exposition on the value of RGB in rendering multiple spectral images of channels can be found in Leppard et al. (2010). I use RGB color blending technique in Figure 1.6 to display the 20, 35 and 50 Hz spectral components. As shown in the RGB color map, if the energies in all three colored channels are at or above the threshold amplitude, the blended color is white, while if the energy of one channel is stronger than the other two, its color would dominate. The new information is revealed by the color changes. The 20 Hz component is plotted against red and better delineates Stages II, III and V. The 35 Hz component is plotted against green and delineates medium thickness Stage V channels. The 50 Hz component is plotted against blue and delineates thinner Stage V channels and part of Stage III. Compared with the interpretation in Figure 1.3, which is a part of the survey, note that the stages interpreted by Peyton et al. (1998) also display in different colors. Stage I is not clearly separated from Stage II or III, which cannot be achieved neither on single frequency slice interpretation as Peyton et al. (1998) did. In other parts of the survey, other stages as well as some geological structures are displayed with different temporal tuning thickness in different colors. There are other good methods that can analyze tuning thickness variance, but none are as easy to create or as routinely used.

I selected 20, 35 and 50 Hz to compare to Peyton et al.'s (1998) 36 Hz component image in Figure 1.6. Next, in Figure 1.7 I compute coherence from each of these spectral components, providing a measure of the edges sensitive to the relative thicknesses of the different stages of valley fill. Color blending of coherence is slightly different with the color blending of spectral magnitudes, where the result is subtractive rather than additive. If all spectral magnitudes are zero, one obtains a black image. If all spectral coherences are unity, one obtains a white image. A high spectral magnitude at the 20 Hz component

results in a red anomaly. In contrast, a low spectral coherence at 20 Hz results in less red, or a cyan anomaly. The black (dark gray) lines are the channel boundaries which appear on all the selected frequency components. The boundaries of relative thick channels showing on lower frequency component painted red would appear as cyan after blending (the opposite color of red on the color wheel), while edges of thinner channels in part of Stage III and V appear magenta or yellow. Since the channel edges can be characterized by other frequency bands, the channel edges shown in Figure 1.7 are not as many as those in Figure 1.2b. In addition, for the most area of the image without channel boundaries, the color delegates the change of coherent energy, for example, the large magenta (which is the opposite of green) area implies that lower coherent energy in middle frequency component. Figure 1.8 adds a fourth broadband coherence image shown in Figure 1.2b using opacity to the RGB blended map shown in Figure 1.7. Comparison between Figures 1.7 and 1.8 shows the advantage brought by spectral component coherences. Through the colorful attribute integration image, one is no-longer thickness unaware.

Until now, the coherence images have been directly computed from different spectral voice components. However, thin beds that are tuned might be expected to better exhibit discontinuities at their higher amplitude tuning frequency than at other frequencies. For this reason, one may wish to not only examine coherence computed from different voices, but also somehow combine them into a single composite image.

Figure 1.9 shows coherence computed from six spectral voices (equivalent to six band-pass filtered data volumes) beginning with corner frequencies of 10-15-25-30 Hz and ending with 110-115-125-130 Hz. As discussed above, different spectral bands

highlight different geological features. Note that in Figures 1.9e and 1.9f that the noise becomes equal to, and then even stronger than signal.

Figure 1.10b shows the multi-spectral coherence computed from all seven filter bank voices defined by the covariance matrix in Equation 1.5. Compared with the broadband coherence shown in Figure 1.10a, random noise (indicated by red dashed ellipses) has been suppressed and the channel boundaries sharper at some locations.

While the computational effort of multispectral coherence increases linearly with the number of spectral components analyzed, the actual increase is somewhat less because of fixed i/o and data transfer overhead. Most of this cost is in computing the individual covariance matrices defined by Equation 1.5. In my implementation, I allow the computation of the individual components as well, providing the images shown in Figure 1.7. While I find the multispectral coherence image to be "better" than the bandlimited and broad-band coherence images, co-rendering the individual images (Figure 1.11) still provides additional insight. Analysis of such images provide insight into which spectral component is a meaningful indicator of a given structural or stratigraphic feature.

Thus, by more fully using the spectral components, the corresponding coherence map and multi-spectral coherence attribute, the stage identification and valley fill boundary delineation can be more completely interpreted.

CONCLUSIONS

The interpretation of incised valley fill can be difficult on conventional amplitude volumes. Multispectral coherence provides improved images over traditional coherence images, even if the seismic amplitude data have been previously spectrally balanced.

While much of this improvement can also be found in RGB blended volumes, multispectral coherence provides several advantages: (1) one can combine the information content of more than three coherence volumes, (2) there is only one rather than three volumes to be loaded into the workstation, which may be a limitation for very large data sets, and (3) the grey-scale image can be co-rendered with other attributes of interest plotted against a polychromatic color bar, such as P-impedance vs. Poisson's ratio or SOM (self organizing map) cluster results. Although the computation cost increases with the number of spectral voices, the additional time savings in interpreting ambiguous channels and the revelation of previously hidden features is of significant value for the human interpreter.

CHAPTER 1 FIGURES

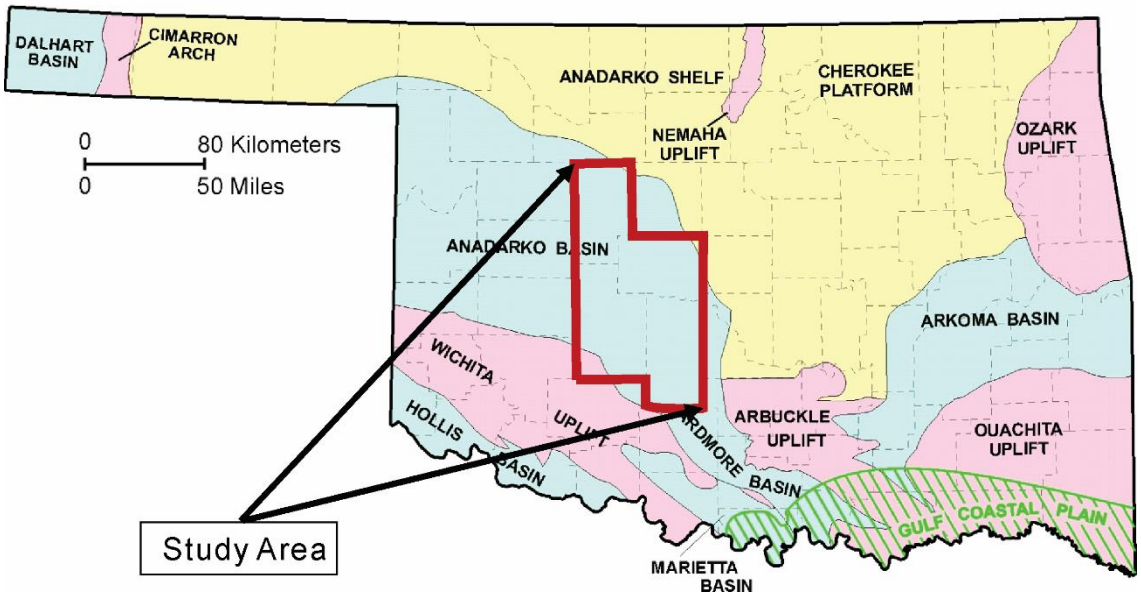

Figure 1.1. Location map of Anadarko basin area on map of Oklahoma, and the study survey is located inside the study area marked by red boundary (after del Moro et al., 2013).

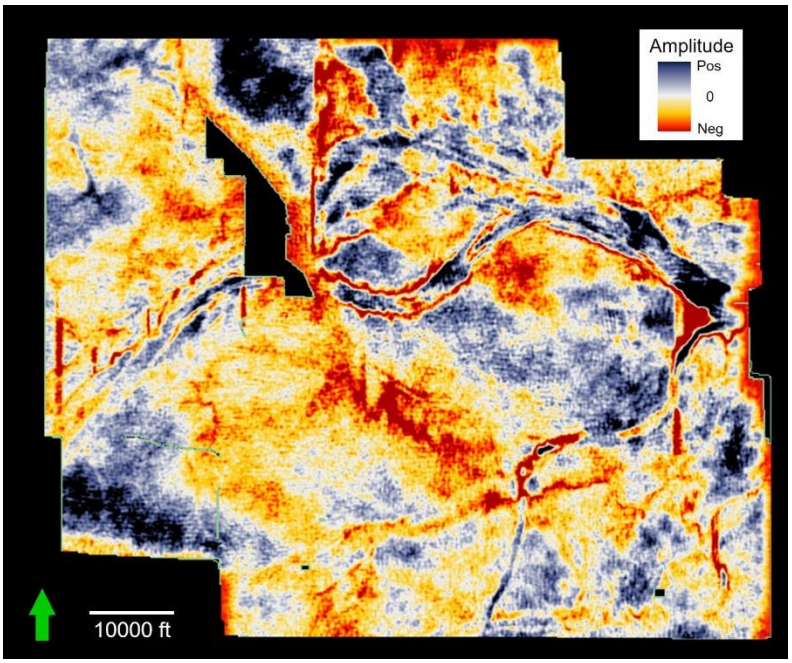

Figure 2a

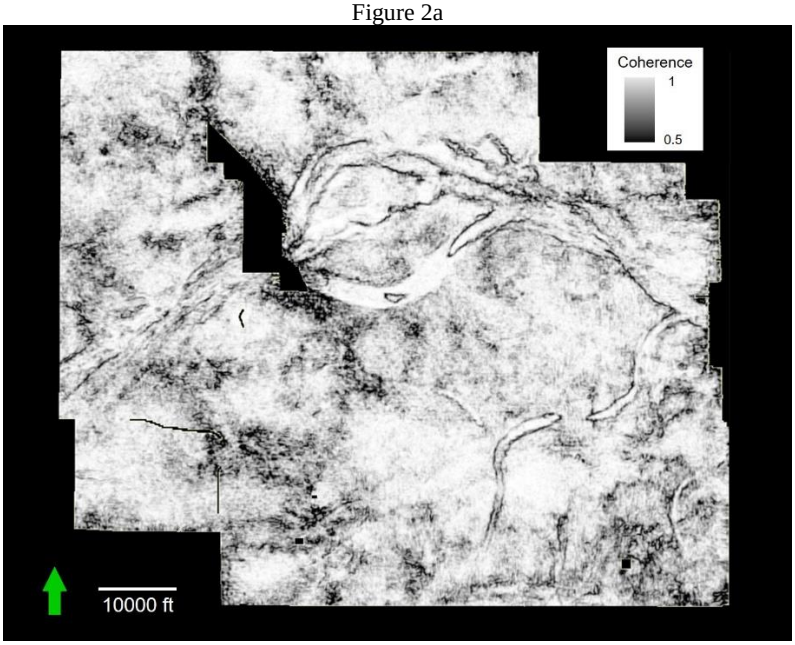

Figure 2b

Figure 1.2. Stratal slices through (a) seismic amplitude and (b) coherence volumes along the top Red Fork Formation from a mega-merge survey. Note the edges of the incised valley are shown on the coherence slice. Data courtesy of CGG-Veritas.

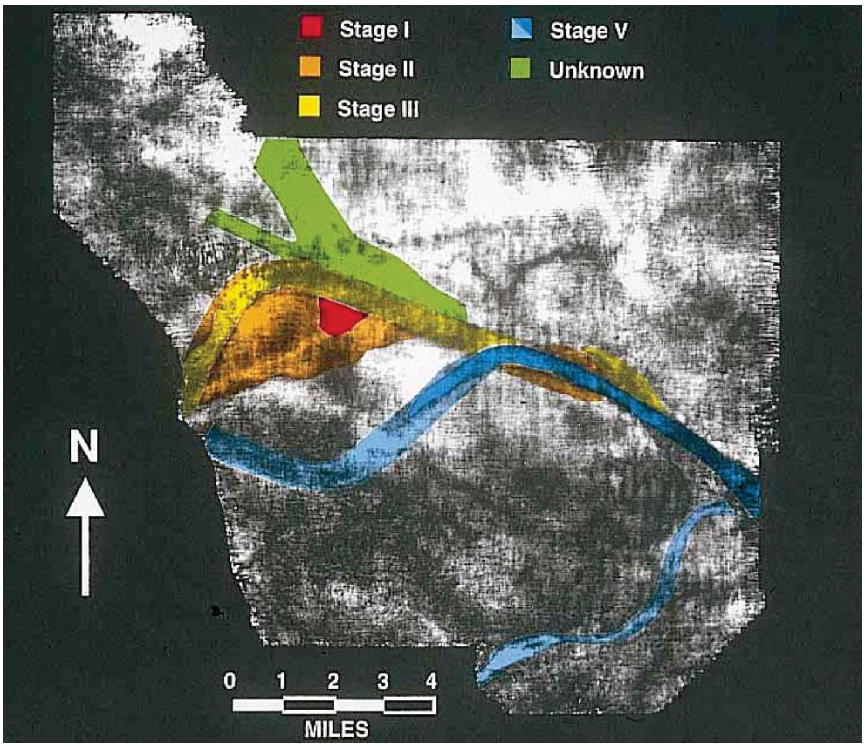

Figure 1.3. Peyton et al.'s (1998) original slice with interpretation through the 36-Hz spectral magnitude computed from the original 1995 seismic data volume. This same data volume formed part of the mega-merge survey shown in Figure 1.2.

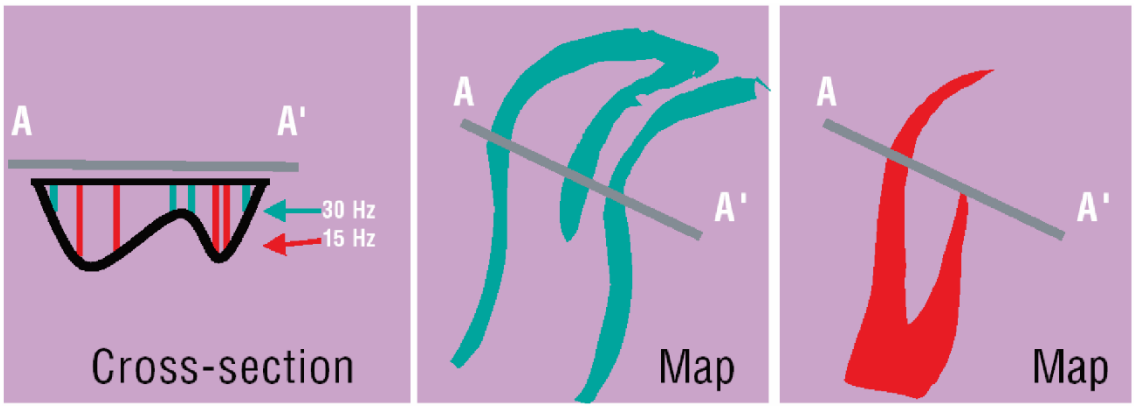

Figure 1.4. A cartoon of thin bed tuning. In thin reservoirs with varying thickness (left) seismic data with higher dominant frequency would highlight the thinner parts of the reservoir on amplitude maps (middle), while seismic with a lower dominant frequency would highlight the thicker parts on an amplitude map (right). (after Laughlin et al., 2002)

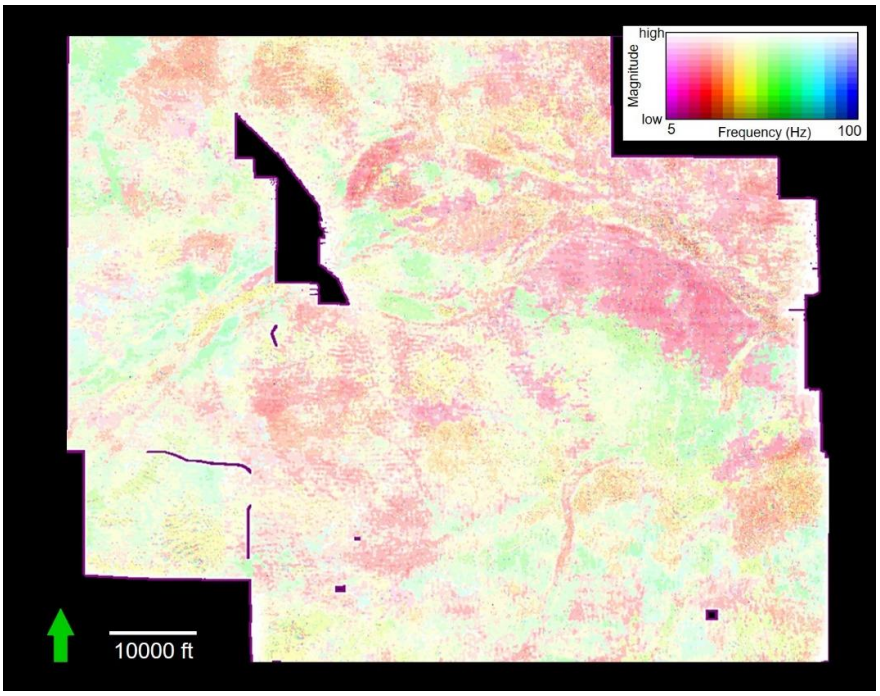

Figure 1.5. Dominant (or peak) spectral frequency image of the Red Fork horizon, which shows that the target horizon has different tuning thickness. The magnitude of the spectral component is plotted against a gray scale, thereby modulating the image.

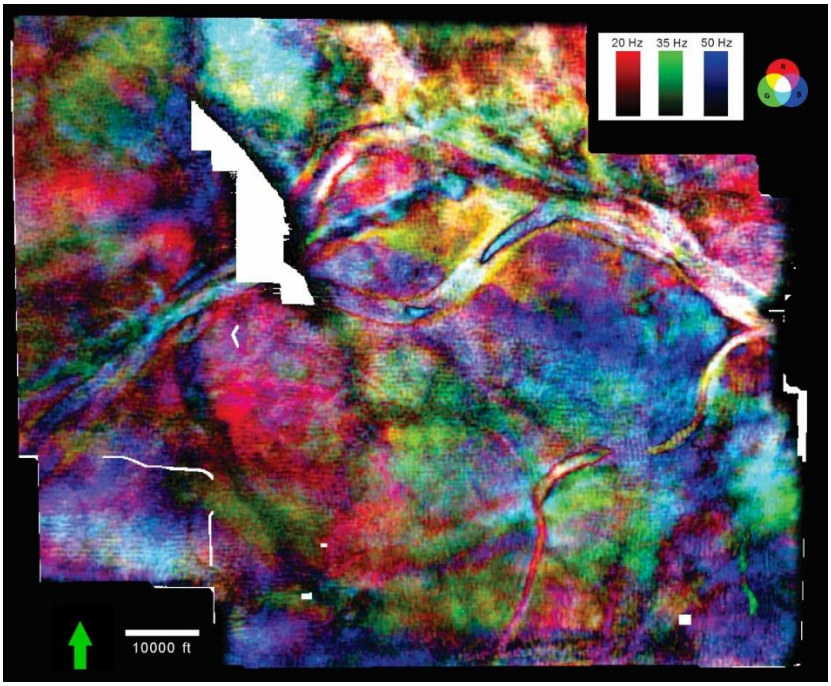

Figure 1.6. RGB blended spectral magnitude components at 20 Hz (in red), 35 Hz (in green) and 50 Hz (in blue).

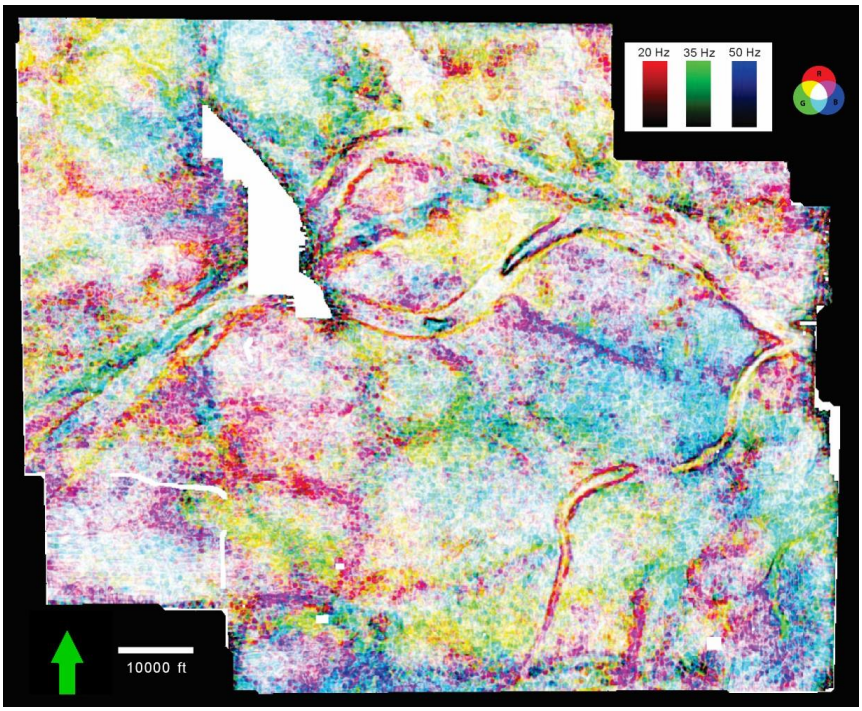

Figure 1.7. RGB blended image of coherence corresponding to Figure 1.6 computed from the 20 Hz (in red), 35 Hz (in green) and 50 Hz (in blue) spectral components.

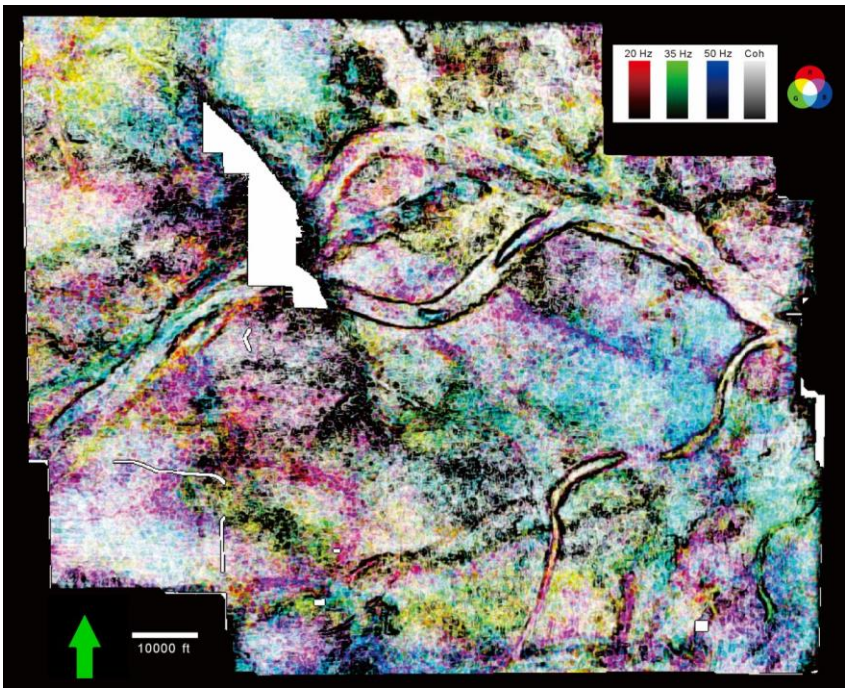

Figure 1.8. The same image shown in Figure 1.7 but now co-rendered with that of Figure 2b. Edges that are not overprinted in black were delineated by coherence computed from the corresponding spectral components, but not by the broad band coherence computation.

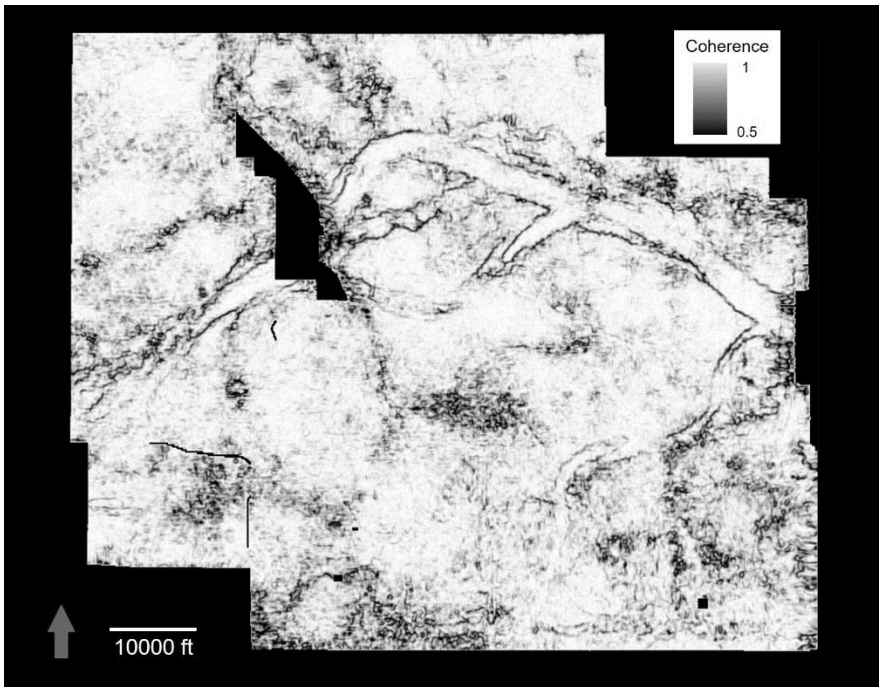

Figure 1.9a

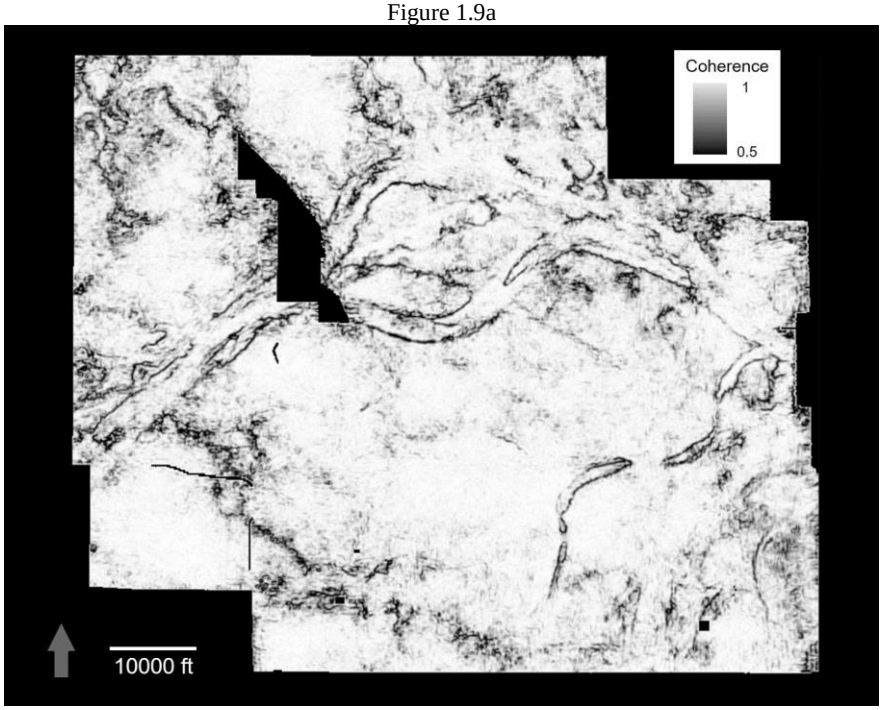

Figure 1.9b

Figure 1.9. Coherence attributes calculated from different spectral bands (a) 10-15-25-30 Hz, (b) 30-35-45-50 Hz, (c) 50-55-65-70 Hz, (d) 70-75-85-90 Hz, (e) 90-95-105-110 Hz, (f) 110-115-125-130 Hz. Note that different spectral bands highlight different features, and the high frequencies include noises.

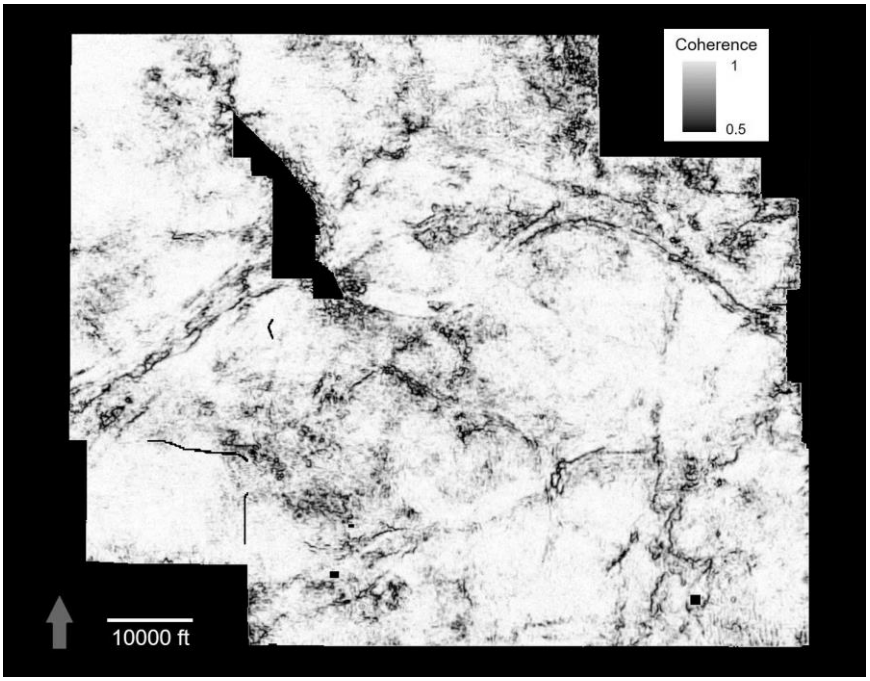

Figure 1.9c

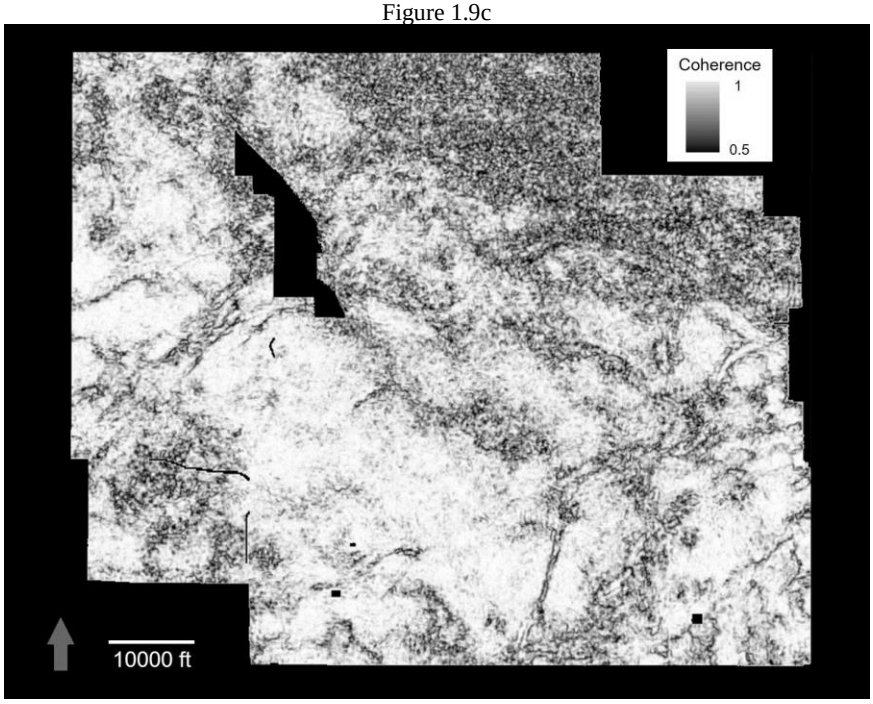

Figure 1.9d

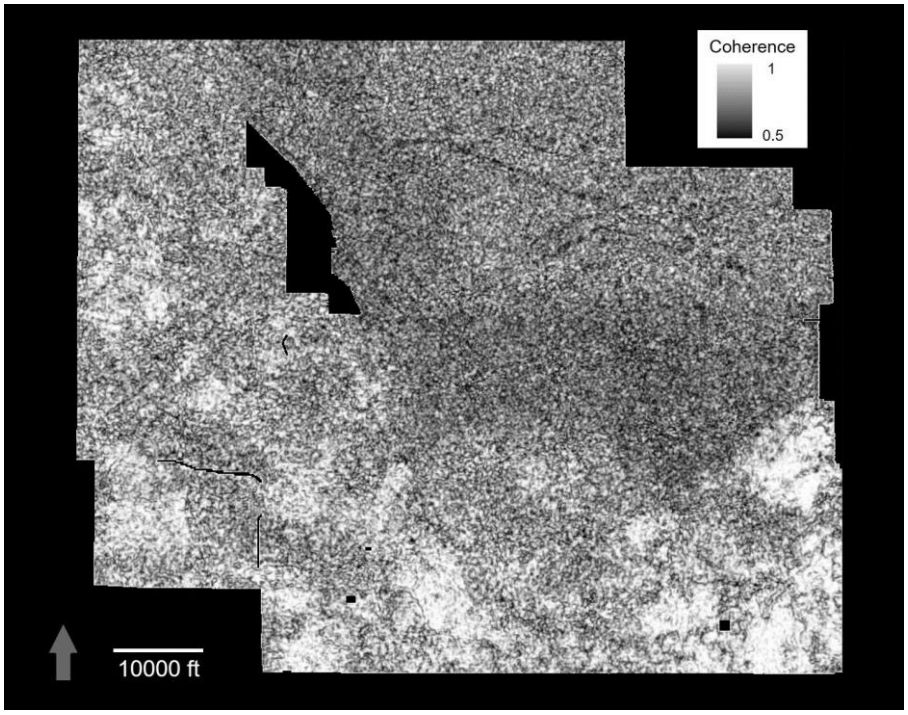

Figure 1.9e

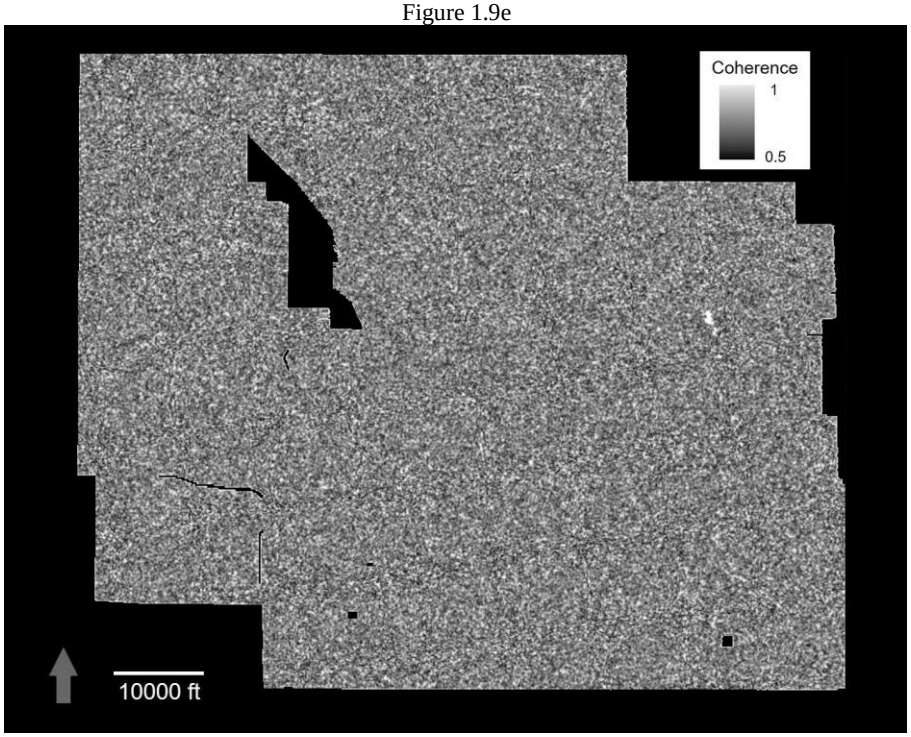

Figure 1.9f

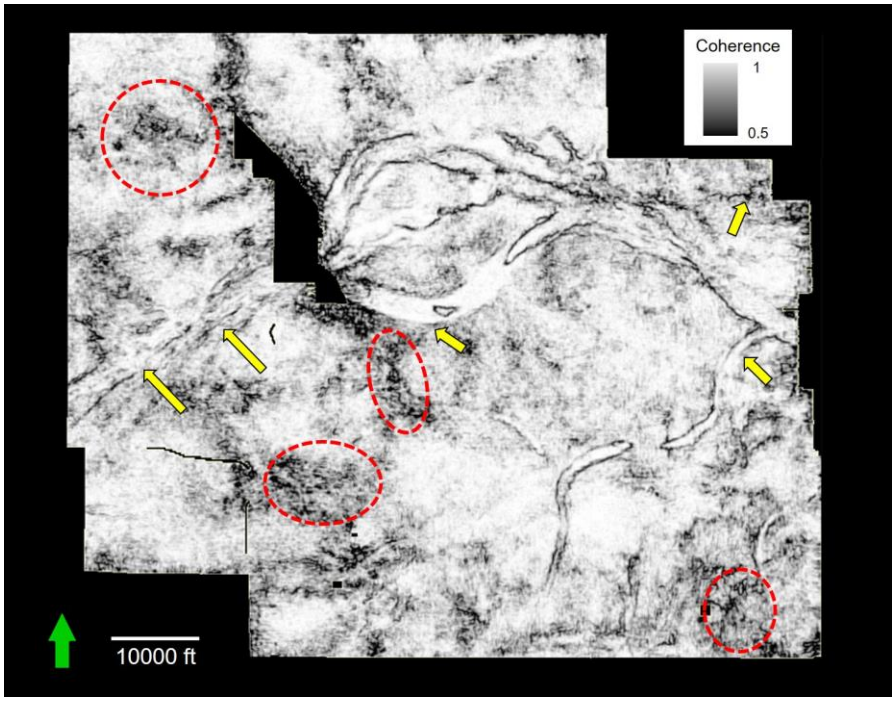

Figure 1.10a

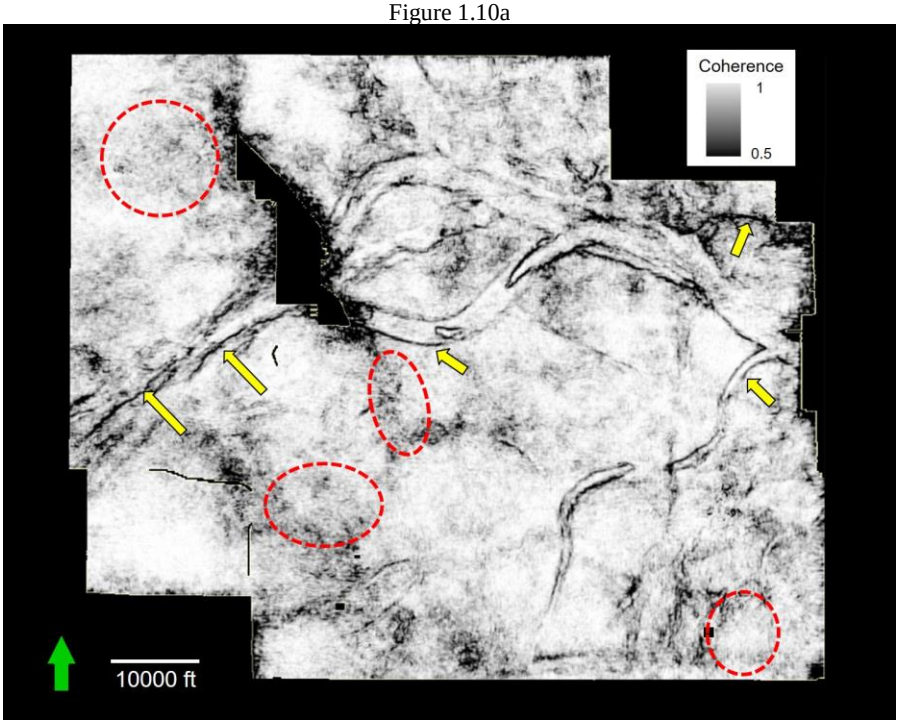

Figure 1.10b

Figure 1.10. (a) The same horizon slice along the top Red Fork Formation shown in Figure 1.2 through broad-band coherence, and (b) through multi-spectral coherence computed using all six spectral bands. Yellow arrows indicate channel boundaries are poorly delineated on the broadband coherence image. Red dashed ellipses indicate noisy areas that have been suppressed.

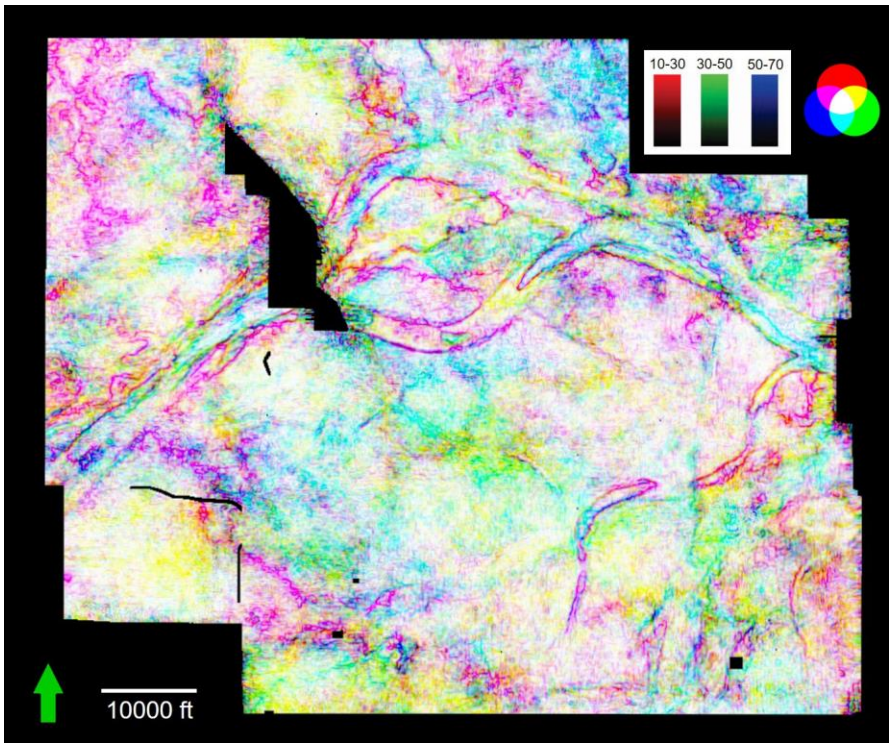

Figure 1.11. Co-rendered coherence for three of the six spectral bands. Red: 10-15-25-30 Hz, Green: 30-35-45-50 Hz, Blue: 50-55-65-70 Hz.

REFERENCES

Abele, S., and R. Roden, 2012, Fracture detection interpretation beyond conventional seismic approaches: AAPG-ICE, Milan.

Bahorich, M. S., and S. L. Farmer, 1995, 3-D seismic coherence for faults and stratigraphic features: The Leading Edge, **14**, 1053–1058.

Balch, A. H., 1971, Color sonograms: A new dimension in seismic data interpretation, Geophysics, **36**, 1074-1098.

Chopra, S. and K. J. Marfurt, 2007, Seismic attributes for prospect identification and reservoir characterization: SEG.

Del Moro, Y., A. Fernandez-Abad, and K. J. Marfurt, 2013, Why should we pay for a merged survey that contains data we already have? An OK Red Fork example: The Shale Shaker, **63**, 340-361.

Dewett, D. T, and A. A. Henza, 2015, Spectral similarity fault enhancement: Interpretation, **4**, SB149-SB159.

Fahmy, W. A., G. Matteucci, D. J. Butters, J. Zhang, and J. P. Castagna, 2005, Successful application of spectral decomposition technology toward drilling of a key offshore development well: 75th Annual International Meeting of the SEG, Expanded Abstracts, 262-264.

Gao, D., 2013, Wavelet spectral probe for seismic structure interpretation and fracture characterization: A workflow with case studies: Geophysics, **78**, O57–O67.

Gersztenkorn, A., and K. J. Marfurt, 1999, Eigenstructure based coherence computations: Geophysics, **64**, P1468–P1479.

Hardage, B., 2009, Frequencies are fault finding factors; looking low aids data interpretation: AAPG Explorer, **30**, no. 9, 34.

Honorio, B. C., Z. Correia, U. M. da C., M. C. de Matos, and A. C. Vidal, 2016, Similarity attributes from differential resolution components: Interpretation, **4**, T65-T73.

Laughlin, K., P. Garossino, and G. Partyka, 2002, Spectral decomposition applied to 3D: AAPG Explorer, **23**, no. 5, 28–31.

Leppard, C., A. Eckersly, and S. Purves, 2010, Quantifying the temporal and spatial extent of depositional and structural elements in 3D seismic data using spectral decomposition and multi attribute RGB blending, *in* L. J. Wood, T. T. Simo, and N. C. Rosen, eds., Seismic imaging of depositional and geomorphic systems: 30th Annual GCSSEPM Foundation Bob F. Perkins Research Conference, 1-10.

Li, F. Y., W.K. Lu, 2014, Coherence attribute at different spectral scales: Interpretation, **2**(1), SA99-SA106.

Li, F., J. Qi, and K. J. Marfurt, 2015, Attribute mapping of variable-thickness incised valley-fill systems: The Leading Edge, **34**, 48-52.

Lu, W., Y. Li, S. Zhang, H. Xiao, and Y. Li, 2005, Higher-order-statistics and supertrace-based coherence-estimation algorithm: Geophysics, **70**, P13-P18.

Marfurt, K.J., R.L. Kirlin, S. L. Farmer, and M.S. Bahorich, 1998, 3-D seismic attributes using a semblance-based coherency algorithm: Geophysics, **63**, 1150-1165.

Marfurt, K. J., 2017, Interpretational aspects of multispectral coherence: 79th EAGE conference and exhibition, DOI: 10.3997/2214-4609.201700528.

Ogiesoba, O. C. and B. S. Hart, 2009, Fault imaging in hydrothermal dolomite reservoirs: A case study: Geophysics, **74**, B71-B82.

Partyka, G. A., J. Gridley, and J. Lopez, 1999, Interpretational applications of spectral decomposition in reservoir characterization: The Leading Edge, **18**, 353–360.

Peyton, L., R. Bottjer, and G. Partyka, 1998, Interpretation of incised valleys using new-3D seismic techniques: A case history using Spectral Decomposition and coherency: The Leading Edge, **17**, 1294-1298.

Qi, J., G. Machado, and K. J. Marfurt, 2017, A workflow to skeletonize faults and stratigraphic features: Geophysics, **82**, O57-O70.

Sui, J.-K., X.-D. Zheng, and Y.-D. Li, 2015, A seismic coherency method using spectral attributes: Applied Geophysics, **12**, no. 3, 353-361.

Sun, D. S, Y. Ling, X.Y. Guo, J. Gao and J. X. Lin, 2010, Application of discrete frequency coherence cubes in the fracture detection of volcanic rocks in full-azimuth seismic data: 80th Annual International Meeting of the SEG, Expanded Abstracts, 1342-1346.

Wu, X., 2017, Directional structure-tensor-based coherence to detect seismic faults and channels: Geophysics, **82**, A13-A17.

Yan, B., S. Yuan, S. Wang, Y. Yang, T. Wang, and P. Shi, 2017, Improved eigenvalue-based coherence algorithm with dip scanning: Geophysics, **82**, V95-V103.

CHAPTER 2

SEISMIC ATTENUATION ESTIMATION USING A MODIFIED FREQUENCY SHIFT METHOD[2]

ABSTRACT

As a powerful tool for structural interpretation, reservoir characterization, hydrocarbon detection, quality factor *Q* provides useful information in seismic processing and interpretation. The popular methods, like spectral ratio (SR) method, central frequency shift (CFS) method, peak frequency shift (PFS) method, are based on the spectral variations between different spectral components supposedly brought from attenuation. However, there are respective limitations in field seismic data applications. The lack of a reliable method for estimating *Q* from reflection seismic data is an issue when utilizing *Q* value for hydrocarbon detection. In this chapter, I derive an approximate equation and propose a dominant and central frequency shift (DCFS) method by combining the quality factor *Q*, the travel time, dominant and central frequencies of two successive seismic signals, along the wave propagating direction. Based on multi-layered analysis, I then propose a method to obtain continuous volumetric *Q* estimation results. A test on synthetic data and statistical experiments show the proposed method can achieve higher accuracy and robustness compared with existing methods, and field applications also show its potential and effectiveness in estimating seismic attenuation.

---

[2] *This chapter contains content from a published article - **Li, F.**, H. Zhou, N. Jiang, J.X. Bi, K.J. Marfurt, 2015, Q Estimation from Reflection Seismic Data using a Modified Frequency Shift Method: Journal of Geophysics and Engineering, **12**, 577-586.*

INTRODUCTION

Seismic attenuation is a fundamental mechanism of elastic waves propagating through the earth. Attenuation acts as a time-variant low-pass filter with a monotonically increasing phase spectrum, which leads to that the seismic wavelet becomes more stretched and its amplitude becomes exponentially smaller with time or depth.

Attenuation, if quantified, can be used as a seismic attribute to characterize rock properties, reservoir heterogeneity, subtle geological structures, and the success of completion processes (Parra and Hackert, 2002; Korneev et al., 2004). For example, in fractured media, the magnitude of attenuation change with azimuth has been shown to be a useful indicator of fracture direction (Clark et al., 2001; Maultzsch et al., 2007). Attenuation is also sensitive to changes in gas saturation in partially saturated media (Winkler and Nur, 1982). For this reason, anomalously high attenuation can be viewed as a hydrocarbon indicator (Toksöz et al., 1979; Hedlin et al., 2001) especially if quantitative attenuation measurements can be made. Once attenuation is measured, it is possible to mitigate the resolution loss by applying processes such as inverse-Q filtering to raise the high-frequency content of later times in seismic sections to compensate for attenuation of the seismic wave (Wang, 2002; Zhang and Ulrych, 2002; Wang, 2006; Wang, 2008) to aid with structural interpretations (Kaderali et al., 2007), amplitude versus offset (AVO) analysis (Luh 1993), and anisotropic attenuation characterization (Maultzsch et al., 2007; Zhu and Tsvankin, 2007). Attenuation, therefore, can provide important information about the subsurface to facilitate seismic interpretation.

Seismic attenuation is usually quantified using quality factor, Q. The anelasticity and inhomogeneity in the subsurface dissipate high frequency seismic energy, which

decreases seismic amplitude. Ricker (1953) developed a wavelet broadening technique to determine attenuation. After that, much research work has been made for *Q* estimation. In the time domain, *Q* can be estimated by pulse amplitude decay (Brzostowski and McMechan, 1992), pulse rise time (Kjartansson, 1979), and pulse broadening (Wright and Hoy, 1981). However, amplitude information of seismic pulses is often influenced by scattering, geometric spreading and other factors. In the frequency domain, *Q* estimates include the spectral ratio (SR) (Hauge, 1981; Raikes and White, 1984; Sams and Goldberg, 1990; White, 1992), central frequency shift (CFS) (Quan and Harris, 1997), peak frequency shift (PFS) (Zhang and Ulrych, 2002), improved peak frequency shift (IPFS) (Hu et al., 2013), and Gabor-Morlet joint time frequency analysis (JTFA) (Singleton et al., 2006) methods, all of which require time-frequency transforms to calculate the spectra of seismic records.

Additionally, *Q* can also be estimated by variation of instantaneous frequency (IF) of a seismic signal. Barnes (1991), Tonn (1991), and Engelhard (1996) developed the relations between the measured instantaneous spectra and seismic attenuation. Assuming that the source wavelet is a band-pass wavelet, Barnes (1991) obtained the relation between *Q* and IF variations to establish a *Q* estimation approach. Matheney and Nowack (1995) proposed the IF matching (IFM) method. Li et al. (2006) suggested using peak scale variations in the wavelet domain to estimate *Q* by assuming an idealized pulse as the seismic source wavelet. Gao et al. (2009) estimated *Q* using the variation of the IFs at the envelope peaks of two successive seismic wavelets. As it is based on the instantaneous attributes, this kind attuation estimation method is called an instantaneous

Q method. However, Yang and Gao (2010) finds these relationships between attenuation and IF are qualitative or implicit, resulting in unstable or unreliable estimation results.

Among the many methods available for measuring seismic attenuation, frequency-based methods are common in exploration geophysics because of their reliability and ease of use. The most classic approach is the spectral-ratio (SR) method, which measures the log of the ratio between two amplitude spectra computed as a function of frequency. Unforturnately, the SR method is sensitive to noise. As opposed to the SR method, the frequency-shift methods, such as CFS and PFS, use the statistics of the spectra rather than the entire spectrum, which improves the accuracy of the estimation.

In subsequent sections, I first analyze the presuppositions of CFS and PFS method. Then, I derive an approximate equation combining *Q*, and variance of dominant and central frequencies, and propose a method called the dominant and central frequency shift (DCFS) method.

EXISTING METHODS AND THEIR ASSUMPTIONS

The underlying theory of *Q* and associated measurement methods are well established (White, 1992; Reine et al., 2009). For frequency independent intrinsic *Q* in the bandwidth of interest, a seismic signal will have its spectral amplitude $A_0(f)$ modified to $A_1(f)$ after traveling time t at frequency f :

$$A_1(f) = A_0(f)\exp\left(\frac{-\pi ft}{Q}\right), \tag{2.1}$$

where the amplitude decay or increase caused by frequency-independent effects is ignored. The observed difference in the frequency spectrum of a Ricker seismic pulse at

t=0 s and time *t*=0.1 s are shown in Figure 2.1 where the source wavelet propagates through attenuating media with different *Q* values.

Based on Equation 2.1, the SR method can be represented as,

$$\ln\left(\frac{|A_1(f)|}{|A_0(f)|}\right) = \frac{-\pi f t}{Q}. \tag{2.2}$$

An estimate of *Q* can be derived by curve fitting within the common effective bandwidth of the two spectra using the least-squares method. An effective bandwidth should be chosen to avoid high frequency fluctuation caused by additive noise or numerical errors due to finite precision.

Quan and Harris (1997) proposed the CFS method by correlating *Q* with the changes in the central frequency of the seismic signal. For the reference seismic signal A_0 and the target seismic signal A_1, the central frequencies denoted by f_{c_0} and f_{c_1}. Assuming that $|A(f)|$ is of Gaussian shape, *Q* can be quantified by,

$$Q = \frac{\pi t \sigma_{A_0}^2}{f_{c_0} - f_{c_1}}, \tag{2.3}$$

where $\sigma_{A_0}^2$ is the spectrum variance of A_0, defined by,

$$\sigma_{A_0}^2 = \frac{\int_0^\infty (f - f_{c_0})^2 |A_0(f)| df}{\int_0^\infty |A_0(f)| df}. \tag{2.4}$$

Compared to the SR methods, the CFS method is quite robust, because the estimation of the central frequency is relatively insensitive to noise. However, the CFS method assumes a Gaussian shape of the seismic spectrum and the stationary spectral variance. In practice, the seismic spectrum is rarely a Gaussian and attenuation changes the spectral variance, introducing inaccuracies to this method.

Zhang and Ulrych (2002) proposed a peak frequency shift (PFS) method to estimate *Q*. For a shallower reference wavelet b_0 and a deeper target wavelet b_1, denote the peak frequencies by f_{p_0} and f_{p_1}. Assuming that the seismic source can be represented by a Ricker wavelet, the PFS estimate of *Q* is

$$Q = \frac{\pi t f_{p_1} f_{p_0}^2}{2(f_{p_0}^2 - f_{p_1}^2)}. \tag{2.5}$$

Recall that spectrum of a Ricker wavelet (Ricker, 1953) is

$$A(f) = \frac{2}{\sqrt{\pi}} \frac{f^2}{f_m^3} \exp(-\frac{f^2}{f_m^2}), \tag{2.6}$$

where f_m is the dominant frequency of the wavelet, the peak frequency is the dominant frequency for a Ricker wavelet. The Ricker-wavelet assumption is more representative of seismic data than a morlet wavelet with a Gaussian spectra assumed by the CFS method. However, the maximum value of the spectra amplitude is easily affected by the background noise, which cannot be ignored. Thus, in practice, the PFS method is less stable in field application than the CFS method.

DOMINANT AND CENTRAL FREQUENCY SHIFT METHOD

Combining Equations 2.1 and 2.6, and assuming the seismic wave propagating in the earth media with a *Q* factor for *t* seconds, the amplitude spectrum of the received signal is

$$A(f,t) = \frac{2}{\sqrt{\pi}} \frac{f^2}{f_m^3} \exp\left(-\frac{f^2}{f_m^2}\right) \exp\left(-\frac{\pi f t}{Q}\right), \tag{2.7}$$

where f_m denotes the dominant frequency of the source wavelet.

The central or mean frequency of a signal $s(t)$ is usually defined as

$$f_c = \frac{\int_0^\infty f \cdot \mathrm{S}(f)df}{\int_0^\infty \mathrm{S}(f)df}, \tag{2.8}$$

where $\mathrm{S}(f)$ is the amplitude spectrum of signal $s(t)$.

Wang (2015) suggested that central frequency should be estimated using the power spectrum rather than the amplitude spectrum, and showed that such an estimate has a higher correlation to estimates made using discrete Fourier spectra of seismic data.

Wang's (2015) central frequency is this:

$$f_c = \frac{\int_0^\infty f \cdot \mathrm{S}^2(f)df}{\int_0^\infty \mathrm{S}^2(f)df}. \tag{2.9}$$

Such that, the central frequency of the received seismic signal amplitude spectrum $A(f,t)$ is

$$f_c = \frac{\int_0^\infty f\left|A(f,t)\right|^2 df}{\int_0^\infty \left|A(f,t)\right|^2 df} = \frac{\int_0^\infty f\left[\frac{2}{\sqrt{\pi}}\frac{f^2}{f_m^3}\exp\left(-\frac{f^2}{f_m^2}\right)\exp\left(-\frac{\pi ft}{Q}\right)\right]^2 df}{\int_0^\infty \left[\frac{2}{\sqrt{\pi}}\frac{f^2}{f_m^3}\exp\left(-\frac{f^2}{f_m^2}\right)\exp\left(-\frac{\pi ft}{Q}\right)\right]^2 df}. \tag{2.10}$$

Simplifying Equation 2.10, one can obtain

$$f_c = f_m \frac{\int_{\frac{\pi f_m t}{2Q}}^\infty \left(x - \frac{\pi f_m t}{2Q}\right)^5 \exp\left(-2x^2\right)dx}{\int_{\frac{\pi f_m t}{2Q}}^\infty \left(x - \frac{\pi f_m t}{2Q}\right)^4 \exp\left(-2x^2\right)dx}, \tag{2.11}$$

where $x = \frac{f}{f_m} + \frac{\pi f_m t}{2Q}$.

Separating the factors, computing the integrals, and using the first-order Taylor series approximation, I obtain

$$f_c = \frac{f_m}{2\sqrt{\pi}} \frac{\begin{array}{c}\left(\sqrt{\pi}-1\right)\alpha^6 - \sqrt{2\pi}\alpha^5 + \left(10\sqrt{\pi}-7\right)\alpha^4 \\ -10\sqrt{2\pi}\alpha^3 + 5\left(3\sqrt{\pi}+2\right)\alpha^2 - 15\sqrt{2\pi}\alpha + 16\end{array}}{\begin{array}{c}\frac{\sqrt{\pi}-1}{\sqrt{\pi}}\alpha^5 - \sqrt{2}\alpha^4 + 3\frac{1-2\sqrt{\pi}}{\sqrt{\pi}}\alpha^3 \\ +6\sqrt{2}\alpha^2 - \frac{10\sqrt{\pi}+3\pi}{\pi}\alpha + 3\sqrt{2}\end{array}}, \quad \alpha = \frac{\pi f_m t}{Q} \qquad (2.12)$$

To validate the correctness of Equation 2.12, I compute f_c of the source signal,

$$f_c = \frac{\int_0^\infty f\left|A(f)\right|^2 df}{\int_0^\infty \left|A(f)\right|^2 df} = \frac{\int_0^\infty f\left[\frac{2}{\sqrt{\pi}}\frac{f^2}{f_m^3}\exp\left(-\frac{f^2}{f_m^2}\right)\right]^2 df}{\int_0^\infty \left[\frac{2}{\sqrt{\pi}}\frac{f^2}{f_m^3}\exp\left(-\frac{f^2}{f_m^2}\right)\right]^2 df} = \frac{\frac{1}{2\pi}}{\frac{3}{8\sqrt{2\pi}\,f_m}} = \frac{4}{3}\sqrt{\frac{2}{\pi}}\,f_m. \qquad (2.13)$$

When there is no attenuation, Q equals infinity in Equation 2.12, the central frequency of the source signal becomes

$$f_c = \frac{f_m}{2\sqrt{\pi}}\frac{16}{3\sqrt{2}} = \frac{4}{3}\sqrt{\frac{2}{\pi}}\,f_m, \qquad (2.14)$$

which has the same form as Equation 2.13, thereby conforming the approximations about central frequency, dominant frequency and Q made in Equation 2.12 are correct.

As my goal is to estimate Q factor, I rearrange Equation 2.12 to obtain a six order polynomal equation in one variable. An approximate solution is

$$Q \approx \frac{{f_m}^2 \pi t}{4 f_m \sqrt{\frac{2}{\pi}} - 3 f_c \sqrt{\pi}}. \qquad (2.15)$$

Equation 2.15 summarizes the relationship between the central frequency f_c, dominant frequency f_m and Q. I call this estimation the dominant and central frequency shift (DCFS) method. DCFS is a modified CFS method, substituting a Gaussian spectrum by that of a Ricker wavelet, which better approximates seismic data acquired with dynamite sources prior to spectral balancing.

Two aspects should be noticed: first, the constant Q model assumes that the attenuation effect is "constant" in the target horizon, so I can only get "average" attenuation estimation; second, whether using the CFS or the DCFS method, the first-order Taylor approximation has been employed during the simplification process. For this approximation to be accurate, the travel time t should be small. Thus, when a target horizon is relatively thick, for both physical and mathematical aspects, one needs to treat it as a multi-layered model, separate it into some thin layers, and do the Q estimation layer by layer (Zhang and Ulrych, 2002; Wang, 2008). As the time interval t becomes smaller and smaller, the Q estimation result changes from piecewise constant, discrete volumes to represent continuous values.

MULTI-LAYERED IMPLEMENTATION

First, consider a case of two layers with quality factors Q_1 and Q_2, and travel times t_1 and t_2, where the total travel time $t = t_1 + t_2$ and the total equivalent quality factor is Q. Applying Equation 2.1 gives

$$A(f,t) = A_0(f)\exp\left(\frac{-\pi ft}{Q}\right) = A_0(f)\exp\left(\frac{-\pi ft_1}{Q_1}\right)\exp\left(\frac{-\pi ft_2}{Q_2}\right). \qquad (2.16)$$

Knowing Q and Q_1, Q_2 can be expressed by

$$Q_2 = \frac{t_2 Q_1 Q}{(t_2 + t_2) Q_1 - t_1 Q}. \tag{2.17}$$

From Equation 2.16, the equivalent Q can be estimated using the dominant frequency of the source wavelet and central frequency at time t. Since the dominant frequency f_m of the initial wavelet and Q_1 have already been determined from upper-layer arrivals with the known travel time parameters t_1 and t_2, Q_2 can be computed using Equation 2.17.

Suppose that the subsurface medium is divided into N layers, separated at times $t_0, t_1, \cdots, t_i, \cdots, t_{N-1}, t_N$, where $t_N = t$, with a total equivalent quality factor Q, the amplitude spectrum is defined by

$$\mathrm{A}(f,t) = \mathrm{A}_0(f) \exp\left(\sum_{i=1}^{N} \frac{-\pi f \Delta t_i}{Q_i} \right), \tag{2.18}$$

where $\Delta t_i = t_i - t_{i-1} \geq 0$ and Q_i are the travel time and quality factor in the ith layer, respectively.

For the last layer with the thickness $\Delta t_N = t - t_{N-1}$, the amplitude spectrum is

$$\mathrm{A}(f,t) = \mathrm{A}_0(f) \exp\left(\sum_{i=1}^{N-1} \frac{-\pi f \Delta t_i}{Q_i} \right) \exp\left[\frac{-\pi f (t - t_{N-1})}{Q_N} \right]. \tag{2.19}$$

Similar to Equation 2.17, the equation for Q_N becomes

$$Q_N = \frac{\Delta t_N}{\frac{t}{Q} - \sum_{i=1}^{N-1} \frac{\Delta t_i}{Q_i}}. \tag{2.20}$$

Now, the Q factor values can be computed layer by layer. Then one can get a "continuous" attenuation estimation result.

Inspired by Wang (2008), in order to stabilize this procedure and make the result more robust, I normalize the amplitude spectrum $A(f,t)$ between t_{n-1} and t_n:

$$\hat{\mathrm{A}}(f,t)=\begin{cases}\hat{\mathrm{A}}(f,t_{n-1}), & for \quad \exp\left(\sum_{i=1}^{n-1}\frac{-\pi f\Delta t_i}{Q_i}\right)\geq 1\\ \dfrac{\mathrm{A}(f,t)}{\exp\left(\sum_{i=1}^{n-1}\frac{-\pi f\Delta t_i}{Q_i}\right)}, & for \quad \beta\leq\exp\left(\sum_{i=1}^{n-1}\frac{-\pi f\Delta t_i}{Q_i}\right)<1\\ 0, & for \quad \exp\left(\sum_{i=1}^{n-1}\frac{-\pi f\Delta t_i}{Q_i}\right)<\beta\end{cases}, \tag{2.21}$$

where the threshold β is related to signal to noise ratio.

In this way, the small amplitude samples are ignored in the *Q* analysis, so I can suppress noise interference, on the other hand, which is more important, the unphysical negative *Q* value can also be eliminated.

SYNTHETIC TEST

In order to confirm the effectiveness and stability of the DCFS method, I estimate *Q* values on both noise-free and noise-added synthetic data and analyze the results calculated by SR, CFS and DCFS methods.

I use a Ricker wavelet with a dominant frequency of 40 Hz to produce a noise-free synthetic with *Q* = 80, 50, 40 and 30 shown in Figure 2.2a. The results of *Q* estimation obtained by SR, CFS and DCFS methods show that three methods perform well in the noise-free case, as shown in Figure 2.2b.

It is known that to ensure the stability in evaluating *Q* factor is challenging when the data are contaminated by noise. Therefore, I evaluate the SR, CFS, and DCFS methods for SNR=30, 10, 5, 0, and -1 dB (Figure 2.3). There are noticeable differences between

the three methods even in the high SNR situation. For the SR method computed between 30 and 50 Hz, accuracy and stability of the estimation is highly dependent on the SNR of original data. When the SNR falls below 5 dB, the DCFS method performs more robustly, with the results calculated by DCFS closer to the true *Q* values than those of the other two methods (Figures 2.3h and 2.3j).

NUMERICAL TEST AND ERROR ANALYSIS

Systematic and random errors are the key factors that influence the accuracy and robustness of most *Q* estimation methods. Figure 2.4 shows the result of 100 independent realization for the fourth layer of the synthetics (shown in Figure 2.2) with different SNR=30, 10, 5, 0, and -1 dB to estimate the *Q* value. The actual noise pattern for each realization is different. These experiments show that the DCFS method (red curve) is more robust than the SR and CFS methods. Note the negative *Q* values for the low SNR case that occur when using the SR and CFS methods in Figures 2.4d and 2.4e.

Table 2.1 summarizes the results of these 100 realizations. The mean value of *Q* from DCFS is closer to the actual *Q* value 30, while the standard deviation is stable even when the noise level is greater than effective signal (SNR=-1dB). In contrast, the anomalously large values of mean and standard deviations using the SR and CFS method imply that these two methods are less robust.

APPLICATION TO FIELD DATA

In order to test the validity of the proposed method, I applied the DCFS to a 3D land survey acquired in western China, showing the value in delineating a known gas

reservoir. Figure 2.5 shows a geological cross section through three wells, displaying the gas reservoir distribution, lithology and well logs (e.g. gamma ray (GR), resistivity (RT), acoustic (AC) and density (DEN)). The sandstone reservoir is full of gas displayed by yellow under the layer L2 at Well A and B, while there is no oil or gas response at well C. The information from the well logs is used to provide guidance in discriminating the lithological boundaries and indicating gas reservoir. Figure 2.6 shows the location the three joint wells on the 3D seismic survey.

Figure 2.7a shows a vertical slice through the three wells through the seismic amplitude volume. Wells A and B are productive wells, while Well C is nonproductive. The sampling interval is 1ms. Figure 2.7b shows the same slice through the *Q* volume calculated using Equations 2.15 and 2.20. Note the low *Q* values of the target layer L2 are highlighted by red curve at the location of productive wells A and B, which implies strong absorption or attenuation in the gas-bearing sandstone. In contrast, there is no attenuation anomaly at the nonproductive Well C. The gas distribution denoted by the red ovals from the well logs (Figure 2.5) is consistent with *Q* value estimation results (Figure 2.7b). In order to further show the advantage of DCFS method, I extract *Q* along phantom horizon slices 10 and 20 ms below the L2 horizon using the three methods, while the SR, CFS and DCFS show similar trends. The DCFS *Q* estimation more accurately correlates to the well control, distinguishing productive Well B and dry-hole Well C. Figure 2.7d shows phantom horizon slices 10 ms below L1 through the three *Q* estimates. All three methods show mudstone strata to have high *Q* values. Therefore, by analyzing the result calculated by DCFS, the reasonable range of *Q* value implies that the low *Q* value area

corresponds well to gas reservoir whereas nonproductive well is identified by high Q value.

CONCLUSIONS

In this chapter, I developed a Q estimation method based on changes in the spectra of the original wavelet (defined by f_m) and the attenuated wavelet (defined by f_c). This method provides more robust estimation of Q than the most commonly used spectral ratio and central frequency shift algorithms. For reasons of mathematical clarity, the algorithm assumes a Ricker wavelet spectrum at the top of the target reservoir. However, the same workflow can be applied to data that have been spectrally balanced to exhibit a higher resolution. In this latter case, the relation between central frequency at depth and the dominant frequency of the original spectrum will provide a table look−up Q estimation.

CHAPTER 2 TABLES

SNR(dB)	SR		CFS		DCFS	
	Mean	SD	Mean	SD	Mean	SD
30	30.38	0.56	28.60	0.87	31.20	0.15
10	32.32	7.25	34.53	13.52	31.53	0.85
5	38.54	29.30	39.37	42.41	31.84	3.25
0	159.77	1540	28.36	89.35	32.36	3.28
-1	52.17	209.28	308.95	3103	32.63	3.65

Table 2.1. Statistical data calculated from 100 realizations using the SR, CFS and DCFS methods. The actual *Q* value is 30. SD denotes the standard deviation. Note that *Q* values from the SR and CFS methods can be negative.

CHAPTER 2 FIGURES

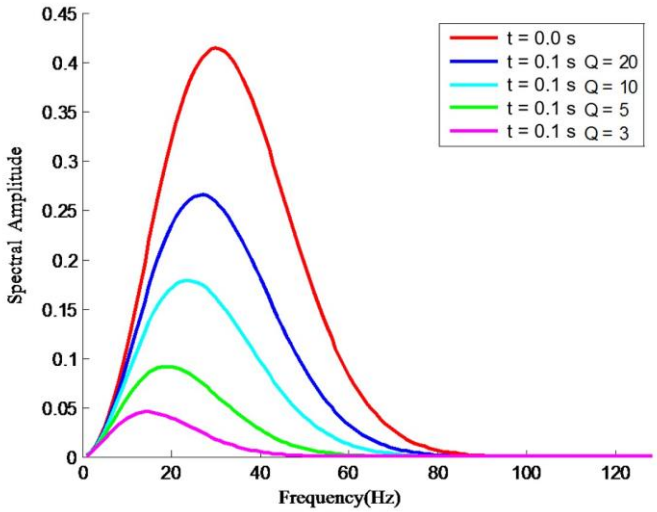

Figure 2.1. The frequency spectra of a Ricker wavelet with 30 Hz dominant frequency at time t=0 (red) and time t=0.1s in different attenuating medium with different Q values showing the loss in frequency and amplitude reduction.

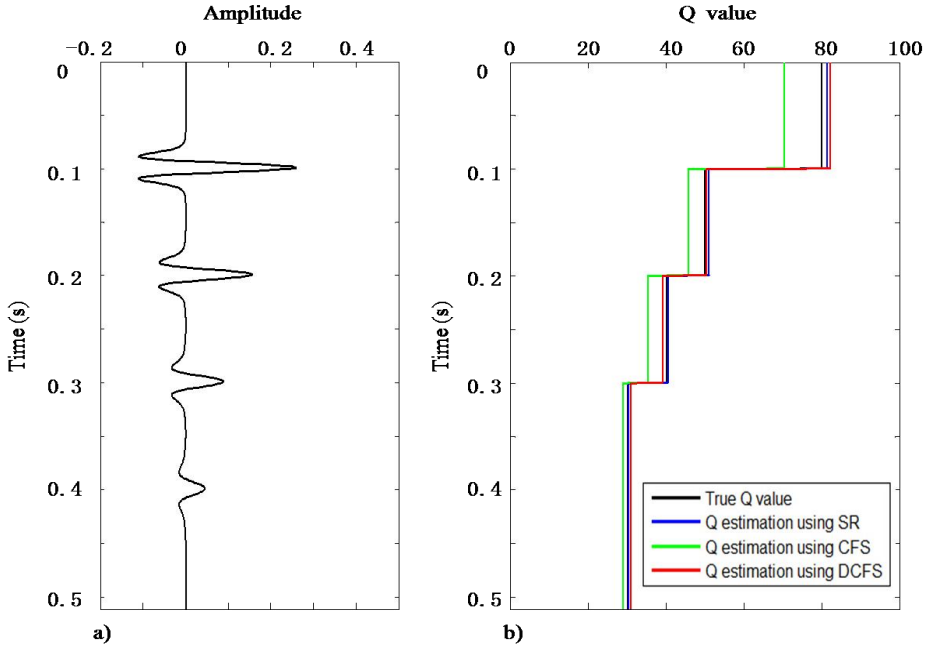

Figure 2.2. An example of Q estimation. (a) A noise-free synthetic generated using a 40 Hz Ricker wavelet with Q values of 80, 50, 40 and 30. (b) The results of Q estimation using the SR, CFS, and DCFS methods.

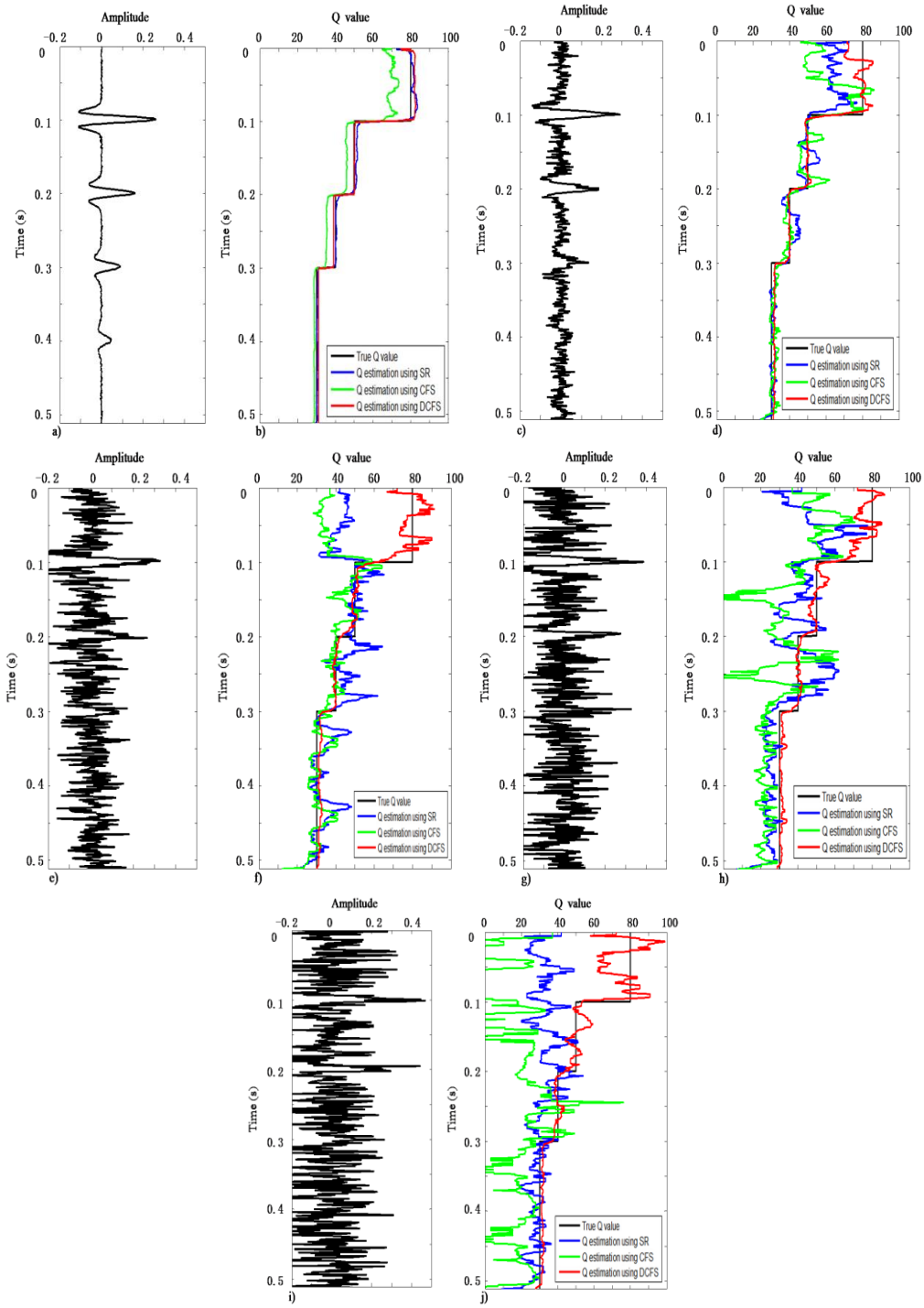

Figure 2.3. Comparison between SR, CFS and DCFS methods for a synthetic (same as Figure 2.2a) with additive random noise. (a), (c), (e), (g) and (i) respectively show the synthetic with SNR=30, 10, 5, 0, and -1 dB. (b), (d), (f), (h) and (j) show the corresponding the results of *Q* estimation using SR, CFS and DCFS methods. Note that the results applied by DCFS method are closer to the true *Q* values than those of the other two methods with decreasing SNR.

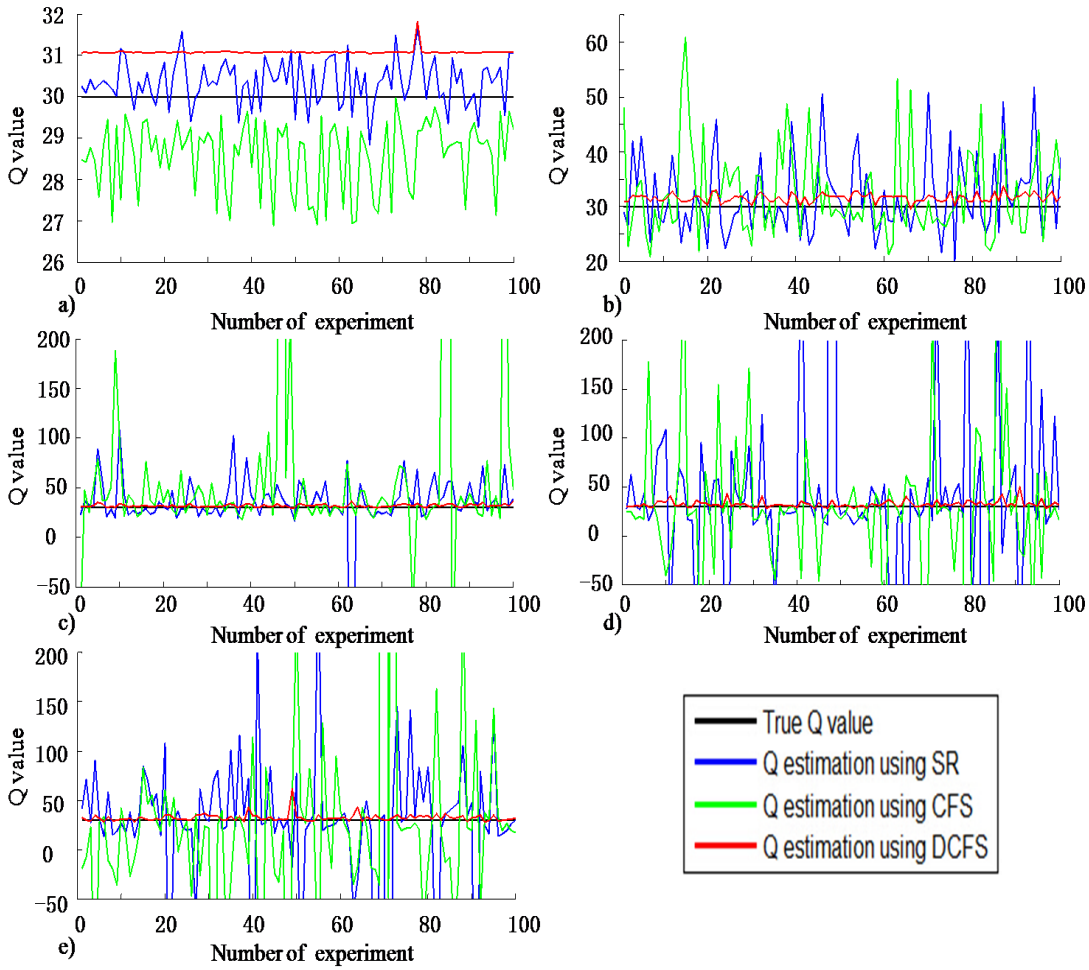

Figure 2.4. Estimation results of 100 independent experiments for the same layer of the synthetics with SNR = 30 (a), 10 (b), 5 (c), 0 (d), and -1 dB (e) using SR, CFS, and DCFS methods. The actual *Q* value is 30. Note that the results of the estimation, as denoted by the red curves, show that the DCFS method has the best robustness.

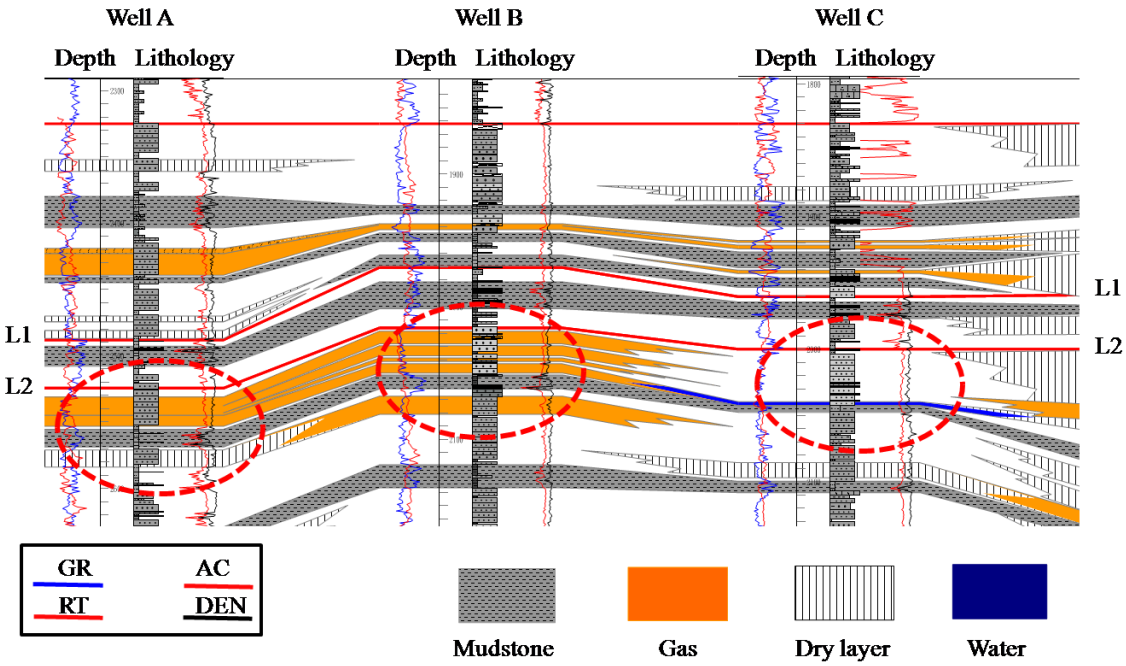

Figure 2.5. Geologic cross section through three wells showing the gas reservoir distribution, lithology, and well logs: gamma ray (GR), resistivity (RT), acoustic (AC) and density (DEN) through three joint wells. Red ovals denote the zones withn the target layer L2.

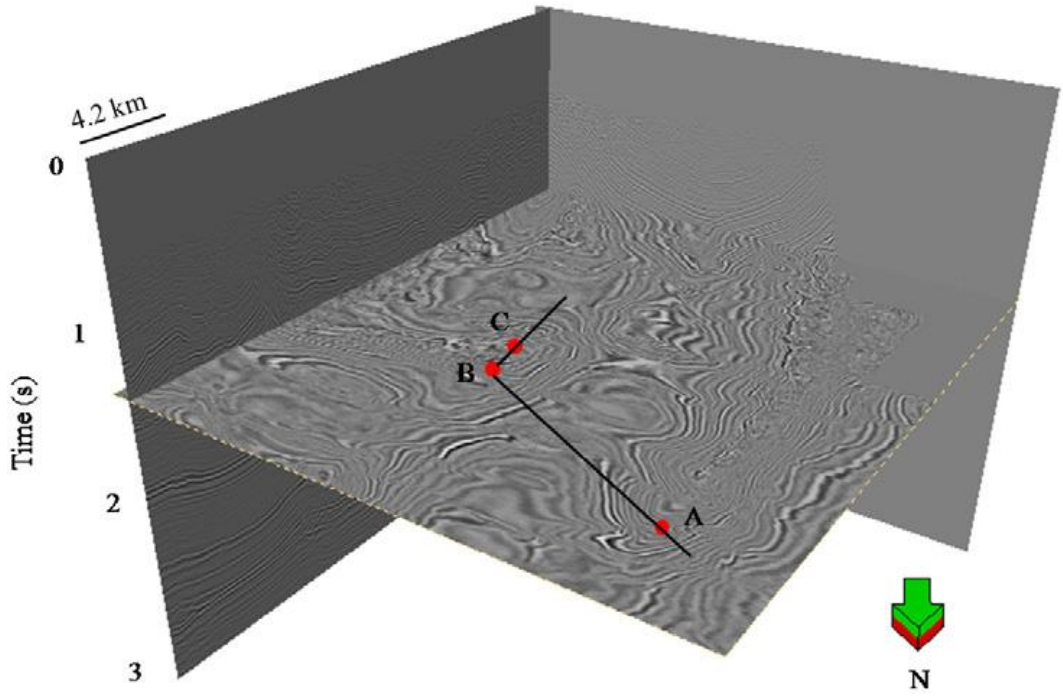

Figure 2.6. The configuration of the 3D land survey. Red dots show the positions of three wells. Black line denotes the random line shown in Figure 2.5.

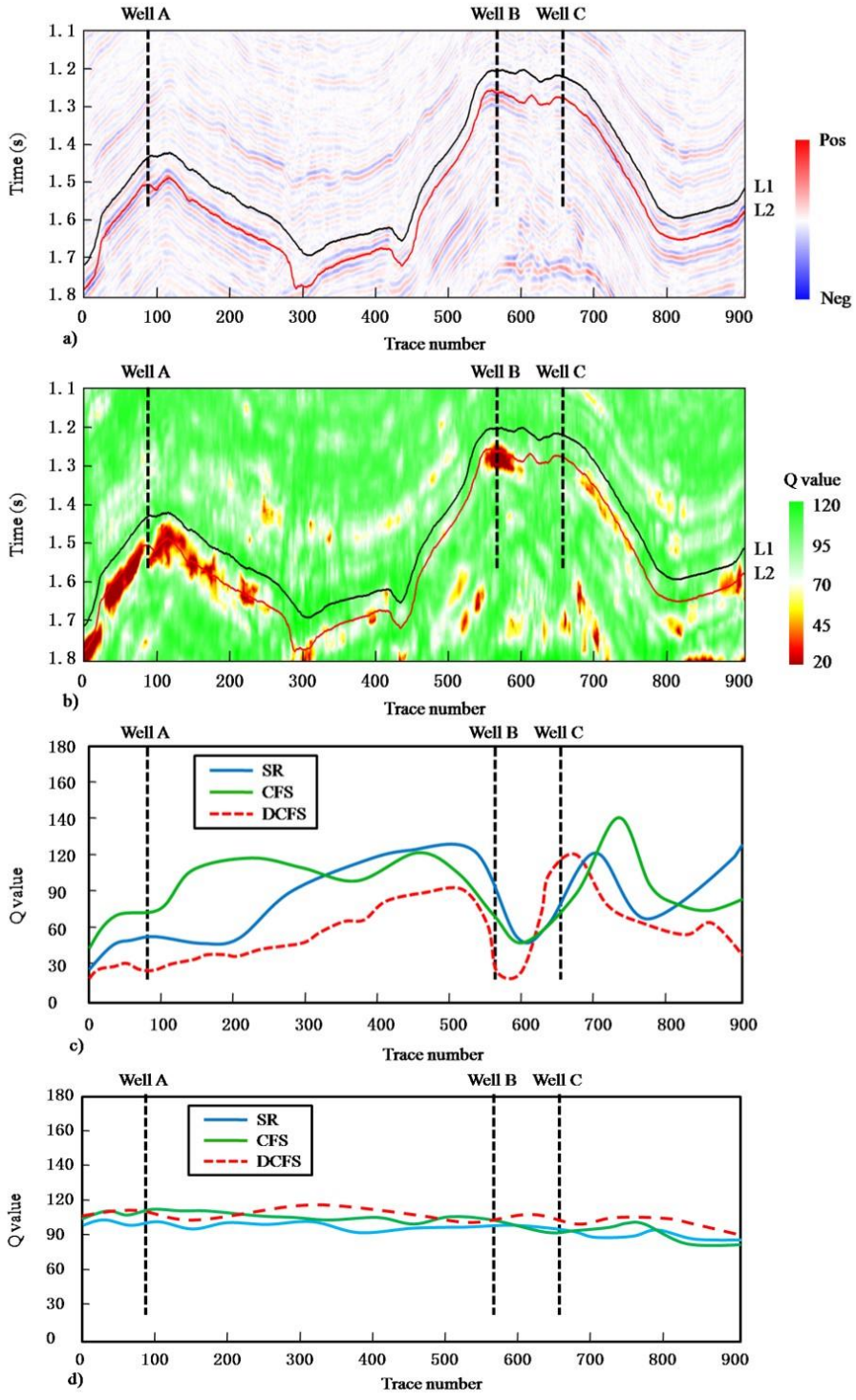

Figure 2.7. Application to the field data. (a) Vertical slice through the seismic amplitude volume connecting the three wells. (b) The continuous *Q* profile obtained by DCFS method. (c) Estimation of average *Q* values calculated by SR, CFS, and DCFS methods for target layer L2 20 ms below and (d) 10 ms below the top of L1. Results using the DCFS method are denoted by a red dashed line in (c) and (d).

REFERENCES

Barnes, A. E., 1991, Instantaneous frequency and amplitude at the envelope peak of a constant-phase wavelet: Geophysics, **56**, 1058-1060.

Brzostowski, M. and G. McMechan, 1992, 3-D tomographic imaging of near-surface seismic velocity and attenuation: Geophysics, **57**, 396–403.

Clark, R. A., A. J. Carter, P. C. Nevill, and P. M. Benson, 2001, Attenuation measurements from surface seismic data—Azimuthal variation and time lapse case studies: 63rd Conference and Technical Exhibition, EAGE, Expanded Abstracts, L-28.

Engelhard, L., 1996, Determination of seismic-wave attenuation by complex trace analysis: Geophysical Journal International, **125**, 608–622.

Gao J., S. Yang, D. Wang, and R. Wu, 2009, Quality factors estimation using wavelet's envelope peak instantaneous frequency: SEG Technical Program Expanded Abstracts 2009, 2457-2461.

Hauge, P. S., 1981, Measurements of attenuation from vertical seismic profiles: Geophysics, **46**, 1548–1558.

Hedlin, K., L. Mewhort, and G. Margrave, 2001, Delineation of steam flood using seismic attenuation: SEG Expanded Abstracts, **20**, 1572–1575.

Hu, C., N. Tu, and W. Lu, 2013, Seismic attenuation estimation using an improved frequency shift method: IEEE Geoscience and Remote sensing Letters, **10**(5), 1026-1030.

Kaderali, A., M. Jones, and J. Howlett, 2007, White Rose seismic with well data constraints: A case history: The Leading Edge, **26**, 742–754.

Kjartansson, E., 1979, Constant Q-wave propagation and attenuation: Journal of Geophysical Research, **84**, 4737–4748.

Korneev, V. A., G. M. Goloshubin, T. M. Daley, and D. B. Silin, 2004, Seismic low-frequency effects in monitoring fluid-saturated reservoirs: Geophysics, **69**, 522–532.

Li, H., W. Zhao, H. Cao, F. Yao, and L. Shao, 2006, Measures of scale based on the wavelet scalogram with applications to seismic attenuation: Geophysics, **71**, 111–118.

Luh, P. C., 1993, Wavelet attenuation and bright-spot detection, in Castagna, J. P. and M. M. Backus eds., Offset-dependent reflectivity: Theory and practice of AVO analysis: Investigations in Geophysics, **8**, 190–198.

Matheney, M .P., and R. L. Nowack, 1995, Seismic attenuation values obtained from instantaneous frequency matching and spectral ratios: Geophysical Journal International, **123**, 1–15.

Maultzsch, S., M. Chapman, E. Liu, and X. Y. Li, 2007, Modelling and analysis of attenuation anisotropy in multi-azimuth VSP data from the Clair field: Geophysical Prospecting, **55**, 627–642.

Parra, J. O. and C. L. Hackert, 2002, Wave attenuation attributes as flow unit indicators: The Leading Edge, **21**, 564–572.

Quan, Y., and J. M. Harris, 1997, Seismic attenuation tomography using the frequency shift method: Geophysics, **62**, 895–905.

Raikes, S. A., and R. E. White, 1984, Measurements of earth attenuation from downhole and surface seismic recordings: Geophysical Prospecting, **32**, 892–919.

Rein, C., M. van dan Baan, and R. Clark, 2009, The robustness of seismic attenuation measurement using fixed and variable-window time-frequency transform: Geophyics, **74**(2), WA123-WA135.

Ricker, N., 1953, The form and laws of propagation of seismic wavelets: Geophysics, **18**, 10–40.

Sams, M. S., and D. Goldberg, 1990, The validity of Q estimates from borehole data using spectral ratios: Geophysics, **55**, 97-101.

Singleton, S., M. T. Taner, and S. Treitel, 2006, Q estimation using Gabor-Morlet joint time-frequency analysis techniques: SEG Extended Abstracts, **25**, 1610-1614.

Toksöz, M. N., D. H. Johnston, and A. Timur, 1979, Attenuation of seismic waves in dry and saturated rocks: I. Laboratory measurements: Geophysics, **44**, 681–690.

Tonn, R., 1991, The determination of the seismic quality factor Q from VSP data: A comparison of different computational methods: Geophysical Prospecting, **39**, 1–27.

Wang, Y., 2002, A stable and efficient approach of inverse Q filtering: Geophysics, **67**, 657–663.

Wang, Y., 2006, Inverse Q-filter for seismic resolution enhancement: Geophysics, **71**(3), V51-V60.

Wang, Y., 2008, Seismic Inverse Q Filtering: Malden: Blackwell Publishing.

Wang, Y., 2015, Frequencies of the Ricker wavelet: Geophysics, **80**(2), A31-A37.

White, R. E., 1992, The accuracy of estimating Q from seismic data: Geophysics, **57**, 1508–1511.

Winkler, K. W., and A. Nur, 1982, Seismic attenuation—Effects of pore fluids and frictional sliding: Geophysics, **47**, 1–15.

Wright, C., and D. Hoy, 1981, A note on pulse broadening and anelastic attenuation in near-surface rocks: Physics of the Earth and Planetary Interiors, **25**, P1–P8.

Yang, S., and J. Gao, 2010, Seismic attenuation estimation from instantaneous frequency: IEEE Geoscience and Remote Sensing Letters, **7**, 113–117.

Zhang, C. J., and T. J. Ulrych, 2002, Estimation of quality factors from CMP records: Geophysics, **67**, 1542–1547.

Zhu, Y., and I. Tsvankin, 2007, Plane-wave attenuation anisotropy in orthorhombic media: Geophysics, **72**(1), D9–D19.

CHAPTER 3
SPECTRALLY CORRECTED ATTENUATION ESTIMATION[3]

ABSTRACT

Unconventional resource play is critical in petroleum exploration and development. Fluid-filled formations directly modify the effective impedance of rocks, attenuate amplitude and distort seismic spectrum, which all make the seismic attenuation estimation a promising tool for characterizing fracture system. However, existing methods for seismic attenuation are usually based on a "Constant *Q*" model, which ignores the interference from reflectivity anomalies. For unconventional reservoirs, the spectrum of the reflected wave may be affected by the presence of thin beds (shales) in the formation, which makes *Q* estimates less reliable. I employ a non-stationary *Q* model to characterize attenuation, and correct the reflected spectrum by using the inverted reflectivity sequence to remove local thin-bed effects from seismic reflection data. In synthetic examples, significantly less variance in the estimated values and fewer unphysical negative *Q* values are obtained. Following the workflow, I also applied this attenuation estimation on Barnett shale data. The recovered *Q* estimates have a good correlation with the production data. Though, the attribute is the average over a target horizon, this may be sufficient to find evidence of fluid-filled fractures, change in lithology, or high TOC content.

---

[3] *This study is published as a journal paper - Li, F., H. Zhou, T. Zhao, K.J. Marfurt, 2016, Unconventional Reservoir Characterization based on Spectrally Corrected Seismic Attenuation Estimation: Journal of Seismic Exploration, **25**, 447-461.*

INTRODUCTION

Identifying highly fractured zones or sweet spots in naturally fractured reservoirs is important where fractures often act as significant conduits for fluid flow (Burns, 2004). Lynn (2015) reports changes in attenuation as a function of fracture orientation for natural fractures. In addition to fractures, shales are also expected to exhibit strong attenuation associated with microcracks with possibly new loss mechanisms linking attenuation to kerogen maturity and organic content (Lynn and Beckham, 1998). Thus, seismic attenuation may play a crucial role in the exploration and exploitation of unconventional hydrocarbon resources.

Existing basic methods for seismic attenuation, such as the spectral ratio method (White, 1992), the frequency shift methods (Quan and Harris, 1997; Zhang and Ulrych, 2002), measure quality factor (Q) based on the variance of the seismic wavelet spectra. However, the classic "constant Q" model ignores the change in spectra due to reflectivity anomalies. For unconventional reservoirs, the spectrum of the reflected wave may be affected by the presence of thin beds in the formation, which makes Q estimates less reliable.

Hackert and Parra (2004) proposed using the known reflectivity sequence from a nearby well log to correct the local spectrum. Inspired by their work, and considering unconventional reservoirs, I employ a new Q model to estimate seismic attenuation, and correct the reflected spectrum by removing local thin-bed effects from seismic reflection data. One can use well logs to build a background model, estimate a source wavelet, and invert seismic amplitude volume to construct an impedance volume of the whole survey. I will use this impedance volume to compute the reflectivity sequence to correct the

reflected spectrum. I validate my workflow on synthetic data and apply it to a Barnett Shale survey.

TIME-VARIANT SPECTRAL MODEL

When a seismic wave propagates in a viscoelastic medium in a constant linear frequency attenuation model, the spectral amplitude decreases exponentially with travel time and 1/*Q* (Aki and Richards, 2002)

$$A(f,t) = S(f)\exp\left(-\frac{\pi ft}{Q}\right), \tag{3.1}$$

where, $S(f)$ is the source wavelet spectrum, t is the travel time, and $A(f,t)$ is the received signal spectrum including all geometric spreading, source, and receiver effects. In this model, the quality factor *Q* is constant on all frequencies.

Sheriff and Geldart (1995) use a simple convolution model (noise free) to define the reflected signal, $a(t)$:

$$a(t) = \int_{-\infty}^{\infty} s(\tau) r(t-\tau)\,\mathrm{d}\tau, \tag{3.2}$$

where, $s(t)$ is source wavelet, and $r(t)$ is reflectivity series. In this model, seismic signal is the convolution of source wavelet and reflectivity sequence.

The frequency expression of convolution model is

$$A(f) = S(f)R(f), \tag{3.3}$$

where, $A(f)$, $S(f)$ and $R(f)$ are the Fourier transforms of seismic signal, source wavelet, and reflectivity series, respectively. If the medium is attenuating with constant *Q*, then the spectrum will be reduced:

$$A(f,t) = S(f)R(f)\exp\left(-\frac{\pi ft}{Q}\right). \tag{3.4}$$

Compared Equation 3.1 with Equation 3.4, constant *Q* model ignores the reflection coefficient effects. The approximation is valid if the reflectivity coefficient is assumed to be random with a white spectrum, as if constant *Q* model is mainly dealing a single layer. Although the reflectivity may be white at a large scale, the local reflectivity spectrum is not white. Shale resource plays are in general comprise of alternating brittle and ductile layers. Thus, one should consider the local reflectivity change, which would distorts the seismic spectrum.

Grossman et al. (2001) introduced a non-stationary convolution model, which is actual a more generalized form of Equation 3.4, to do the attenuation estimation:

$$A(f,t) = S(f)\alpha(f,t)R(f), \tag{3.5}$$

where $\alpha(f,t)$ is the attenuation factor expression in the frequency domain. This formula can be rearranged to (Grossman et al., 2001) :

$$\frac{A(f,t)}{R(f)} = S(f)\alpha(f,t). \tag{3.6}$$

If I can obtain the estimation of the local reflectivity coefficient sepctra *R(f),* I can suppress the interference of the local geology, which can lead to more accurate *Q* estimation.

LOCALIZED SPECTRAL CORRECTION

Assume that there are two local subset of reflectors $r_1(t)$ and $r_2(t)$ near time t_1 and t_2, respectively. Then, I can express their spectra as:

$$A_1(f,t_1) = S(f)R_1(f)\exp\left(-\frac{\pi f t_1}{Q}\right), \quad \textit{and}$$
$$A_2(f,t_2) = S(f)R_2(f)\exp\left(-\frac{\pi f t_2}{Q}\right). \tag{3.7}$$

Taking the logarithm of their ratio,

$$\ln\left(\frac{A_1(f,t_1)}{A_2(f,t_2)}\right) = \ln\left(\frac{R_1(f)}{R_2(f)}\right) - \frac{\pi f(t_1 - t_2)}{Q}. \tag{3.8}$$

If there is no reflectivity anomaly, the ratio of R_1 and R_2 is independent of frequency, so the first term on the right-hand side is constant, and Q can be estimated form the slope of the log-spectral ratio of A_1 and A_2. However, if there are spectral anomalies associated with layering, then the first term on the right-hand side varies with frequency, and the spectral slope is not simply related to Q.

Therefore, one needs to correct for the interference from the reflectivity coefficient. When the well-log impedance data available, I can compute the reflectivity of the well position. In my work, I use a commercial software package to invert the amplitude volume for the seismic impedance. I then compute reflection coefficients to correct the spectra.

After computing the reflectivity spectrum, one moves the first term on the right-band side of Equation 3.8 to the left-hand side to obtain:

$$\ln\left(\frac{A_1(f,t_1)/R_1(f)}{A_2(f,t_2)/R_2(f)}\right) = -\frac{\pi f(t_1 - t_2)}{Q}. \tag{3.9}$$

Note that the $\frac{A(f,t)}{R(f)}$ is a local spectrum correction, after which one can use the Q estimation methods, for example, central frequency shift method, on the spectrally corrected results.

To sum up, this method has the following steps (Figure 3.1):

(1) Select a reference reflection and some target reflections; at the same time, invert the seismic amplitude data to obtain impedance; Then, compute reflectivity from the impedance;

(2) In order to estimate the local reflection spectra, computation of a windowed time-frequency transform should be applied in a local (short time window) period. The time window should be short enough to select the reflection of interest but long enough to assure the frequency resolution;

(3) Correcte the spectrum using *R(f)*;

(4) Use a *Q* estimation method to compute *Q* values.

INTERFERENCE FROM ILL-SPACED REFLECTORS

As we know, the reflected data come from the convolution of the source wavelet with the reflectivity series. For a relatively long time range, the reflectivity sequence is often assumed to be random and may be approximated by a white spectrum. However, the localized reflection spectrum can be distorted by ill spaced reflectors. Figure 3.2 shows a possible interference phenomena. For a single reflector (Figure 3.2a), there is no spectral distortion. For the three evenly spaced reflectors shown in Figure 3.2c, the reflection spectrum is enhanced near 45Hz and suppressed near 15Hz and 75Hz, which shows that local reflectivity can result in constructive and destructive interference at certain frequencies. Figure 3.2e shows closely but randomly spaced reflectors, the reflected spectrum may be affected irregularly. It could suppress low-frequency content in the combined reflection because of the possible low frequency notches, as in this case,

which will give the appearance of negative *Q* through increased amplitude at high frequencies.

SYNTHETIC THIN-BED EXAMPLE

I built a synthetic example consisting of five layers (four reflectors), each with different *Q* and P-velocity (Figure 3.3). The source pulse is a Ricker wavelet of 100-Hz central frequency. I set up two cases on this model: one with no thin beds, and the second case with thin beds added, as shown in Figure 3.3. From Figure 3.2, one can infer that the reflectivity sequences with thin beds are distorted.

The uncorrected and corrected normalized local spectra of the four reflections are shown in Figure 3.4. The blue curves are the ideal reflected spectra without thin beds, while red curves are the uncorrected spectra for reflections including thin beds, and the black dotted lines are the spectrum with the local spectral correction. Ideally, the corrected spectrum (dashed line) would exactly match the ideal spectrum (blue curve). This does not happen because I have smoothed out the zeroes in the spectrum of the reflectivity sequence.

The first reflection is the reference. One computes the average *Q* between the reference and each later reflection using both the uncorrected and corrected spectra (Table 3.1). Only the central frequency shift (CFS) method is used. Without thin beds present, the method recovers the *Q* of each layer almost exactly. The thin beds at the layer boundaries of the second model, however, interfere with the reflection spectra in the manner discussed above, so that *Q* values of the uncorrected CFS method are quite poor. Applying the well-log–based spectral correction substantially removes this effect, and the corrected *Q* values are of reasonable accuracy.

FIELD DATA APPLICATION

The Barnett Shale is a very important unconventional shale gas system in the Fort Worth Basin (FWB), Texas where it serves as a source rock, seal, and trap (Perez, 2009). The reservoir was deposited between the Mable Falls Limestone and Viola unconformity and separated by the Forestburg Limestone into the Upper Barnett and the Lower Barnett. The Viola and Forestburg formations are not producible and provide barriers to fracture growth. Figure 3.5 shows the seismic data and the interpreted Upper Barnett Shale and Lower Barnett Shale.

Figures 3.6 and 3.7 show the time structure map and curvature attributes along the base Lower Barnett Shale. Seismic attributes show great promise in delineating fracture systems (Chopra and Marfurt, 2008), and has proven to be successful. From Figure 3.7, because the fracture scale is below the seismic resolution, we can only infer potential fracture locations, which might be larger along more strained (curved) parts of the survey.

I applied central CFS method to estimate Q value, as shown in Figure 3.8, in which attenuation means $1/Q$. This result has high correlation with the attributes in Figure 3.7 as well as the production data (productive well locations). Almost all the well locations show high attenuation. What's more, this result also display high correlation with the TOC prediction by Verma et al. (2012). Although it seems so good, there are so many unphysical negative Q values in the result.

In order to compensate for the spectral interference from thin beds, following the workflow in Figure 3.1, I do the Q estimation again. The reference and target reflections are already picked. First, I invert the seismic impedance volume using well logs (e.g.

density and Vp) and the seismic amplitude volumes. Figure 3.9 shows two vertical well logs. The reflectivity is not random, which means the spectral correction is important.

Figure 3.11 shows the improved attenuation estimation result. Compared to Figure 3.8, the upper left area of Figure 3.11 has more positive *Q* values, which makes more sense. But for the bottom right area, there are still many negative values. This error inspired the construction of the DCFS algorithm described in Chapter 2.

CONCLUSIONS

The current "constant *Q*" model is inadequate to describe attenuation caused by fracture system and unconventional reservoirs. Reflected wavelets can be distorted by the thin beds, which makes it more difficult to estimate reliable attenuation information. Based on non-stationary convolution model, I demonstrated the successful use of a spectral correction method for improving *Q* estimation. I applied the method on synthetic examples, and *Q* values computed using the corrected spectra have less variance and fewer negative values than those computed with uncorrected spectra.

Using the local corrected spectra of the target and reference reflections, I compute *Q* of the Barnett shale using the centroid frequency shift method. The recovered *Q* estimates have a good correlation with the production data with less negative *Q* values. With the comparison between the results I obtained and the attributes associated with fracture delineation, I can determine that the estimation of seismic attenuation can be a useful tool to evaluate the fracture density, when the valuable information from the well log tied to the seismic data is adopted appropriately. In the future work, detailed attenuation models should use specific and spatially localized and unambiguous physical properties, if possible.

CHAPTER 3 TABLES

	True Value	Estimation without thin beds	Estimation with thin beds (uncorrected)	Estimation with thin beds (corrected)
Layer 1	40	37.2	81.5	37.9
Layer 2	30	31.2	16.5	31.1
Layer 3	50	47.2	-307	44.6
Layer 4	20	20.6	5	20.4

Table 3.1. True and computed values of *Q* from the synthetic test data, for cases of no thin beds and thin beds added. When thin beds are present, *Q* values are computed with and without the spectral correction technique.

CHAPTER 3 FIGURES

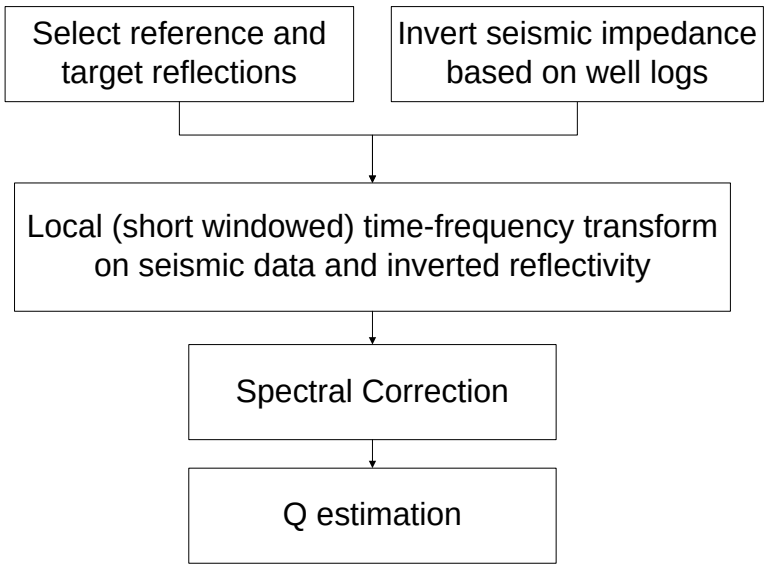

Figure 3.1. Workflow of the well-log based local spectral correction *Q* estimation.

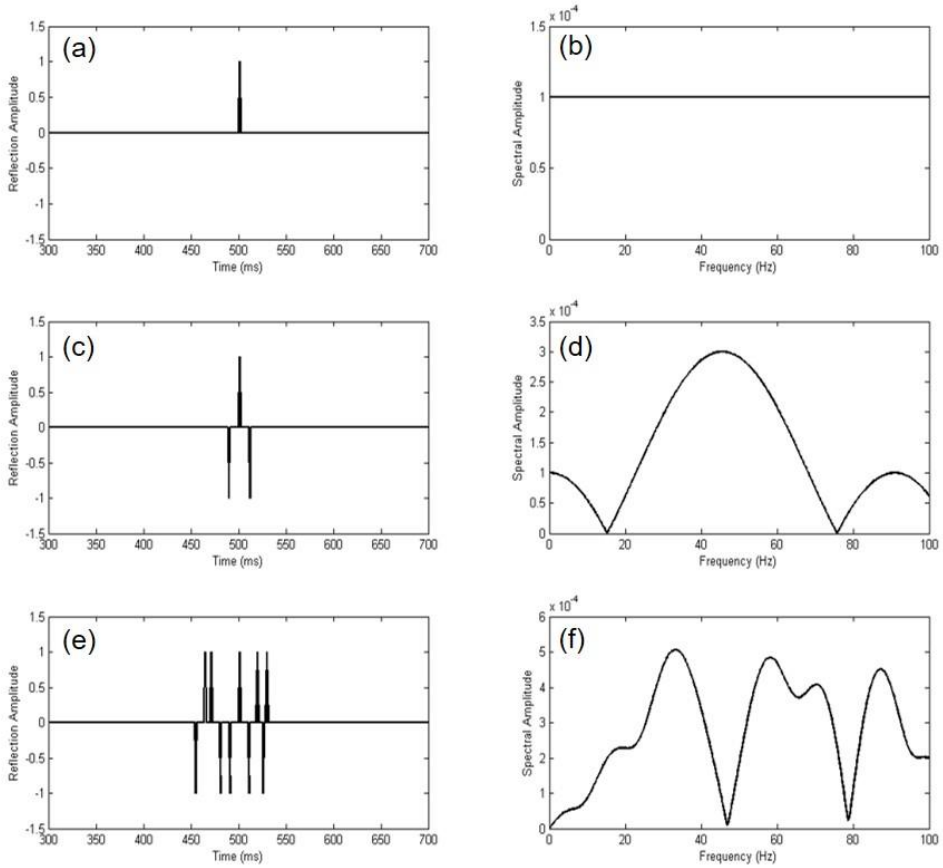

Figure 3.2. Three hypothetical spike reflectivity sequences and their corresponding spectra.

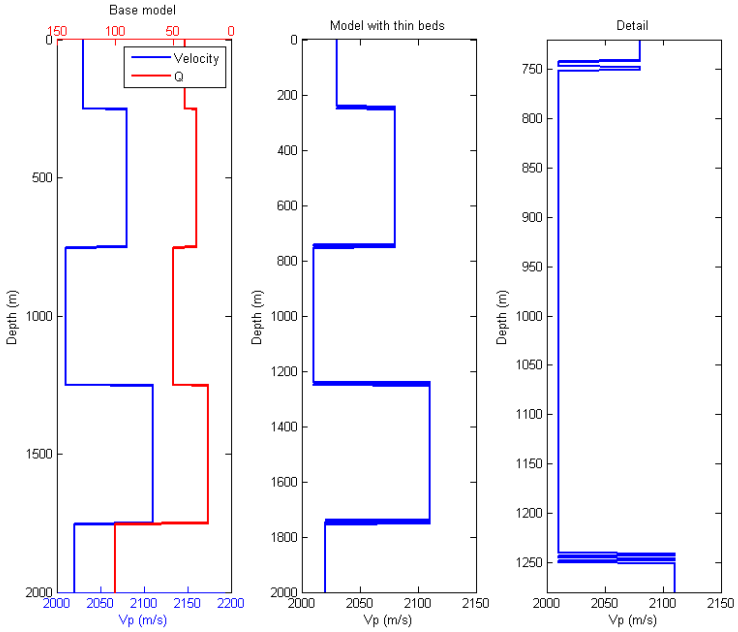

Figure 3.3. Velocity models for synthetic seismic reflection data without and with thin beds added.

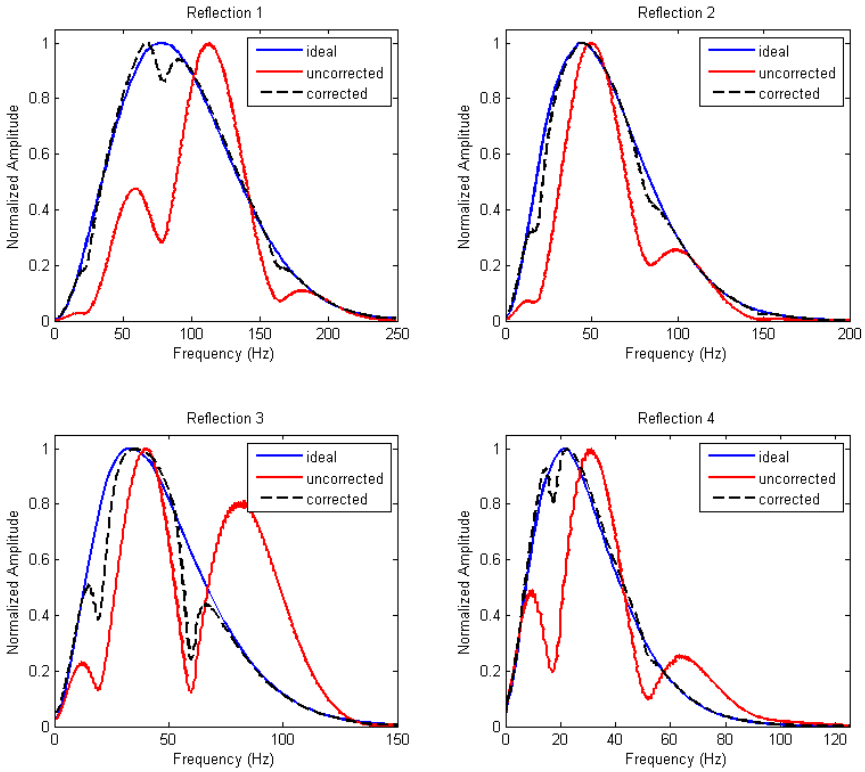

Figure 3.4. Comparison between uncorrected and corrected normalized local reflection spectra. In each figure, the blue line is the spectrum if there are no thin beds. The red line is the spectrum with thin beds. The black dashed line is the corrected spectrum. Note that not all frequency axes span the same range.

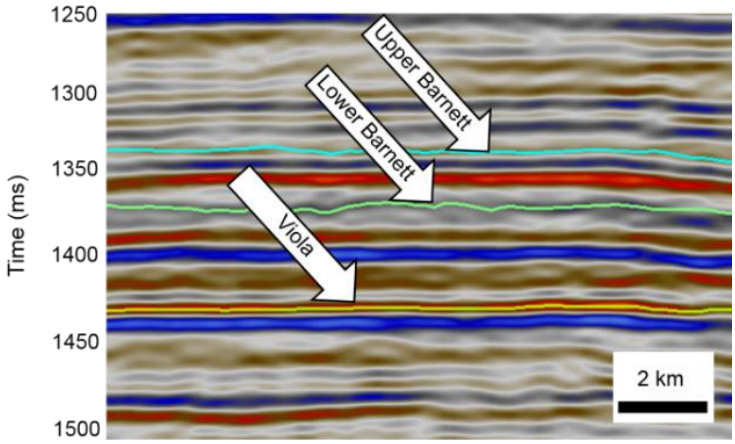

Figure 3.5. Seismic data and interpreted horizons.

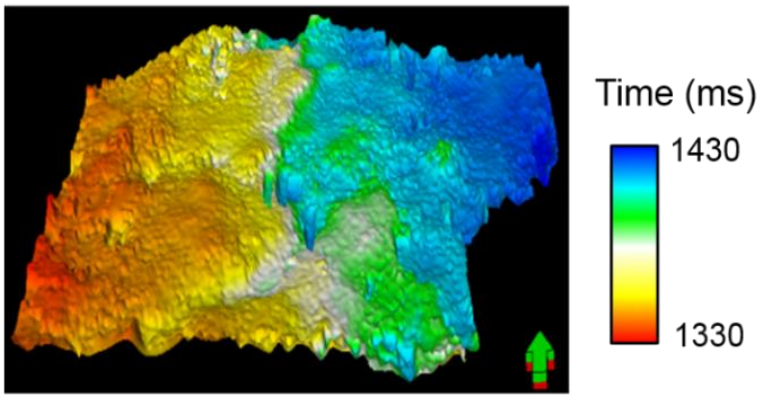

Figure 3.6. Time structure map of Lower Barnett shale.

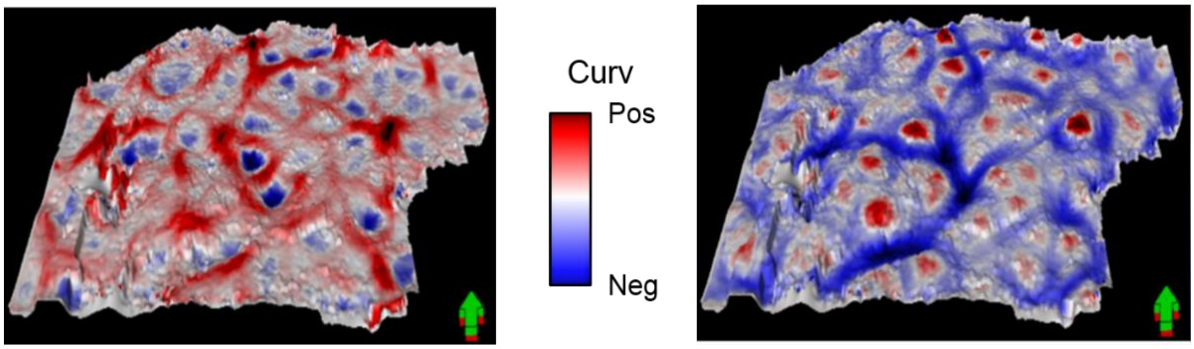

Figure 3.7. Attributes horizon slices from Lower Barnett Shale with (left) most positive curvature, (right) most negative curvature.

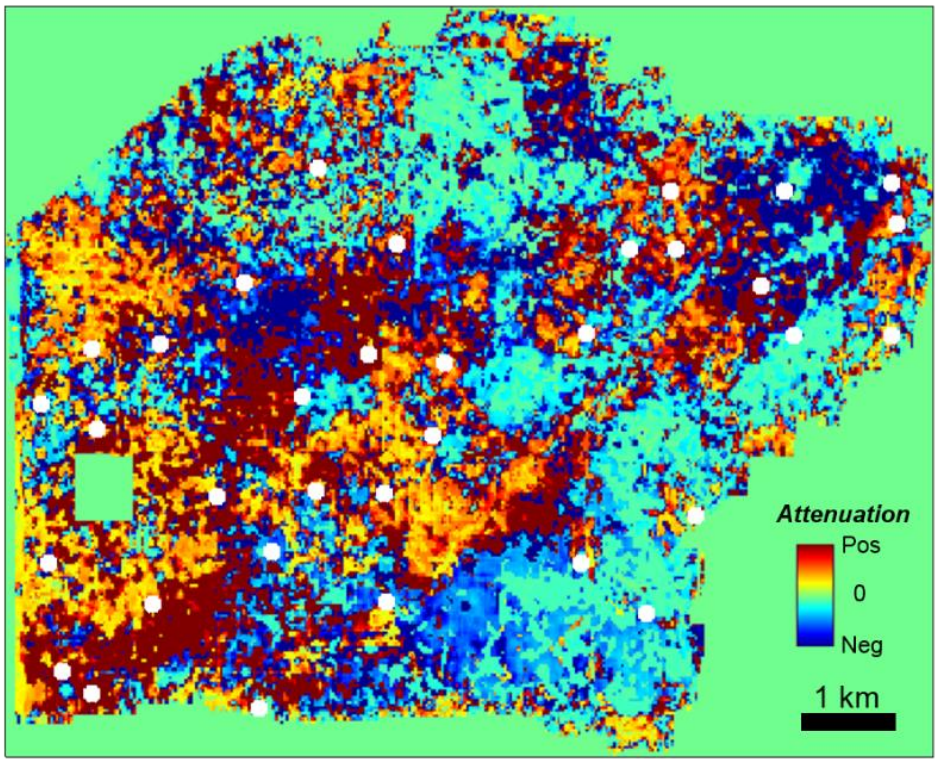

Figure 3.8. Attenuation estimation from uncorrected spectra using the CFS method. White circles denote productive well locations.

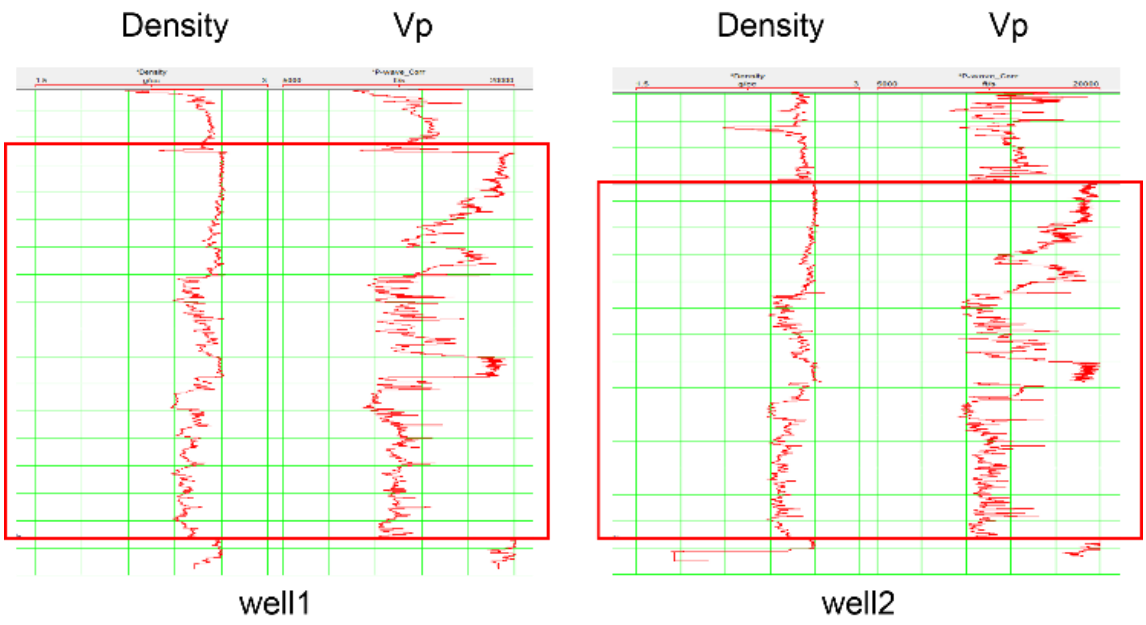

Figure 3.9. Well log examples in the survey. Red frames denote the lower Barnett Shale, which doesn't have a white spectrum.

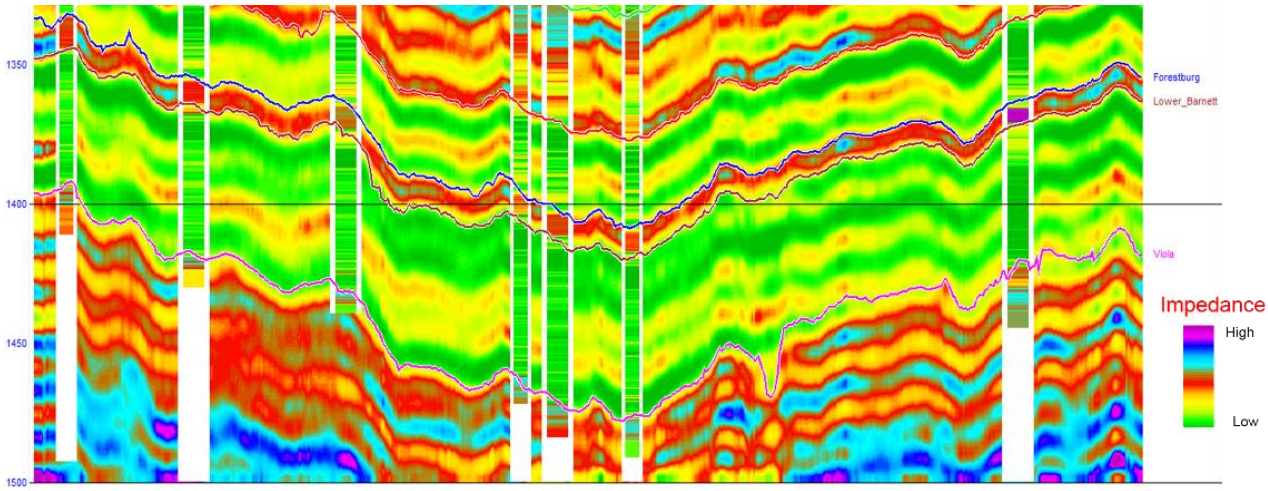

Figure 3.10. Inverted seismic impedance profile along an arbitrary line shown on the right. Note the inverted result has a good correlation with the well logs.

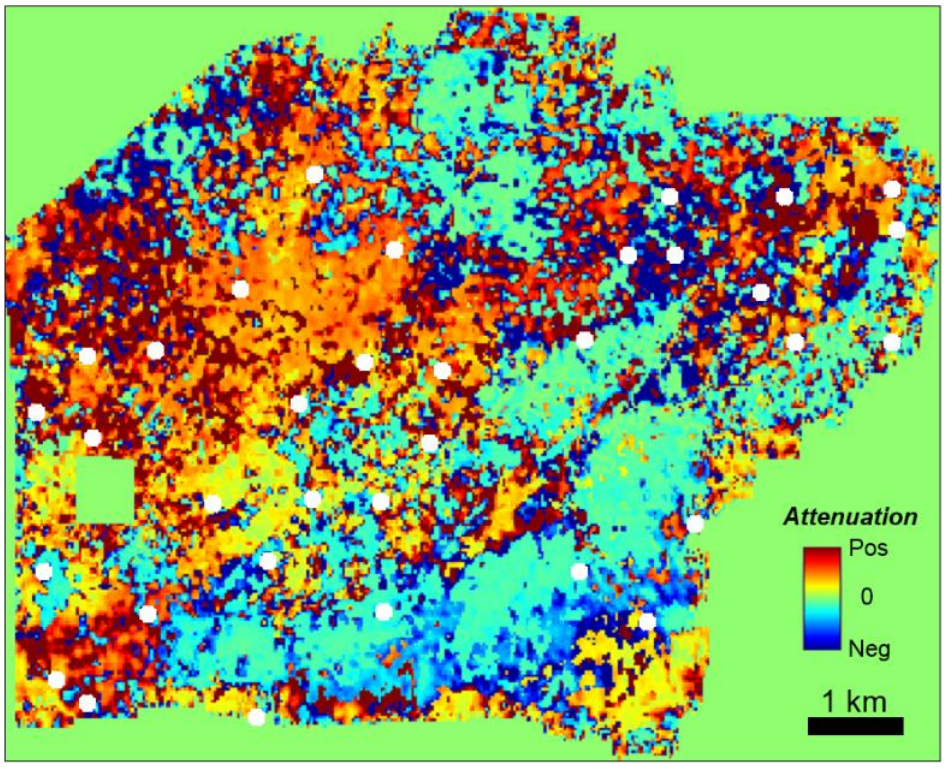

Figure 3.11. Attenuation estimation from the corrected spectra using the CFS method. White circles denote productive well locations.

REFERENCES

Burns, D.,M. E.Willis, B. Minsley, and M. N. Toksöz, 2004, Characterizing subsurface fractures from reflected and scattered seismic energy: 112th SEGJ Conference.

Chopra, S., and K. J. Marfurt, 2008, Emerging and future trends in seismic attributes: The Leading Edge, **27**, 298-318.

Dasgupta, R., and R. A. Clark, 1998, Estimation of Q from surface seismic reflection data: Geophysics, **63**, 2120–2128.

Grossman, J. P., G. F. Margrave, M. P. Lamoureux, and R. Aggarwala, Constant-Q wavelet estimation via a nonstationary Gabor spectral model, tech. rep., CREWES, University of Calgary, 2001.

Hackert, C. L. , and J. O. Parra, 2004, Improving Q estimates from seismic reflection data using well-log-based localized spectral correction: Geophysics, **69**, 1521–1529.

Hauge, P. S., 1981, Measurements of attenuation from vertical seismic profiles: Geophysics, **46**, 1548–1558.

Lynn, H., and W. Beckham, 1998, P-wave azimuthal variations in attenuation, amplitude and velocity in 3D field data: Implications for mapping horizontal permeability anisotropy: 68th SEG Annual Meeting, 193–196.

Lynn, H., W. Lynn, J. Obilo, and V. Agarwal, 2015, Azimuthal pre-stack depth migration for in-situ stress evaluation in a fractured carbonate oil reservoir: predrill prediction of Instantaneous Shut-In Pressure gradients: GSOC talk.

Perez, R., Quantitative petrophysical characterization of the Barnett shale in Newark east field, Fort Worth Basin : M. S. thesis, University of Oklahoma, 2009.

Quan, Y., and J. M. Harris, 1995, Seismic attenuation tomography using the frequency shift method: Geophysics, **62**, 895–905.

Sheriff, R. E., and L. P. Geldart, Exploration seismology, 2nd ed., Cambridge University Press: 1995.

Verma, S., A. Roy, R. Perez, K. J. Marfurt, 2012, Mapping high frackability and high TOC zones in the Barnett Shale: Supervised Probabilistic Neural Network vs. unsupervised multi-attribute Kohonen SOM: SEG Annual Meeting, 1-5.

White, R. E., 1992, The accuracy of estimating Q from seismic data: Geophysics, **57**, 1508–1511.

Zhang, C. J., and T. J. Ulrych, 2002, Estimation of quality factors from CMP records: Geophysics, **67**, 1542–1547.

CHAPTER 4
SEISMIC ATTENUATION ATTRIBUTES WITH APPLICATIONS ON CONVENTIONAL AND UNCONVENTIONAL RESERVOIRS[4]

ABSTRACT

Seismic attenuation, generally related to the presence of hydrocarbon accumulation, fluid-saturated fractures, and rugosity, is extremely useful for reservoir characterization. The popular constant attenuation estimation model, focusing on intrinsic attenuation, intentionally detects the seismic energy loss because of the presence of hydrocarbons, but it works poorly when spectral anomalies, due to the existence of rugosity, fractures, thin layers and so on. Instead of trying to adjust the classic attenuation model to such phenomena, I evaluate a suite of seismic spectral attenuation attributes to quantify the apparent attenuation response. I apply these attributes to a conventional and an unconventional reservoir, and find those seismic attenuation attributes are effective and robust for seismic interpretation. Specifically, the spectral bandwidth attribute correlates to production of a gas sand in the Anadarko Basin, whereas the spectral slope of high frequencies attribute correlates to the production in the Barnett Shale of the Fort Worth Basin.

---

[4] *The major part of this study is published as a journal paper - Li F., S. Verma, H. Zhou, T. Zhao, and K. J. Marfurt, 2016, Seismic attenuation attributes with applications on conventional and unconventional reservoirs: Interpretation, **4**(1), SB 63–SB77.*

INTRODUCTION

Seismic attenuation can be reduced to a simple concept: when a seismic wave moves through a body of rock in the subsurface, higher frequencies of an incident seismic wave will attenuate faster than lower frequencies, showing a net loss of energy (Raikes and White, 1984). Extensive work has been done to measure energy attenuation in rocks under a variety of conditions. Some studies (Knight et al., 2010; Piane et al., 2014: Parra et al., 2015) show attenuation varying in response to changes in water saturation, clay content, porosity, pore geometry, permeability, micro-fracturing, and pressure. Seismic attenuation can be a powerful tool in indicating lithology, pore structure, fractures, and fluid content (Klimentos, 1995). In metals and crystalline rocks, the major contribution to energy loss is the movement of dislocations (Mason et al., 1978).

The seismic attenuation phenomenon is often closely related to the velocity dispersion effect in the laboratory and field applications. Velocity is affected by two main fluid-related modes at the pore scale when waves propagate in fluid-saturated rocks (Dvorkin and Nur, 1993): Biot's or global flow and local flow or squirt flow (Dvorkin et al., 1995). Calculation of the velocity of elastic waves that propagate in saturated rocks is complicated by many dispersion and attenuation mechanisms. The experiments based on different models have detected attenuation as well as dispersion due to dry bulk modulus with pressure, pore-scale, local-flow mechanism and fluid properties (Gurevich et al., 2010; Yao and Han, 2013; Spencer and Shine, 2016; Sayar and Torres-Verdín, 2017). In this dissertation, velocity dispersion is not studied, and only attenuation is discussed.

Attenuation can be ten times more sensitive to changes in saturation, clay content, pore fluids or pore pressure than velocity and densities (Klimentos, 1995; Clark et al., 2009). Castanga et al. (2003) and others provide case studies indicating that the presence of known overlying hydrocarbons gives rise to deeper low-frequency "shadows". For resource plays, if attenuation arises from intercrack flows (i.e. flow though aligned flow conduits between parallel fractures), then attenuation anisotropy may be related to the anisotropy of horizontal permeability (Lynn, 2004a). Lynn (2004b) hypothesized that one can estimate open fractures by measuring the quality (Q) factor (1/attenuation). Gao (2013) showed how the spectral response can change with offset and azimuth for rugose surfaces. Cho et al. (2013) found anomalous spectral response after hydraulic fracturing. In addition, the apparent attenuation caused by the scattering effect was more pronounced when the shear-wave polarization was perpendicular to the crack plane, and the crack aperture had the same magnitude as the source wavelength (de Figueiredo et al., 2011).

Robust attenuation measures from seismic data have great potential for reservoir characterization and direct detection of hydrocarbons, especially natural gas. For example, based on an understanding of the relationship between frequency decay and effective stress, an attenuation-based pore pressure prediction technology reveals the relationships between the geometry of the pore pressure distribution, the structure of the rocks, and the accumulation of hydrocarbons (Young et al., 2004). Studies show that attenuation is frequency selective, with seismic energy loss typically occurring in the high frequency end of the spectrum. Such behavior suggests that signal processing algorithms targeting anomalous high frequency energy may provide accurate attenuation measures.

Conventionally, energy loss per cycle is represented by Q, however, despite different authors having used the identical name, Q value computation in different contexts are not the same (Morozov and Ahmadi, 2015). Several attenuation estimation methods measure the apparent attenuation without classifying its type (Quan and Harris 1997; Zhang and Ulrych 2002). Specific attenuation estimation of a given type implies a specific energy loss mechanism. In their study, O'Doherty and Anstey (1971) concluded that the apparent seismic attenuation includes the intrinsic attenuation, as well as the interaction among multiple receivers, geometric spreading, scattering, frequency-independent transmission loss or gain, and frequency-dependent thin layer interfaces. For reflection seismic data, geometric spreading can be compensated during migration, while thin layer interferences can be corrected using well logs and impedance inversion (Li et al., 2015a). Intrinsic losses due to conversion from mechanical to heat energy, as well as scattering losses due to fracture heterogeneities and rugose surfaces occure in both conventional and unconventional reservoirs. For this reason, the characterization of apparent attenuation can be beneficial for both kinds of reservoirs.

In this chapter, I first discuss the classification of attenuation. Then, I evaluate seven seismic attenuation attributes for reservoir identification: energy reduction of the normalized spectra of high frequencies and full bands, spectral bandwidth, skewness, kurtosis, spectral slopes of both low and high frequencies. (For comparison, I also examine the central frequency shift (CFS) method (Appendix 4.C) to produce an apparent attenuation value). I apply these attenuation measures for a conventional sand reservoir and an unconventional hydraulically-fractured shale reservoir.

Q CLASSIFICATION

As discussed above, despite the same name and similarity, the term *Q* does not have the same meaning in different applications. A classification of the concept of *Q* is a complex task because this concept represents a mixture of measurement techniques, empirical definitions, physical theories, mathematical transformations, and simplified assumptions. Morozov and Ahmadi (2015) categorized the attenuation effects into three types (Figure 4.1). One needs to differentiate these different uses of the *Q* factor: (1) a measure of "internal friction" implied in petrophysical interpretation, (2) apparent *Q* estimates arising from observations, and (3) the "axiomatic," mathematical *Q* used in viscoelastic theory and numerical modeling. These three groups differ in physical meaning, underlying theory, method of measurement, attainable resolution and accuracy, and most importantly, their role in data analysis and interpretation. The measures of seismic attenuation used in different models and obtained from different measurements and inversion approaches are also different.

Seismic attenuation classification is constructed based on the phenomenological aspects. The first type is the "true," or "intrinsic" *Q*. As the first column in Figure 4.1, this *Q* is a property of the phenomenological "imperfect modulus" in seismology and materials science (Anderson and Archambeau 1964; Lakes, 2009), which comprises certain petrophysical properties of the wave-propagating medium. These underlying properties may be broadly variable (for example, granularity, dislocations, fluid content, as well as electric, magnetic, or thermal properties). The true internal-friction mechanisms are usually explained by first-principle physics and generally do not require

the notion of a *Q*. Their relations to *Q* models can be complicated and require further study.

As a common tool of attenuation analysis, the second type, apparent *Q* (second column in Figure 4.1), is the empirical parameter reported from most observations, and has been studied in Chapters 2 and 3. Apparent *Q* may differ for different types of observations (for example, lab or field measurements of direct, refraction, reflection, or surface-wave events), and their relationships to the internal friction may be intricate and variable. For example, the "scattering *Q*" which is particularly important in seismology is difficult to formalize and measure. By the nature of wave-attenuation phenomena and measurements, the apparent *Q* is always averaged and statistical, and therefore its accuracy and resolution in time and frequency are strongly limited (item c in Figure 4.1).

In contrast to the first two types, the axiomatic *Q* is attributed to the material mathematically, through the popular viscoelastic model (Lakes, 2009). The purpose of the measured attenuation is to represent the internal friction (material *Q*), while the numerical approximation is made through the use of the approach such as the relaxation times and strain-stress phase lags. These parameters link the apparent *Q* to the physical internal friction models. Although this model is convenient mathematically, broadly used, and seems intuitively appealing, its rigorous meaning and relation to petrophysical properties of materials is poorly understood. The viscoelastic model also contains a specific, inherent spatial averaging that is difficult to assess in *Q* results.

Several theoretical models explain dissipation of elastic waves in solids, such as poroelasticity (Biot, 1956), squirt pore-fluid flows (Jones, 1986), thermoelasticity, and solid viscosity (Landau and Lifshitz, 1986). These physics-based models belong to the

"internal friction" category. Another theoretical approach to anelastic attenuation is represented by viscoelasticity (Aki and Richards, 2002; Lakes, 2009). Because of its simplicity and generality, this model is broadly used in exploration and observational seismology and lab studies. Modeling local flow, also known as squirt, cannot be done in a similar manner because local flow depends on various parameters describing pore shapes and orientations. Most theoretical models of squirt-flow attenuation are based on the analysis of aspect ratio distributions (Palmer and Traviolia, 1980; Jones, 1986) and pressure relaxation time (Murphy et al., 1986). The observations of internal friction are explained by a specialized parameter (viscoelastic Q) associated with the elastic modulus. Similarly to the modulus, the viscoelastic Q is free from the statistical constraints discussed above, and its images can be arbitrarily detailed. For example, to explain wave attenuation in porous rocks containing heavy oil or melts, viscoelastic moduli and Q are attributed to pore fluids or solids, i.e., to the microscopic level (Mavko, 2013). Nevertheless, the viscoelastic model still does not fully correspond to reality, and its Q should be differentiated from the internal friction and the various apparent Q.

From the above descriptions of the different aspects of Q, most of the existing estimates of Q belong to the apparent Q category and not to the internal friction (i.e., representing a material property) as it may be implied. Moreover, these values are only robust (as "interval" or scattering Q in contrast to the structural Q) when averaged over substantial time and/or spatial intervals. The apparent structural Q contains effects of colored transmission and reflections on layered structures, as well of the underlying theoretical models. A statistical, averaged character is an important characteristic of any

self-consistent type of *Q*, because many apparent *Q* models suggest that the estimates are likely influenced by deterministic local structures (Chapter 3).

In practical seismic data processing and inversion, exact estimates of *Q* are sometimes unimportant. The goal of attenuation analysis may be limited to enhancing the data or aiding the interpretation. By contrast, when numerically modeling seismic wavefields, it is important to ensure that the algorithms adequately represent the physical mechanisms of wave attenuation.

Seismic interpreters commonly are not interested in the absolute attenuation value, but in the relative attenuation effects between an area and its surroundings. Li et al. (2015b) proposed a suite of seismic attenuation attributes that quantify the spectral changes between a shallower reference and a deeper target horizon to detect anomalous spectral energy loss. The sketches in Figure 4.2 summarize these seismic attenuation attributes. Simple mathematical derivations are in Appendix 4.A - Appendix 4.D.

APPLICATIONS

A CONVENTIONAL RESEROIR – RED FORK SANDSTONES

The study area is in the eastern part of the Anadarko Basin, Oklahoma (Figure 4.3). Pennsylvanian rocks throughout most of the Anadarko Basin are dominated by shallow-shelf marine clastics. The target is the Red Fork Sand of the middle Pennsylvanian age, composed of clastic facies deposited in a deep-water (shale/silt) to shallow-water fluvial-dominated environment. The Red Fork Sandstone is sandwiched between the shallower Pink Limestone and the deeper Inola Limestone. The Oswego Limestone that lies above the Pink Limestone and the Novi Limestone that lies below the Inola

Limestone are prominent reflectors that can be mapped easily on seismic-amplitude data, and are used to generate stratal slices that approximate a fixed geologic time. The Upper Red Fork incised-valley system consists of multiple stages of incision and fill, resulting in a stratigraphically complex internal architecture.

Figure 4.4a shows the time structure map of the base of the channels in the Red Fork, where the channels are clearly visible. Figure 4.4b shows a horizon along the Red Fork through inverted seismic impedance, where zones of sandstone deposited in the channels exhibits lower impedance, while other areas and surrounding matrix shows higher impedance. Figure 4.5 shows the vertical seismic section along line AA' (location displayed in Figure 4.4a). Seismic amplitude is displayed in variable area format and overlain by instantaneous envelope in color. The Red Fork channel base is displayed as the yellow solid line. The Redfork channel thickness varies from location to location. In addition, the incise channels and four well locations are also denoted.

In Figure 4.6, I extract the seismic trace at CDP (common depth point) 170 denoted by the red triangle along arbitrary line AA' in Figure 4.5 and analyze its spectrum in a sliding window. I picked three positions on the selected trace and highlight them by red, black and blue rectangles, from Oswego, Pink Lime and Red Fork, respectively. The amplitude spectrum plotted with the red curve corresponds to the wavelet in the red rectangle, while the black and blue amplitude spectra correspond to the wavelets in the black and blue rectangles. I corender all three amplitude spectra in last subfigure of Figure 4.6. Examination of the cartoons in Figure 4.2 suggests that I can apply seismic attenuation attributes to characterize these spectral changes.

Figure 4.7 shows the seismic attenuation attribute values calculated using the central frequency shift (CFS) method (Appendix 4.C) between the top Pink Lime and bottom of the incised Red Fork formation in Figure 4.5. The light blue curve in Figure 4.7a indicates strong attenuation ($1/Q$) at the locations of channels, which implies strong absorption or attenuation in the gas-bearing sandstone. However, I can also find some unphysical (negative attenuation) values on this curve, which is inconsistent with the constant attenuation model. As mentioned previously, the apparent attenuation includes not only intrinsic attenuation, scattering attenuation, but also the spectral interference which I attribute to thin layers and also changes the seismic spectra. Given this shortcoming, I compute the other seven seismic attenuation attributes: energy reduction of high frequencies, energy reduction of full spectral band, spectral bandwidth (Figure 4.7a), skewness, kurtosis, spectral slopes of low frequencies, and spectral slopes of high frequencies (Figure 4.7b). From the appendixes and sketches in Figure 4.2, it is clear that the attributes capture different aspects of spectral changes. Almost all the seismic attenuation attributes have higher values at the channel locations. And, at the original negative attenuation locations, some attributes are showing more reasonable results. Multiple seismic attenuation attributes should be analyzed together to provide better interpretation because a single attribute may be unable to lead to a conclusive result. Interpreters can analyze all the attributes and can decide the best attributes which provide valuable information assisting for interpretation.

Figure 4.8 shows maps of the eight seismic attenuation attributes along the whole Red Fork formation. Note that almost all the attributes highlight the incised channel system, which verifies our hypothesis that sandstone would produce stronger attenuation

than surrounding matrix. Most of the productive wells are also located in the high attenuation areas. Wells, which produced at high initial volumes, correspond to areas of high energy absorption at the producing horizon. It is particularly interesting to note that the spectral bandwidth attribute helps to identify the location of potential hydrocarbon in the stratigraphic trap. First, from the seismic inversion and well locations in Figure 4.4, I can locate the fluvial system, and spectral bandwidth shows the best correspondence. Second, there is an area in the south of the major channel showing low impedance on Figure 4.4b, which should be anomalous. Spectral bandwidth result shows low attenuation.

The Southwest area (higher impedance on Figure 4.4b) exhibits high attenuation, is painted as strong attenuation in Figure 4.8a, 4.8b and 4.8c. According to the interpreted horizons on Figure 4.5, I believe this is because the Red Fork formation is quite thin at certain areas, so the thin-bed effect would introduce spectral interferences, which damages the attribute evaluation.

AN UNCONVENTIONAL RESERVOIR – THE BARNETT SHALE

The Barnett Shale is one of first shale resource plays in the Fort Worth Basin (FWB), Texas (Figure 4.9) Shale acts as the source rock, seal, and trap (Perez, 2009). Completion is often more expensive than drilling the horizontal well. Ideally, operators use image logs, production logs, chemical tracers, and microseismic monitoring to determine the effectiveness of a given completion process. The survey shown in Figure 4.8 was acquired after hydraulic fracturing using about 200 vertical and 200 horizontal wells (Thompson, 2010). Seismic data were acquired for this survey area after the wells

were drilled and hydraulically fractured. In the survey area, the relatively brittle Barnett Shale reservoir falls between the more ductile Marble Falls and Viola Limestones which form the frac barriers (Perez and Marfurt, 2014). A thin Forestburg Limestone which can acts as an imperfect frac barrier separates the reservoir into the Upper Barnett and the Lower Barnett sections. Figure 4.10 shows the seismic data with the interpreted Upper Barnett shale and Lower Barnett Shale, and a time structure of the top Lower Barnett shale.

Figures 4.11 shows the curvature attributes of the Lower Barnett shale. Curvature maps paleo deformation in this survey. Because the fracture scale is below the seismic resolution, curvature does not "see" any small scale fractures. Curvature measures strain, which is a component of natural fracture formation and thus zones of weakness and/or strength for subsequent stimulation. In this survey, the ridges form fracture barriers with most microseismic events occurring within structural bowls (Perez and Marfurt, 2014). Production appears to be compartmentalized by these ridges.

Cho et al. (2013) evaluated a Canadian shale resource play using a careful time-lapse seismic survey, I note strong spikes in the spectra which they attributed to the addition of discrete gas-filled fractures. For an unconventional survey, such scattering attenuation would contribute to the apparent attenuation effect. I applied CFS method to estimate apparent attenuation values, shown in Figure 4.12a. Apparent attenuation has high correlation with curvature attributes in Figure 4.10. Horizontal well paths are also shown on Figure 4.12. The locations of productive wells should display high attenuation. But in some areas where the well density is high, the attenuation attribute shows low values. In addition, note that there is "negative" attenuation shown in blue. Such

attenuation would be unphysical for the classic constant *Q* model. However, the "attenuation" mapped here is due to increased scattering due to new, gas filled fractures. Figures 4.12b to 4.12h display the remaining seven seismic attenuation attributes.

Verma et al. (2012) evaluated TOC (Total Organic Carbon) based on the low density, low velocity with Neural network method, shown in Figure 4.13a. Using a similar approach, I obtain the BI (brittleness index) map in Figure 4.13b, which indicates the brittleness, one of the most important factors for hydraulic fracturing. And, high and low production areas from Thompson (2010) are denoted on Figure 4.13. TOC indicates the organic material accumulation. Shales have very low permeability, and the hydrocarbons do not migrate, but it can migrate through fractures, or it can also stay in fractures. Hydrocarbon saturated fractures would show high TOC, but not only gas/oil accumulation can show high TOC, other nonproducible hydrocarbon can also show high TOC. In addition, layers with high TOC could be ductile, which can hinder hydraulic fracturing. Thus, unconventional reservoir evaluation requires considering both the TOC and BI.

From Figures 4.12 and 4.13, I observe that there is no directly decisive relationship among production, TOC and BI. For example, the south end of the survey shows low BI and low production, but high TOC, while there are many horizontal wells in that area. High TOC doesn't ensure high production for horizontal wells, because, first, high TOC doesn't equal gas/oil reservoir; second, low brittleness is bad for hydraulic fracturing, so this area has a low production. Another example is the northern high BI area in Figure 4.13b. Since the seismic data is acquired after hydraulic fracturing, the high BI indicates high density fracture. Fracture system can produce scattering attenuation.

Thus, in the attenuation attributes in Figure 4.12, the northeast part of the survey usually shows high attenuation.

Figure 4.14 displays two vertical sections of seismic impedance at different locations shown on well location map. For BB', most of the attributes in Figure 4.12 show high attenuation values, and the impedance section shows two major internal layers. For CC', most attributes show low attenuation (negative value), and the impedance profile shows layering effect. Li et al. (2015a) showed thin beds can alter the seismic spectrum, which results in unreliable attenuation estimation. Considering the influences of TOC, BI and thin-bed tuning effect, the attenuation characterization is very complex. In actual drilling and production, there are still some more factors, which should be taken into account, e.g. stress/strain field. Spectral slope of high frequencies is the only seismic attenuation attribute, which highlights both the high TOC and high BI areas.

DISCUSSION

Barnes (2007) warned that after many years of attribute development many attributes are redundant, and some are even useless. I have evaluated a suite of attenuation attributes, all of which are based on input spectral decomposition volumes. For the conventional porous gas reservoir analyzed, the classic *Q* model computed using the CFS algorithm provides a good discrimination between the presence and absence of gas. In contrast, the assumptions of the classic *Q* model are radically violated as a model for induced, gas-filled fractures of the Barnett Shale. For this situation, *Q* becomes an attribute, and is no longer a rock property. However, correlation with production and

microseismic measures of fractured rock indicates that it may become an important tool in estimating reservoir completion.

The proposed seismic attenuation attribute suite is not a gas indicator *per se*, nor does it deliver a quantitative Q value. Rather, the process detects local areas where high frequency energy has been rapidly lost over a target horizon, and as such should be thought of as a qualitative way of detecting intervals of anomalous energy attenuation in the subsurface. Because numerous petrophysical mechanism causes give rise to energy attenuation, the presence of gas is only one of the several possible mechanisms considered by the interpreter. Nevertheless, I have seen numerous data sets in which absorption anomalies were coincident with gas reservoirs, and in many cases, the absorption attribute identifies the gas reservoirs where other seismic attributes (e.g., amplitude, AVO) do not (Mitchell et al., 1996). I are thus encouraged to pursue seismic attenuation as a reservoir characterization attribute.

Words of caution are appropriate. While attenuation attributes can measure high frequency energy loss in the data caused by presence of gas and fractures, it can also measure non-geological factors. Possible non-geological seismic attenuation pitfalls include seismic acquisition (the data need to have an adequate frequency range to target the loss of high frequency energy), as well as data contamination of data in seismic processing (AGC, spectral whitening, deconvolution, stacking and other processes can alter frequency content). For these reasons, I recommend true amplitude processing common to AVO and prestack inversion analysis.

CONCLUSIONS

After describing a suite of seismic attenuation attributes, I apply them to the field data to detect hydrocarbon and evaluate fracture system. Almost all of the attributes have good correspondences with production. Thus they are useful and promising for seismic interpretation as well as reservoir characterization. However, because different attributes measures different spectral changes, they demonstrate different aspects of seismic apparent attenuation. According to the application situations, I should adopt suitable attributes. In future, multiattribute clusters and statistical analysis tools will be really helpful for choosing the most appropriate attribute or producing the combination of seismic attributes.

APPENDIX

4.A Apparent Attenuation on Seismic Spectrum

When a seismic wave propagates in a viscoelastic medium in a constant linear frequency attenuation model, the apparent *Q* arises by considering a traveling wave whose spectral amplitude exponentially reduces with traveltime as (Aki and Richards, 2002)

$$A(\omega,\tau)=S(\omega)\exp\left(-\frac{\omega\tau}{2Q}\right), \tag{4.A-1}$$

where, $\omega=2\pi f$ is the angular frequency, $S(\omega)$ is the source wavelet spectrum, τ is the travel time, and $A(\omega,\tau)$ is the received signal spectrum including all geometric spreading, source, and receiver effects.

Here, it clearly shows that the apparent *Q* is not related to certain specific rock properties. It is just a symbol for apparent attenuation in frequency domain. Hence, adopting seismic attributes to characterize this effect is not inapproriate.

4.B The Ricker Wavelet and Its Frequencies

I assume the seismic signal is propagating as a Ricker wavelet, which is suitable for empirical situations. Wang (2015) discussed frequencies of the Ricker wavelet, which inspired some of the following derivations.

The Fourier transform of the Ricker wavelet can be expressed as

$$R(\omega)=\frac{2\omega^2}{\sqrt{\pi}\omega_m^3}\exp\left(-\frac{\omega^2}{\omega_m^2}\right), \tag{4.B-1}$$

where ω is the angular frequency and ω_m is the dominant frequency (the most energetic frequency, also in radians per second). This is an amplitude spectrum, so it is real and nonnegative.

I can set the derivative of the amplitude spectrum $R(\omega)$ to zero to get the corresponding peak frequency ω_p:

$$\frac{\partial R(\omega)}{\partial \omega} = \frac{4\omega}{\sqrt{\pi}\omega_m^3}\left(1-\frac{\omega^2}{\omega_m^2}\right)\exp\left(-\frac{\omega^2}{\omega_m^2}\right) = 0 . \tag{4.B-2}$$

This leads to $\omega_p = \omega_m$.

Replacing the $S(\omega)$ in Equation 4.A-1 by $R(\omega)$ in Equation 4.B-1, I can obtain the attenuated seismic spectral expression. Then I adopt the way in Equation 4.B-2 to calculate the peak frequency after attenuation:

$$\frac{\partial\left[R(\omega)\exp\left(-\frac{\omega\tau}{2Q}\right)\right]}{\partial\omega} = \frac{\partial R(\omega)}{\partial\omega}\exp\left(-\frac{\omega\tau}{2Q}\right) - R(\omega)\frac{\tau}{2Q}\exp\left(-\frac{\omega\tau}{2Q}\right) = 0 . \tag{4.B-3}$$

This leads to

$$\tilde{\omega}_p = \frac{{\omega_m}^2}{2}\left(\sqrt{\frac{\tau^2}{4Q^2}+\frac{4}{{\omega_m}^2}}-\frac{\tau}{4Q}\right). \tag{4.B-4}$$

Note that when attenuation is stronger (Q^{-1} is larger), the peak frequency value is smaller.

By substituting the $\omega_p = \omega_m$ to Equation 4.B-1, one can obtain the peak of the Ricker wavelet amplitude spectrum is

$$R(\omega_p) = \frac{2}{e\sqrt{\pi}\omega_m} . \tag{4.B-5}$$

In the following work, I adopt the normalized Ricker wavelet amplitude spectra. It is obtained by dividing the spectra with its maximum value to unity. Hermana et al. (2013) also adopted this normalization approach in attenuation based hydrocarbon prediction, because the spectral amplitude deceases significantly after attenuation which changes the spectral shape properties without appropriate conditioning.

The normalized Ricker wavelet amplitude spectrum is formulated as:

$$\bar{R}(\omega)=\frac{R(\omega)}{R(\omega_p)}=\frac{\frac{2\omega^2}{\sqrt{\pi}\omega_m^3}\exp\left(-\frac{\omega^2}{\omega_m^2}\right)}{\frac{2}{e\sqrt{\pi}\omega_m}}=\frac{\omega^2}{\omega_m^2}\exp\left(1-\frac{\omega^2}{\omega_m^2}\right). \quad (4.B\text{-}6)$$

4.C Attenuation Estimation Methods

Spectral Ratio (SR) Method

For the reference seismic signal A_0 and the attenuated seismic signal A_1, based on Equation 4.A-1, the Spectral Ratio (SR) method can be represented as,

$$\ln\left(\frac{|A_1(f)|}{|A_0(f)|}\right)=-\pi ft/Q. \quad (4.C\text{-}1)$$

An estimate of *Q* can be derived by curve fitting within the common effective bandwidth of the two spectra using the least-squares method. An effective bandwidth should be chosen to avoid high frequency fluctuation caused by additive noise or numerical errors brought by finite precision.

Central Frequency Shift (CFS) Method

Quan and Harris (1997) proposed the Central Frequency Shift (CFS) method by correlating *Q* with the changes in the centroid frequency of the seismic signal. The

centroid frequencies of reference and attenuated seismic signals are denoted by f_{c_0} and f_{c_1}, assuming that $|A(f)|$ is of Gaussian shape, Q can be quantified by,

$$Q = \frac{\pi t \sigma_{A_0}^2}{f_{c_0} - f_{c_1}}, \tag{4.C-2}$$

where $\sigma_{A_0}^2$ is the spectrum variance of A_0, defined by,

$$\sigma_{A_0}^2 = \frac{\int_0^\infty (f - f_{c_0})^2 |A_0(f)| df}{\int_0^\infty |A_0(f)| df}. \tag{4.C-3}$$

As an alternate Q estimation method of SR methods, CFS method is a milestone for frequency shift methods. It is quite robust as the estimation of centroid frequency is not as sensitive as SR method to noise. However, I notice that the preconditions of CFS method are the Gaussian shape of the seismic spectrum and the unchanged spectrum variance. However, the seismic spectrum is usually a non-Gaussian distribution and the attenuation effect would certainly change the spectrum variance, which brings inaccuracies to this method.

4.D Seismic Attenuation Attributes

My objective is to propose attributes to measure the spectral changes caused by attenuation. I assume the decrease in peak frequency is the main change, and after attenuation the seismic spectrum is still a Ricker wavelet spectrum. Set the reference spectrum without attenuation to $R_0(\omega)$ with peak frequency ω_{m0}. The received attenuated spectrum is $R_1(\omega)$ with peak frequency ω_{m1}. According to Equation 4.B-4, ω_{m1}

should be smaller than ω_{m0}, and the difference between reference and received peak frequencies shows the attenuation strength: larger difference, stronger attenuation.

Higher-order Statistics

As is known, the amplitude spectrum of the Ricker wavelet is the Gaussian distribution multiplied by a factor ω^{-2}, and thus is asymmetric and "unGaussian" in the frequency domain. In mathematics, I would usually use Higher-order Statistics (HOS) to quantify the shape (McGrew and Monroe, 2009). Here, I use skewness (third order moment) and kurtosis (fourth order moment) to measure the spectra's shapes:

$$skewness = \frac{\mu_3}{\sigma^3} = \frac{\mu_3}{\left(\sigma^2\right)^{\frac{3}{2}}} = \frac{\int_0^\infty \left(\omega-\omega_m\right)^3 \frac{\omega^2}{\omega_m^2}\exp\left(1-\frac{\omega^2}{\omega_m^2}\right)d\omega}{\left(\int_0^\infty \left(\omega-\omega_m\right)^2 \frac{\omega^2}{\omega_m^2}\exp\left(1-\frac{\omega^2}{\omega_m^2}\right)d\omega\right)^{\frac{3}{2}}}. \tag{4.D-1}$$

$$= \frac{\frac{1}{8}e\cdot{\omega_m}^4\cdot\left(20-11\sqrt{\pi}\right)}{\left[\frac{1}{8}e\cdot{\omega_m}^3\cdot\left(-8+5\sqrt{\pi}\right)\right]^{\frac{3}{2}}} \approx \frac{1.0777}{\sqrt{\omega_m}}$$

$$kurtosis = \frac{\mu_4}{\sigma^4} = \frac{\mu_4}{\left(\sigma^2\right)^2} = \frac{\int_0^\infty \left(\omega-\omega_m\right)^4 \frac{\omega^2}{\omega_m^2}\exp\left(1-\frac{\omega^2}{\omega_m^2}\right)d\omega}{\left(\int_0^\infty \left(\omega-\omega_m\right)^2 \frac{\omega^2}{\omega_m^2}\exp\left(1-\frac{\omega^2}{\omega_m^2}\right)d\omega\right)^2}. \tag{4.D-2}$$

$$= \frac{\frac{1}{16}e\cdot{\omega_m}^5\cdot\left(-96+55\sqrt{\pi}\right)}{\left[\frac{1}{8}e\cdot{\omega_m}^3\cdot\left(-8+5\sqrt{\pi}\right)\right]^2} \approx \frac{2.9390}{\omega_m}$$

Note the lower peak frequency, the larger skewness, and larger kurtosis. So, I can measure their changes to estimate the relative attenuation.

Spectral Bandwidth

The frequency bandwidth is defined by the frequency components spreading at some proportion of the spectrum peak (maximum value). Here, I set the frequency band to be measured at $\alpha(\alpha<1)$ of the peak, which is 1 in the normalized spectrum, so I get:

$$\bar{R}(\omega)=\frac{\omega^2}{\omega_m^2}\exp\left(1-\frac{\omega^2}{\omega_m^2}\right)=\alpha, \tag{4.D-3}$$

which leads to the inverse exponential equation

$$-\frac{\omega^2}{\omega_m^2}\exp\left(-\frac{\omega^2}{\omega_m^2}\right)=-\frac{\alpha}{e}, \tag{4.D-4}$$

with an analytical solution expressed in terms of the Lambert W function:

$$-\frac{\omega^2}{\omega_m^2}=\mathrm{W}\left(-\frac{\alpha}{e}\right). \tag{4.D-5}$$

The solution of an inverse exponential equation $z\exp(z)=x$ is $z=\mathrm{W}(x)$, where W(x) is the Lambert W function, displayed in Figure 4.D1. Then the frequency band $[\omega_{low},\omega_{high}]$ is given by

$$\begin{aligned}\omega_{low}&=\omega_m\sqrt{-\mathrm{W}_0\left(-\frac{\alpha}{e}\right)},\\ \omega_{high}&=\omega_m\sqrt{-\mathrm{W}_{-1}\left(-\frac{\alpha}{e}\right)}.\end{aligned} \tag{4.D-6}$$

The spectral bandwidth is

$$\omega_b=\omega_m\left(\sqrt{-\mathrm{W}_{-1}\left(-\frac{\alpha}{e}\right)}-\sqrt{-\mathrm{W}_0\left(-\frac{\alpha}{e}\right)}\right). \tag{4.D-7}$$

The variable α is fixed in each situation, so the bandwidth in frequency domain is only related to the peak frequency. Thus, after attenuation, the peak frequency will be lower, and the spectral bandwidth will be narrower.

Spectral Slopes

I compute the expressions of spectral slope averages of low frequencies (from $\beta\omega_m$ to ω_m , $\beta < 1$) and high frequencies (from ω_m to $\sigma\omega_m$, $\sigma > 1$), respectively.

$$Slope_{low} = \frac{\int_{\beta\omega_m}^{\omega_m} \frac{\partial \bar{R}(\omega)}{\partial \omega} d\omega}{(1-\beta)\omega_m} = \frac{\bar{R}(\omega_m) - \bar{R}(\beta\omega_m)}{(1-\beta)\omega_m} \quad . \quad (4.D\text{-}8)$$
$$= \frac{\frac{\omega_m^2}{\omega_m^2}\exp\left(1-\frac{\omega_m^2}{\omega_m^2}\right) - \frac{\beta^2\omega_m^2}{\omega_m^2}\exp\left(1-\frac{\beta^2\omega_m^2}{\omega_m^2}\right)}{(1-\beta)\omega_m} = \frac{1-\beta^2\exp\left(1-\beta^2\right)}{(1-\beta)\omega_m}$$

$$Slope_{high} = \frac{\int_{\omega_m}^{\sigma\omega_m} \frac{\partial \bar{R}(\omega)}{\partial \omega} d\omega}{(\sigma-1)\omega_m} = \frac{\bar{R}(\sigma\omega_m) - \bar{R}(\omega_m)}{(\sigma-1)\omega_m} \quad . \quad (4.D\text{-}9)$$
$$= \frac{\frac{\sigma^2\omega_m^2}{\omega_m^2}\exp\left(1-\frac{\sigma^2\omega_m^2}{\omega_m^2}\right) - \frac{\omega_m^2}{\omega_m^2}\exp\left(1-\frac{\omega_m^2}{\omega_m^2}\right)}{(\sigma-1)\omega_m} = -\frac{1-\sigma^2\exp\left(1-\sigma^2\right)}{(\sigma-1)\omega_m}$$

Both of the slopes have a format of Lambert function in Figure 4.11, so I can estimate their values. The peak frequency and low frequency slope have an inverse relationship. A decrease in peak frequency will indicate an increase in low frequency slope. The low frequency slope is always positive and the high frequency slopes is always negative. The decrease in peak frequency causes the high frequency slope to become more negative but with a larger absolute value.

Energy Reduction

Let's compute the energy difference between normalized reference and received spectra on the whole band, from 0 to infinity:

$$ER_{all} = \int_0^\infty \left[\frac{\omega^2}{\omega_{m0}^2}\exp\left(1-\frac{\omega^2}{\omega_{m0}^2}\right) - \frac{\omega^2}{\omega_{m1}^2}\exp\left(1-\frac{\omega^2}{\omega_{m1}^2}\right)\right] d\omega \quad . \quad (4.D\text{-}10)$$
$$= \frac{1}{4} e\sqrt{\pi}\left(\omega_{m0} - \omega_{m1}\right)$$

This formula shows that spectral energy will decay after attenuation even they are both normalized, and the stronger attenuation, the larger energy reduction.

$$ER_{high} = \int_{\omega_c}^{\infty} \left[R_0(\omega) - R_1(\omega) \right] d\omega . \qquad (4.D\text{-}11)$$

Actually, in Equation 4.18 I can also just compare the spectral energies of higher frequency components, (e.g. Mitchell et al. (1996) proposed a similar energy absorption analysis (EAA) attribute.), starting from their crossover frequency ω_c . As ω_{ml} is smaller, ω_c is smaller, and the differences at frequencies larger than previous ω_c will be larger, so the energy in higher frequencies will reduce more, when the attenuation is stronger.

CHAPTER 4 FIGURES

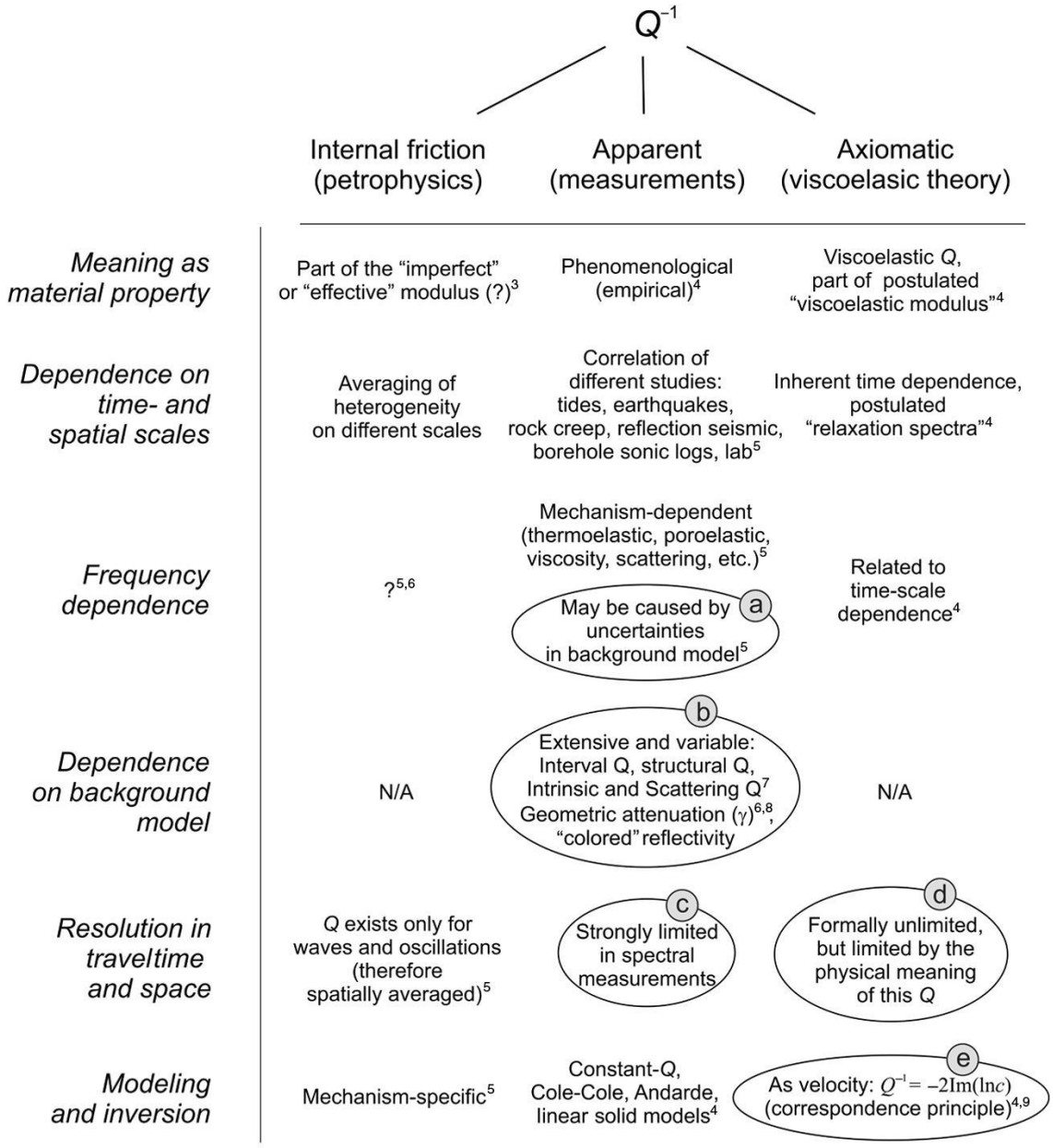

Figure 4.1. The taxonomy of attenuation (Q^{-1}) from Morozov and Ahmadi (2015). The columns are the three general attenuation types, and the rows (labeled on the left) are the aspects by which these types are differentiated. The footnotes refer to selected (incomplete) literature.

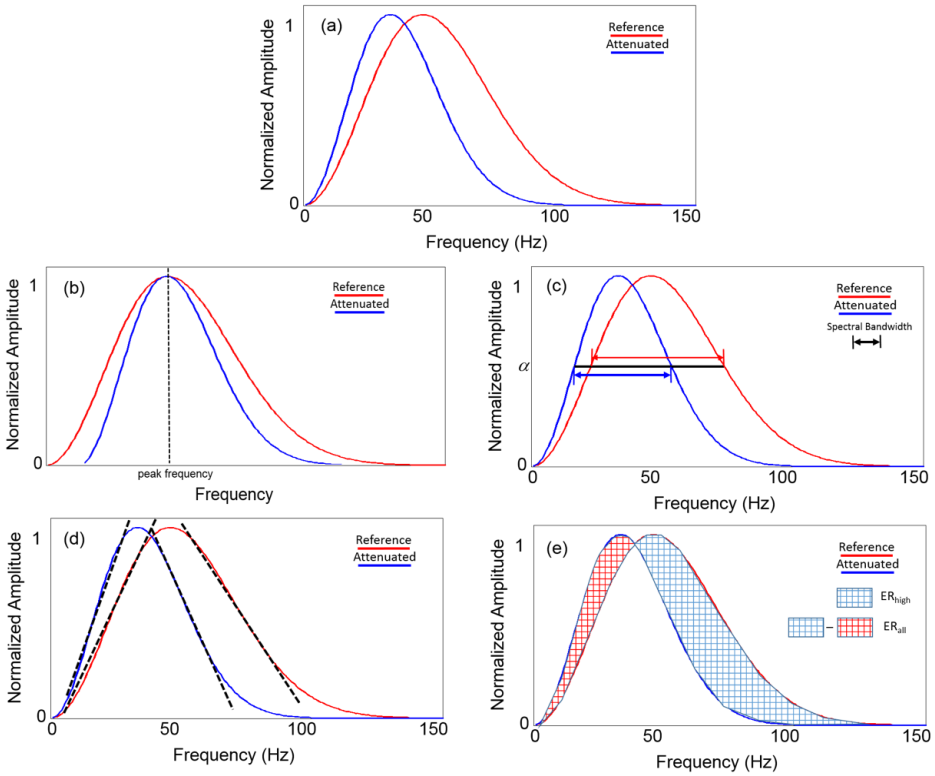

Figure 4.2. Schematics of the proposed seismic attenuation attributes: (a) normalized reference and attenuated spectra, (b) skewness and kurtosis, overlaying their peak frequency axes, (c) spectral bandwidth, (d) spectral slopes at low and high frequencies and (e) energy reduction in high frequencies and all frequency band.

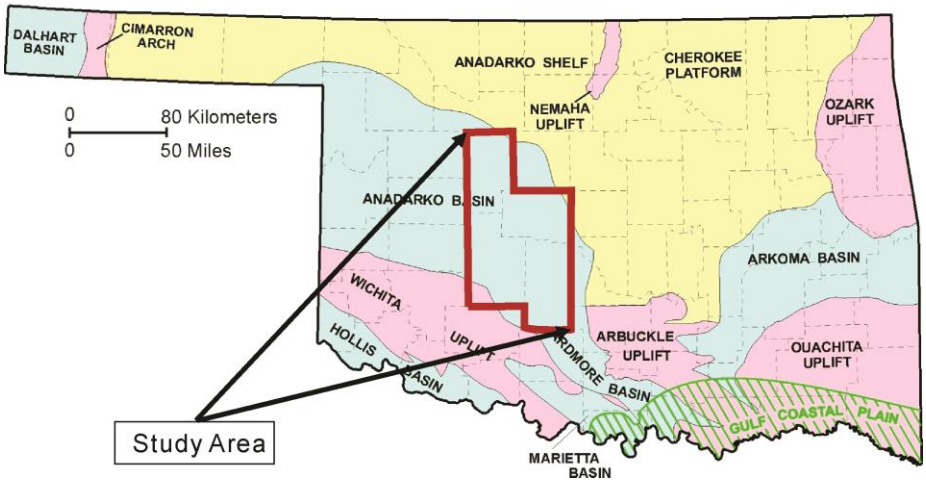

Figure 4.3. Location map of the Anadarko Basin area on a map of Oklahoma. The study area lies inside the red boundary. (After Del Moro et al., 2013).

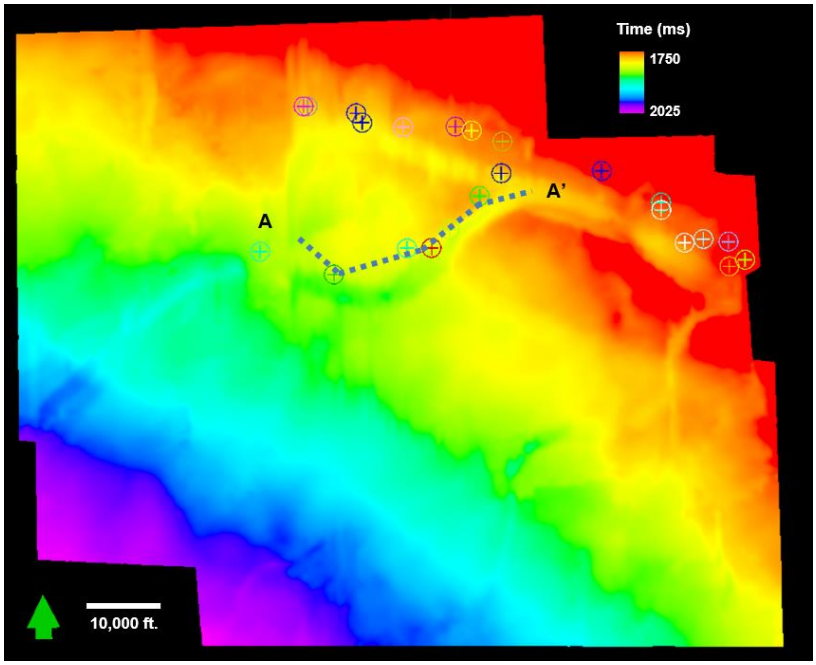

Figure 4.4a

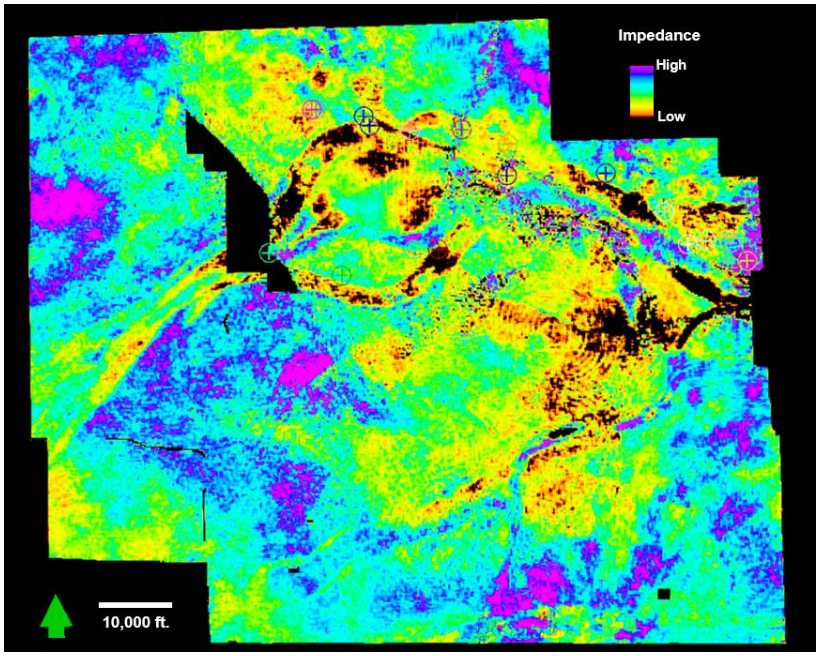

Figure 4.4b

Figure 4.4. (a) Time structure map of the base of the incised channels in the Red Fork channels showing dip to the SW. (b) Horizon slice along base of Red Fork through seismic impedance. Note that the sandstone in the channel shows low impedance in yellow, red and black, while the surrounding matrix shows higher impedance in green, blue, and magenta. The cross circles denote the positions of 19 productive wells.

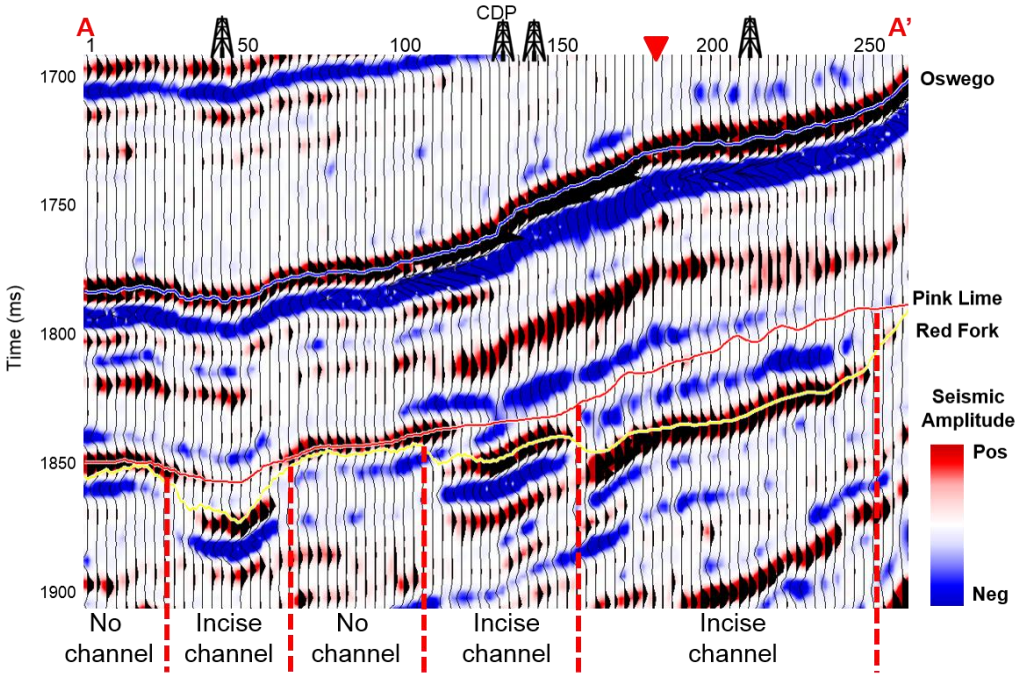

Figure 4.5a

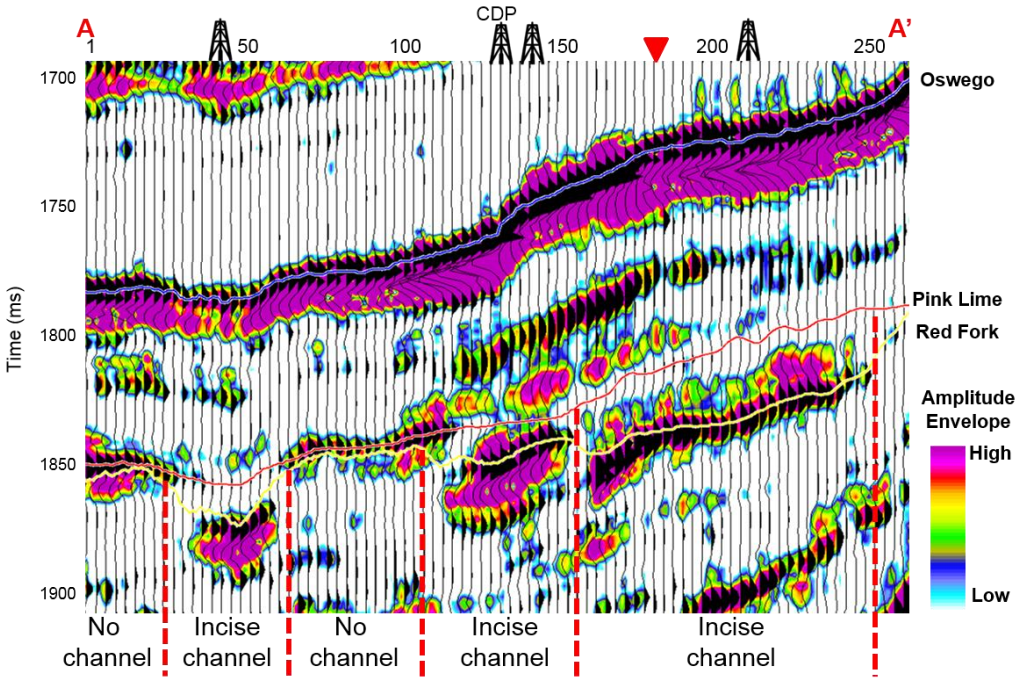

Figure 4.5b

Figure 4.5. Vertical slice along line AA' shown in Figure 4.4a through amplitude overlain by the seismic amplitude (Figure 4.5a) and instantaneous envelope (Figure 4.5b). The Oswego Lime (blue pick) and Pink Lime (red pick) form regional markers. Because of incisement, the amplitude and phase of Red Fork (yellow pick) change across the survey.

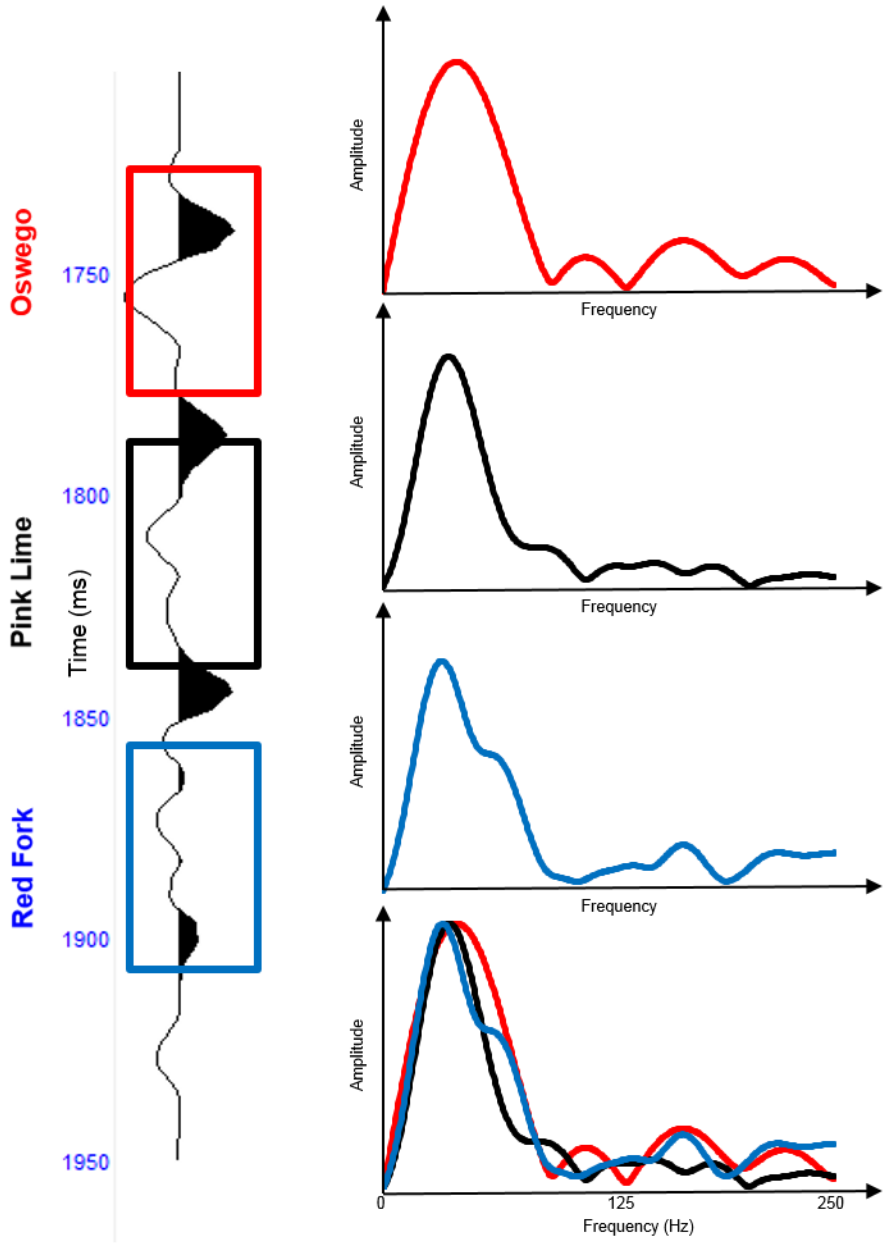

Figure 4.6. Single trace example (extracted from CDP 170, denoted as a red triangle in Figure 4.5) of seismic spectral changes with increasing depth.

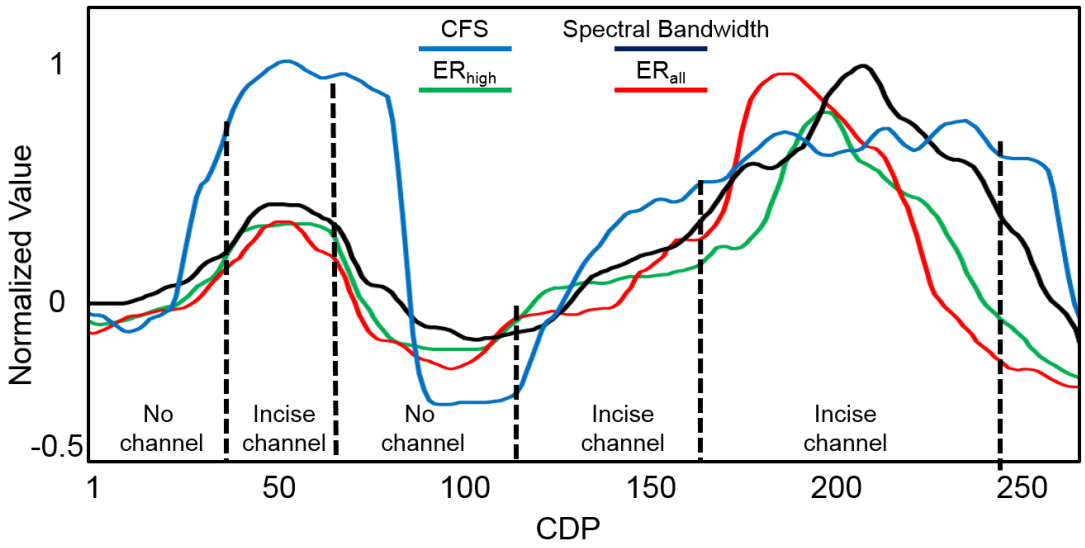

Figure 4.7a

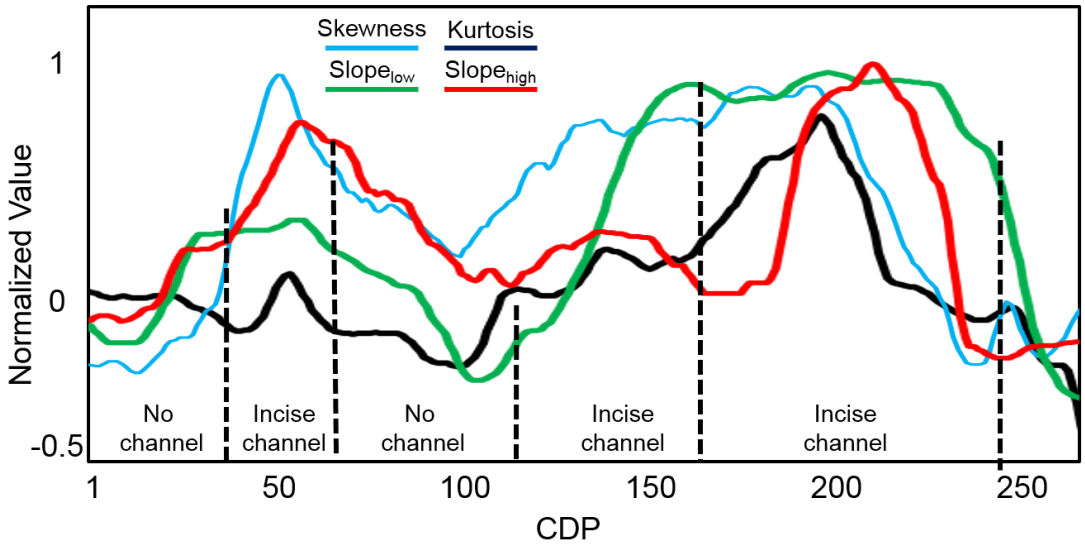

Figure 4.7b

Figure 4.7. Seismic attenuation attributes between the pink and yellow horizon shown in Figure 4.5. (a) Attenuation estimation using the central frequency shift (CFS) method, spectral bandwidth, energy reduction in full bands and high frequency bands, (b) Spectral slopes of low and high frequencies, skewness and kurtosis.

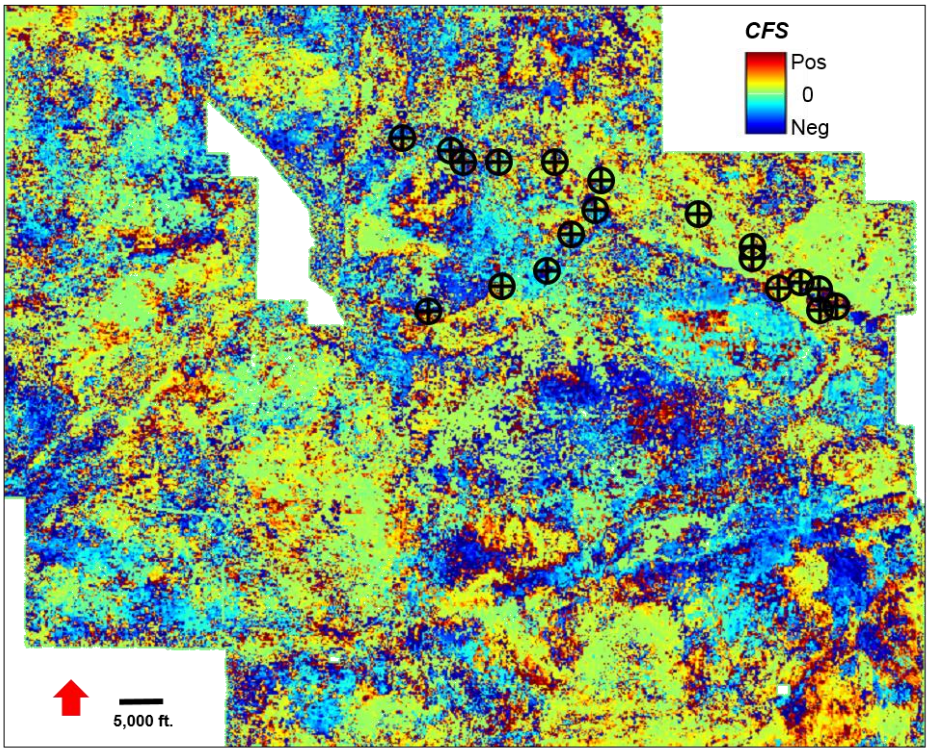

Figure 4.8a

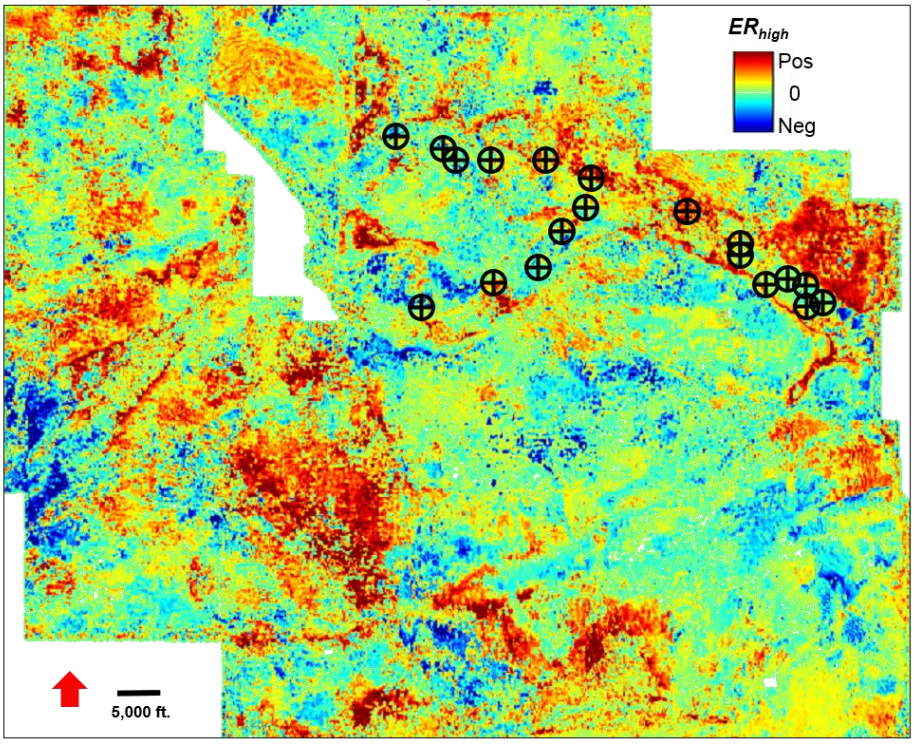

Figure 4.8b

Figure 4.8. Seismic attenuation attributes of the Red Fork formation using: (a) CFS, (b) energy reduction of high frequencies, (c) energy reduction of full spectral bands, (d) skewness, (e) kurtosis, (f) spectral bandwidth, (g) spectral slope of low frequencies and (h) spectral slope of high frequencies. Cross circles denote positions of productive wells.

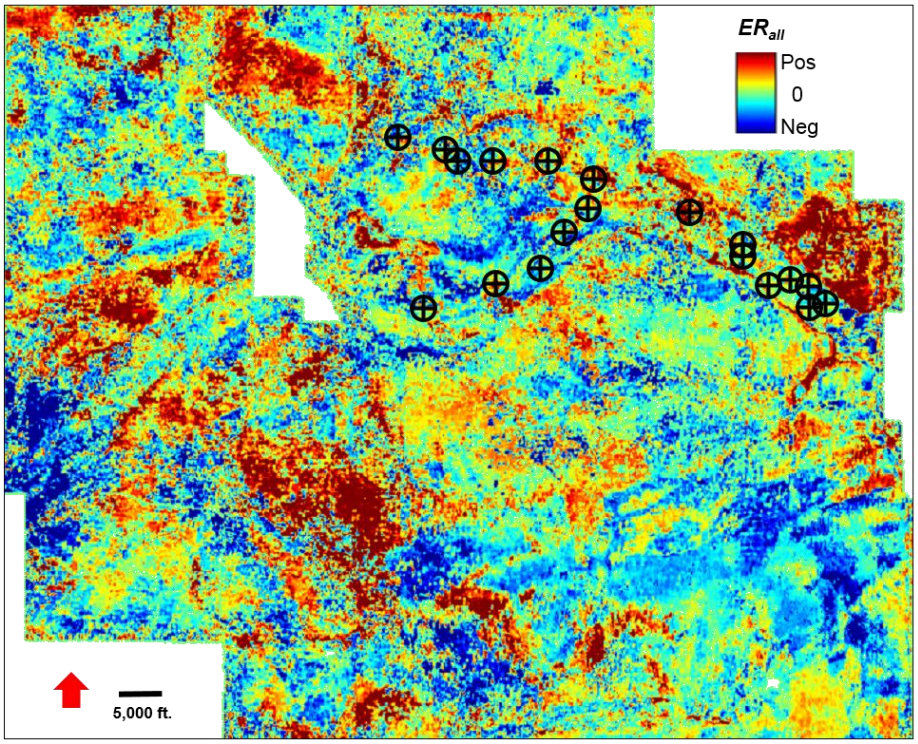

Figure 4.8c

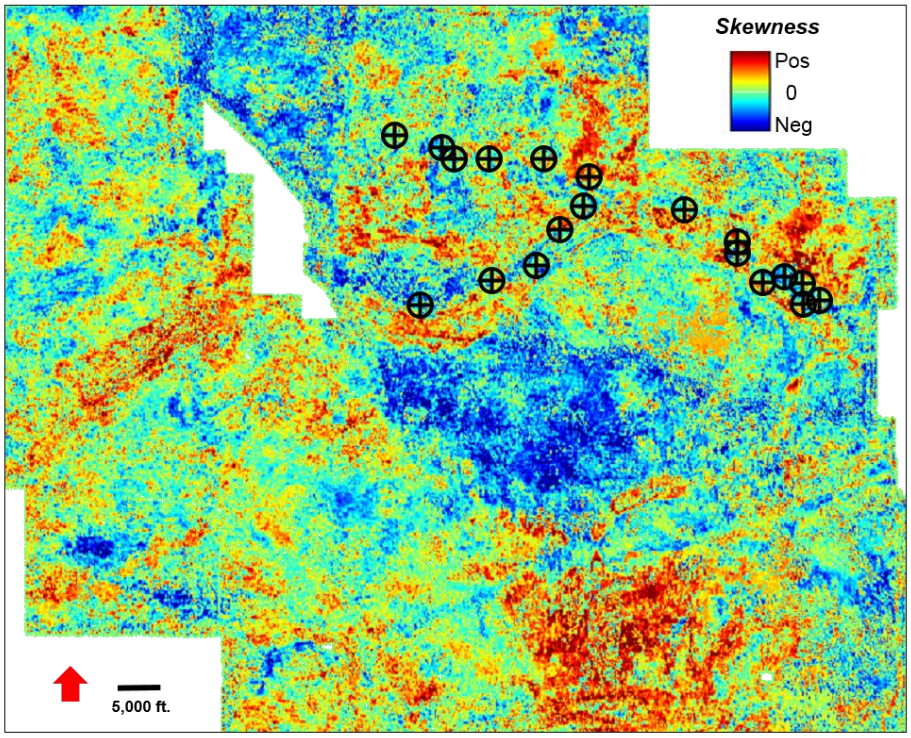

Figure 4.8d

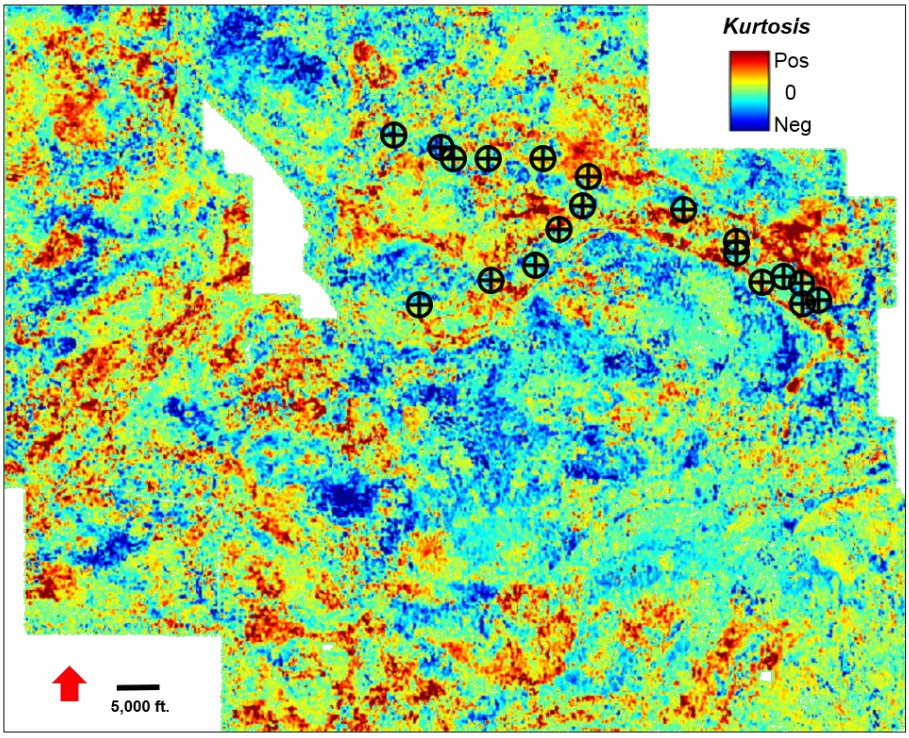

Figure 4.8e

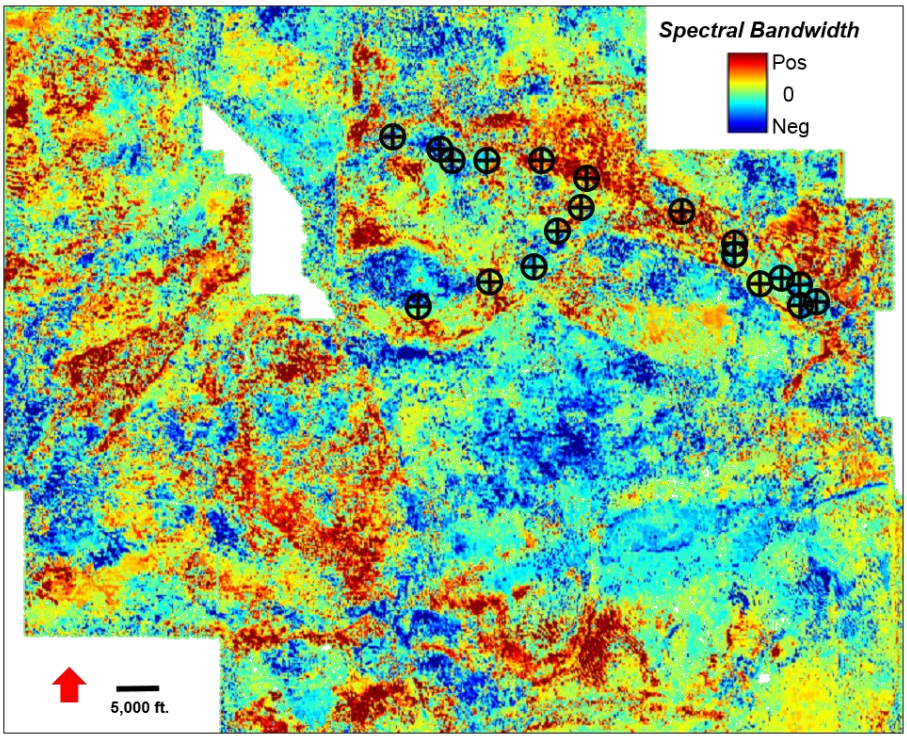

Figure 4.8f

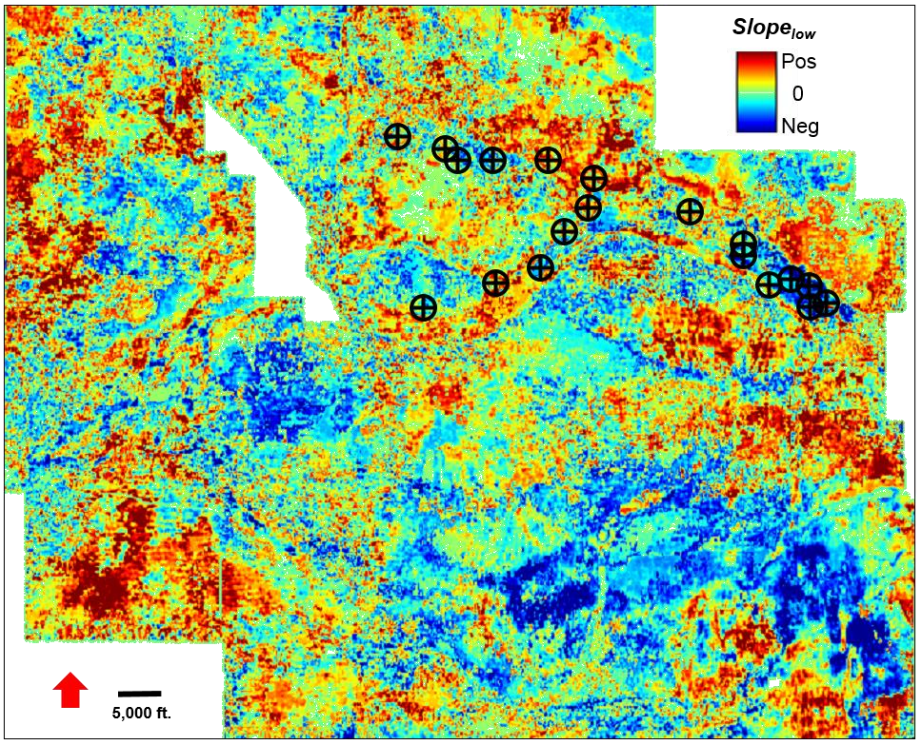

Figure 4.8g

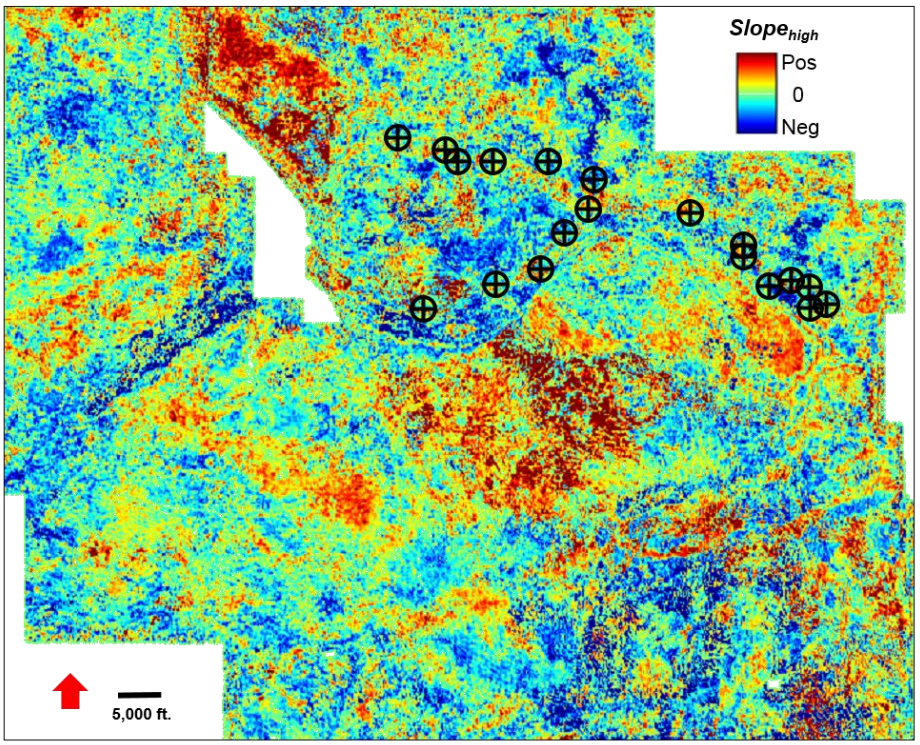

Figure 4.8h

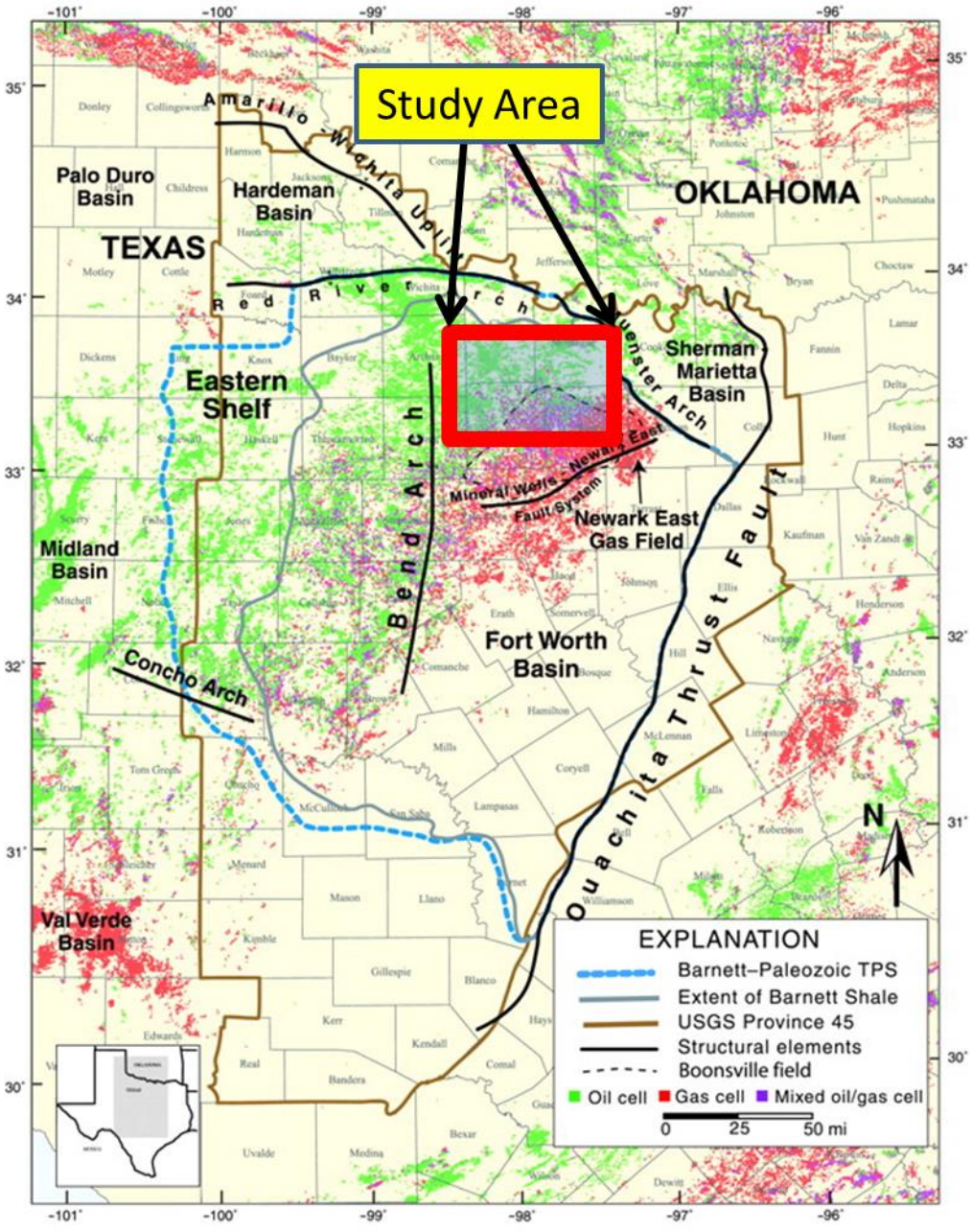

Figure 4.9. Location map of the Fort Worth Basin. The study area lies inside the red boundary. (After Pollastro et al., 2007).

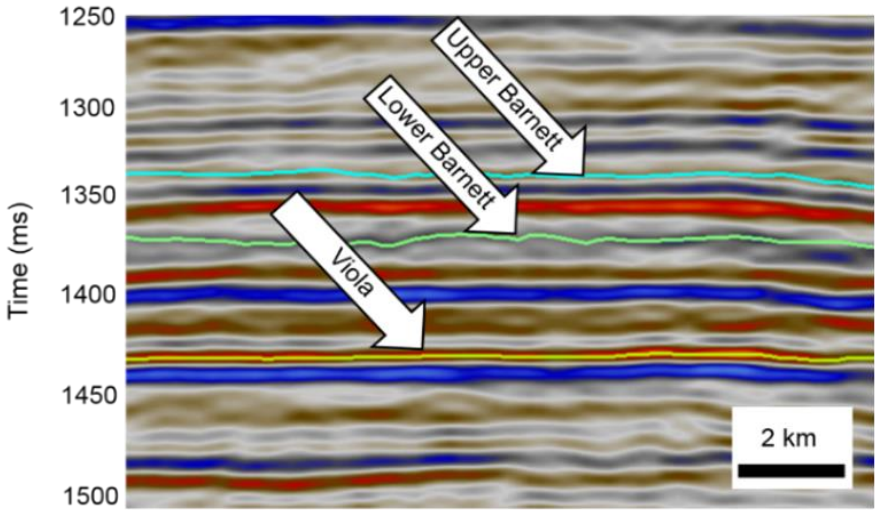

Figure 4.10a

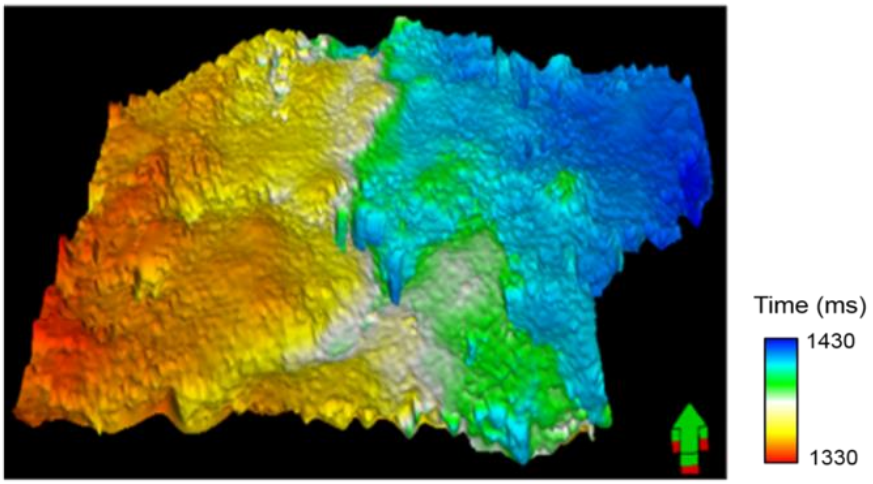

Figure 4.10b

Figure 4.10. (a) Vertical slice through seismic amplitude and interpreted horizons. (b) Time structure map of Lower Barnett Shale.

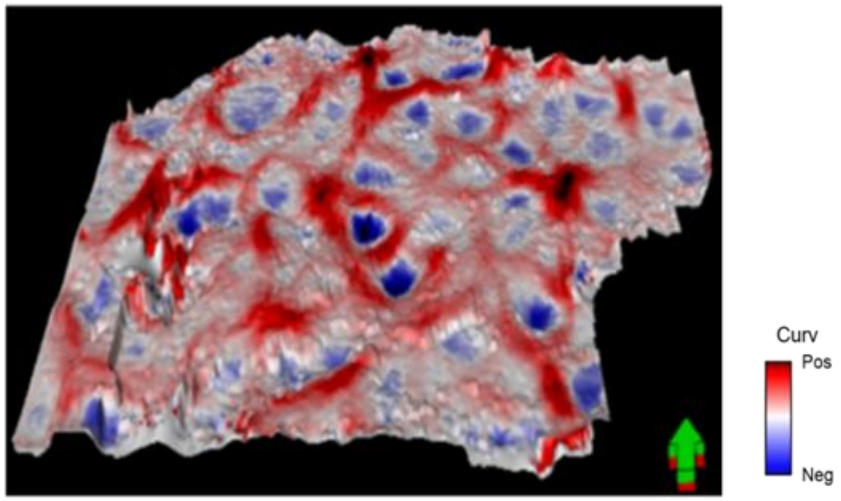

Figure 4.11a

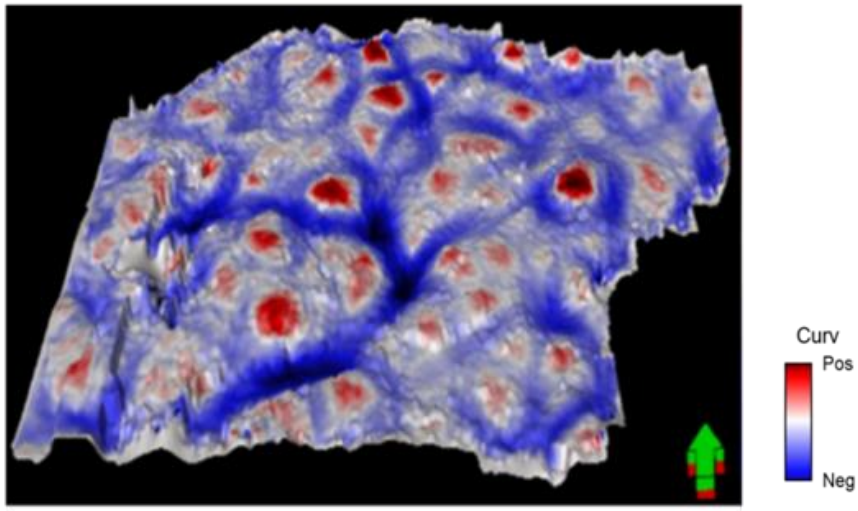

Figure 4.11b

Figure 4.11. Horizon slices along the top Lower Barnett Shale through (a) most positive and (b) most negative curvature volumes.

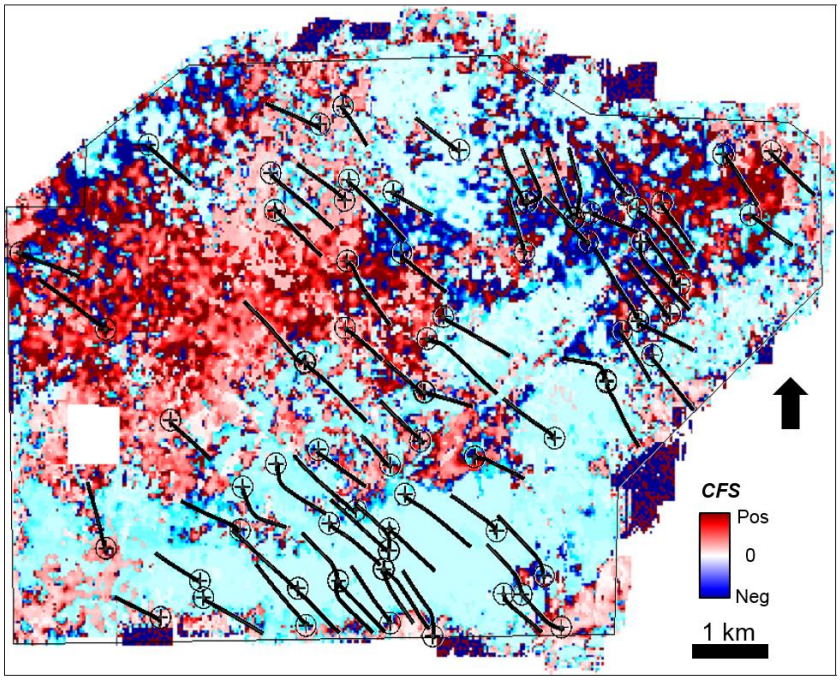

Figure 4.12a

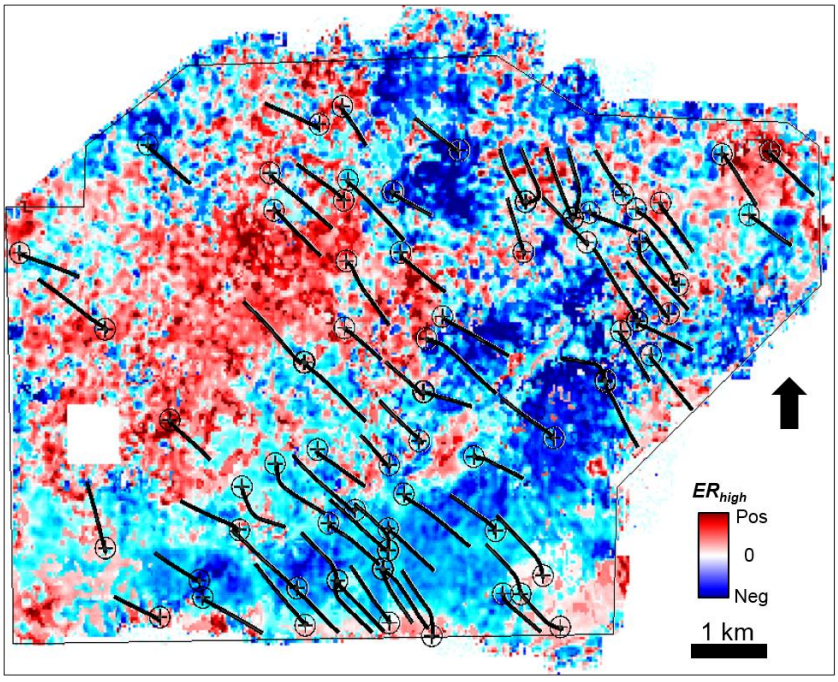

Figure 4.12b

Figure 4.12. Seismic attenuation attributes of the Lower Barnett shale using (a) CFS, (b) energy reduction on the high frequencies, (c) energy reduction on the full spectral bands, (d) skewness, (e) kurtosis, (f) spectral bandwidth, (g) spectral slope of low frequencies, and (h) spectral slopes of high frequencies. Horizontal well paths are also denoted.

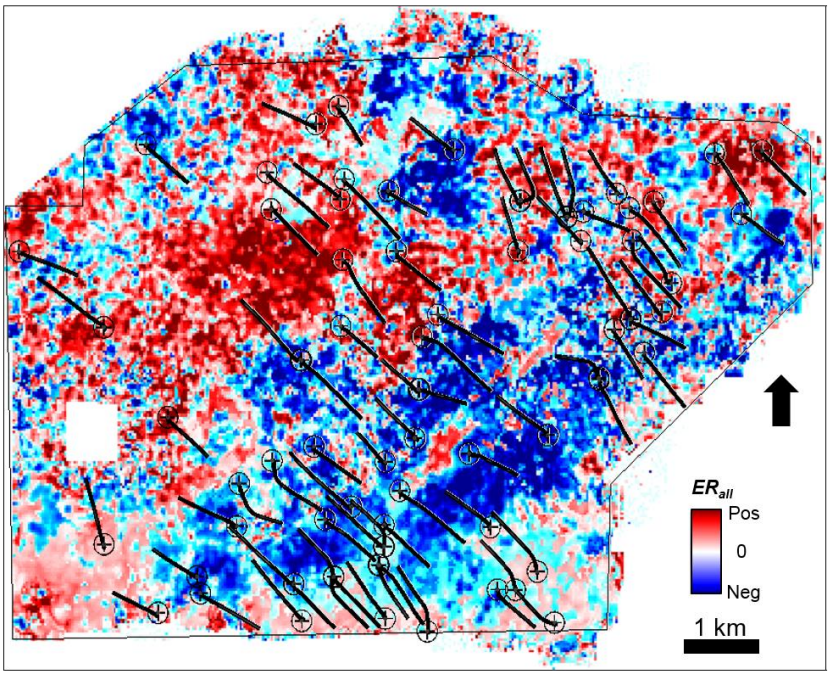

Figure 4.12c

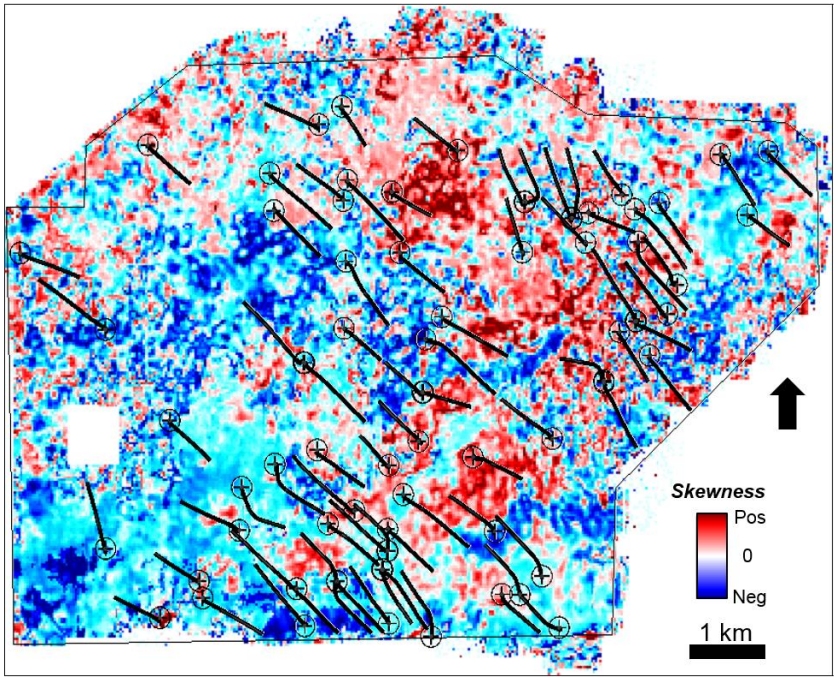

Figure 4.12d

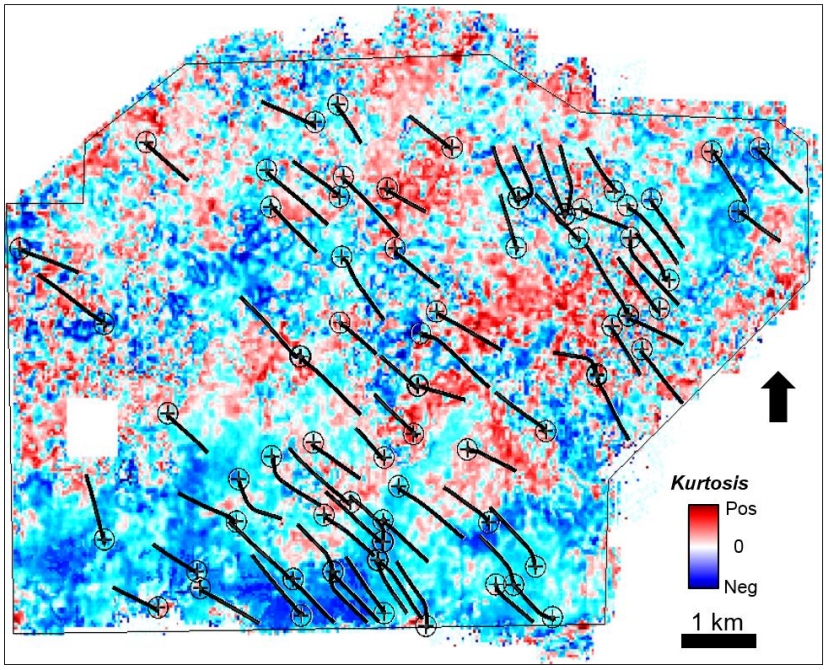

Figure 4.12e

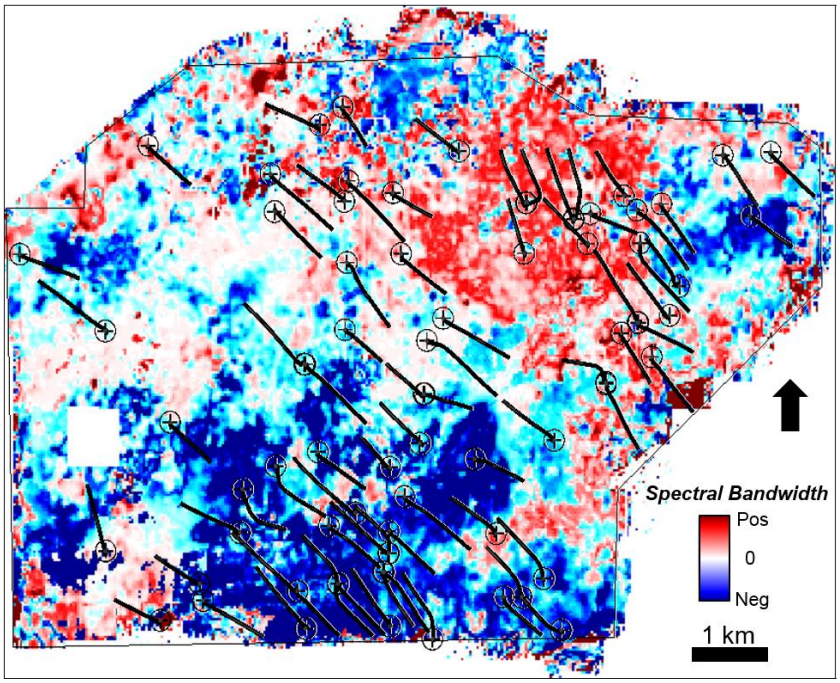

Figure 4.12f

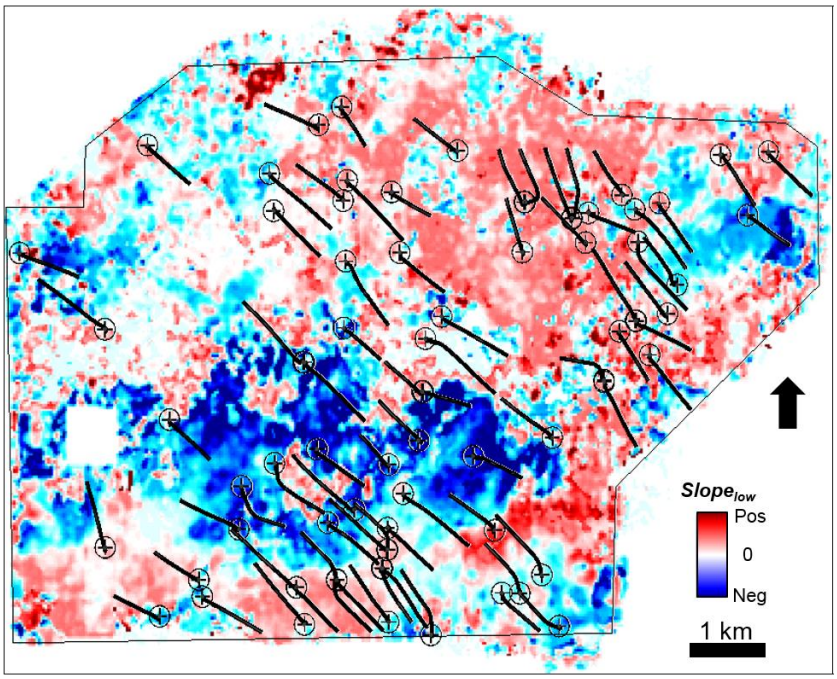

Figure 4.12g

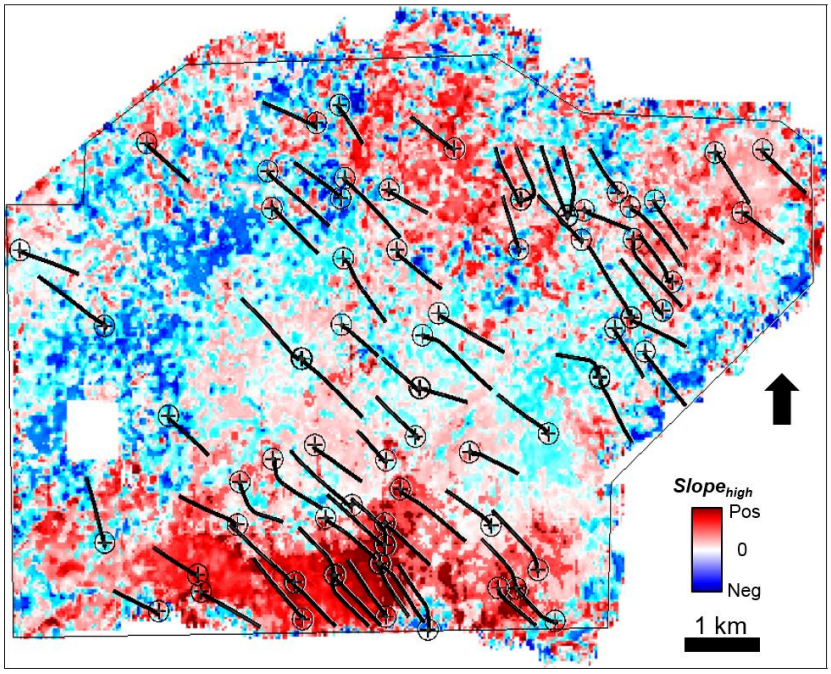

Figure 4.12h

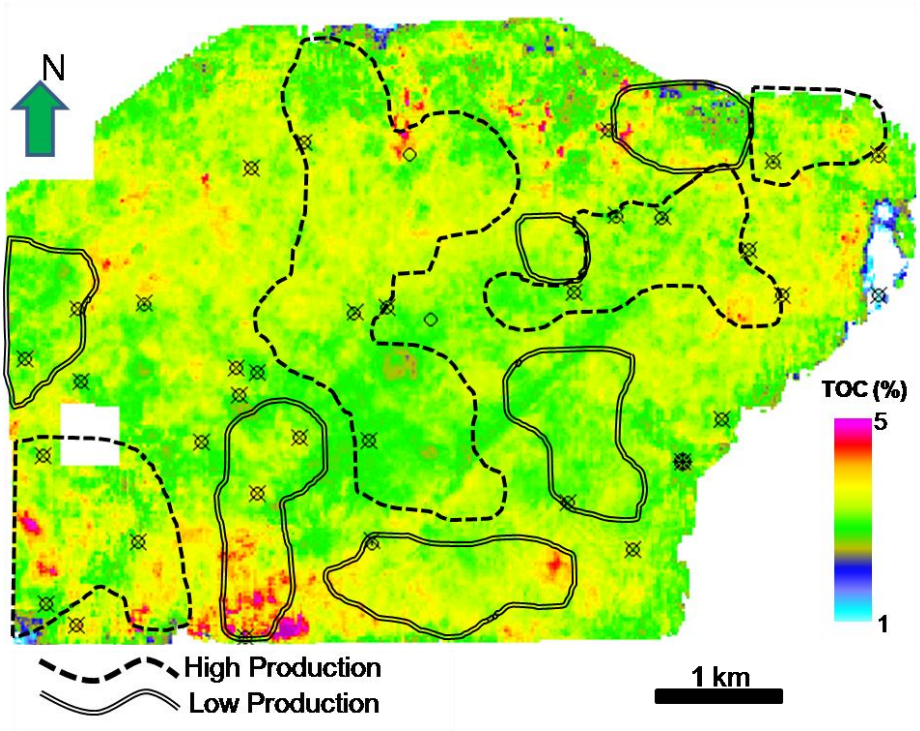

Figure 4.13a

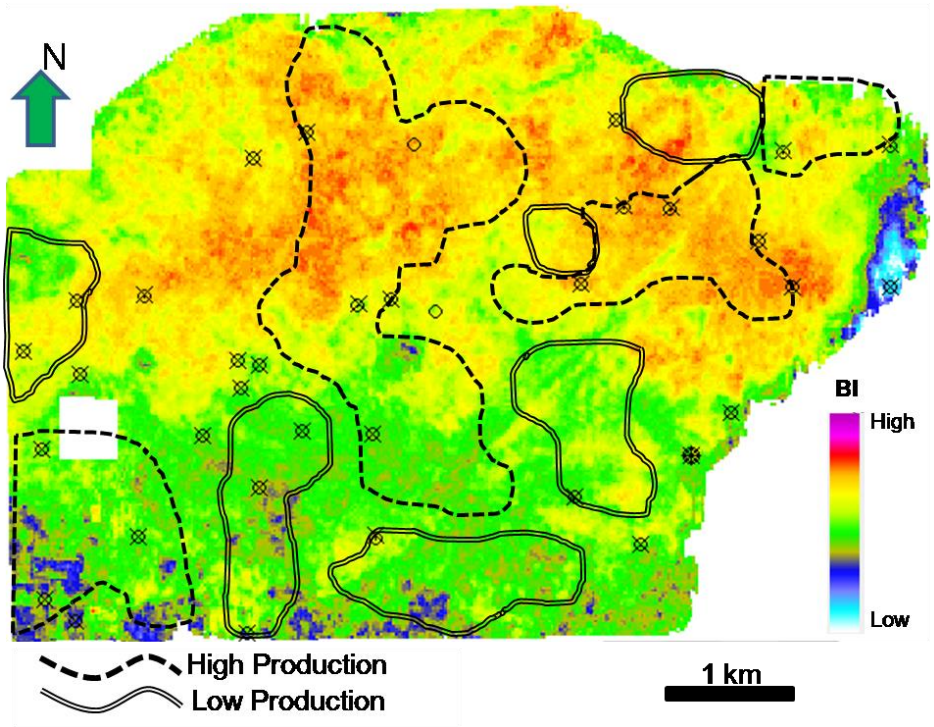

Figure 4.13b

Figure 4.13. Maps of average (a) TOC (total organic carbon) and (b) BI (brittleness index) of Lower Barnett Shale.

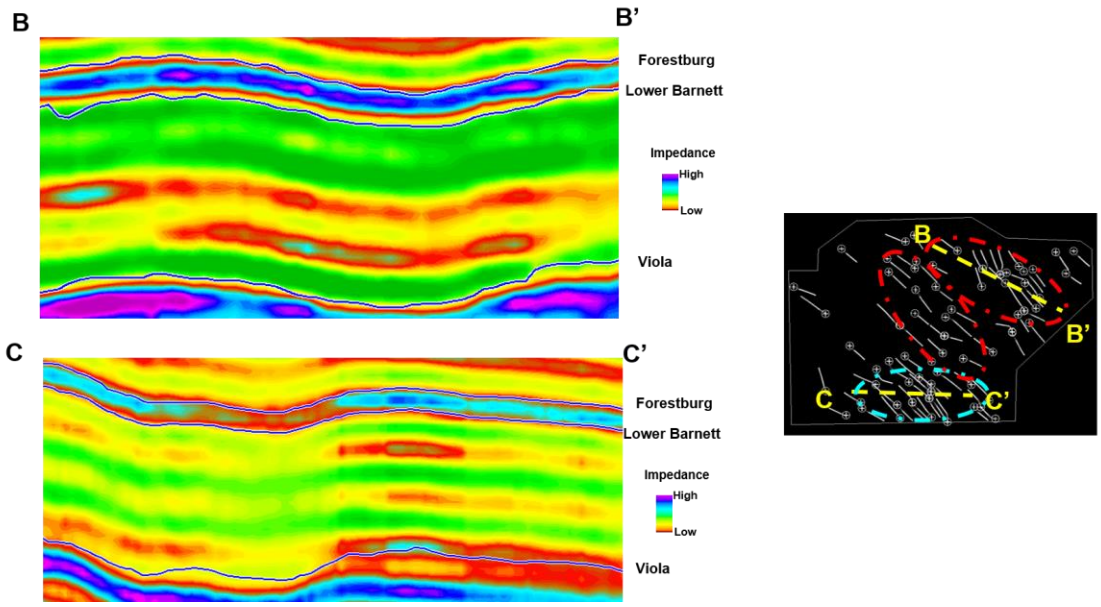

Figure 4.14. Vertical sections of seismic impedance at BB' and CC', denoted at well location map on the right. Red circles highlight high production areas shown in Figure 4.13, while cyan circle highlights a low production area with high density horizontal wells.

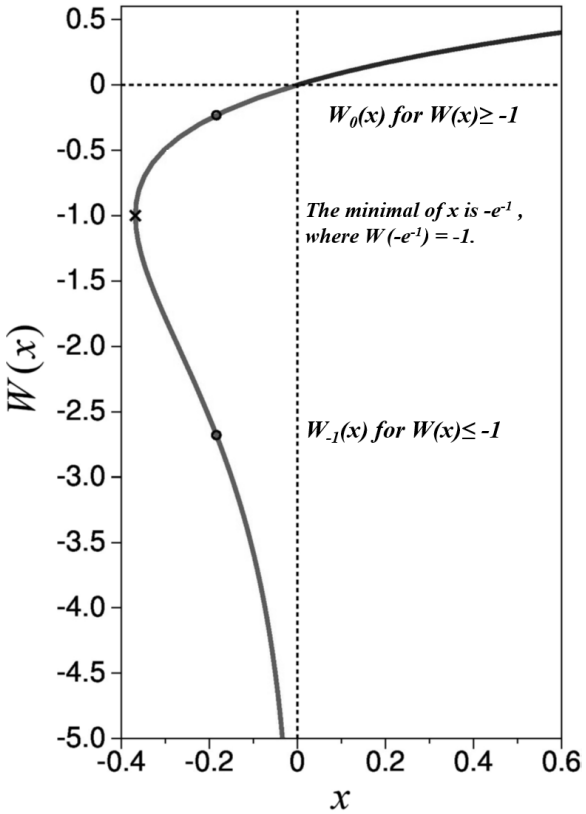

Figure 4.D1. Lambert *W* function, modified from Wang (2015).

REFERENCES

Aki, K., 1969, Analysis of the seismic coda of local earthquakes as scattered waves: Journal of Geophysical Research, **74**, 615–631.

Aki, K., and P. G. Richards, 2002, Quantitative seismology: 2nd ed.: University Science Books.

Anderson, D. L., and C. B. Archambeau, 1964, The anelasticity of the earth: Journal of Geophysical Research, **69**, 2071–2084.

Barnes, 2007, Redundant and useless seismic attributes: Geophysics, **72**, P33–P38.

Biot, M. A., 1956, Theory of propagation of elastic waves in a fluid-saturated porous solid, II. Higher-frequency range: Journal of the Acoustical Society of America, **28**, 168–178.

Blias, E., 2012, Accurate interval Q-factor estimation from VSP data: Geophysics, **77**, WA149–WA156.

Castagna, J., S. Sun, and R. W. Siegfried, 2003, Instantaneous spectral analysis: Detection of low-frequency shadows associated with hydrocarbons: The Leading Edge, **22**, 120–127.

Clark, R. A., P. M. Benson, A. J. Carter, and C. A. Guerrero Moreno, 2009, Anisotropic P-wave attenuation measured from a multi-azimuth surface seismic reflection survey: Geophysical Prospecting, **57**, 835–845.

Cho, D., B. Goodway, M. Perez, A. Iverson and G. Margrave, 2013, 4D-attenuation-analysis-for-permeability-estimates-in-hydraulically-induced induced fractures: CSEG Recorder, **38**.

deFigueiredo, J. J. S., R. R. Stewart, J. Schleicher, N. Dyaur, O. Omoboya, R. Wiley, and A. William, 2011, Frequency dependence of elastic and attenuation properties of cracked media: Ultrasonic modeling studied: 12th International Congress of the Brazilian Geophysical Society, 39-43.

Del Moro, Y., A. Fernandez-Abad, and K. J. Marfurt, 2013, Why should we pay for a merged survey that contains data we already have? An OK Redfork example: The Shale Shaker, **63**, 340-361.

Dvorkin, J., G. Mavko, and A. Nur, 1995, Squirt flow in fully saturated rocks: Geophysics, **60**, 97–107.

Gao, D., 2013, Integrating 3D seismic curvature and curvature gradient attributes for fracture characterization: Methodologies and interpretational implications: Geophysics, **78**, O21-O31.

Gurevich, B., D. Makarynska, O. Bastos de Paula, and M. Pervukhina, 2010, A simple model for squirt-flow dispersion and attenuation in fluid-saturated granular rocks: Geophysics, **75**, N109–N120.

Hermana, M., Z.Z.T. Harith, C.W. Sum, D.P. Ghosh, 2013, The Attribute for Hydrocarbon Prediction Based on Attenuation: International Conferences on Geological, Geographical, Aerospace and Earth Sciences.

Jones T. D., 1986, Pore fluids and frequency- dependent wave propagation in rocks: Geophysics, **51**, 1939-1953

Klimentos, T., 1995, Attenuation of P- and S-waves as a method of distinguishing gas and condensate from oil and waters: Geophysics, **60**, 447 - 458.

Klimentos, T., 1995, Attenuation of P- and S-waves as a method of distinguishing gas and condensate from oil and water: Geophysics, **60**, 447– 458.

Knight, R., L. J. Pyrak-Nolte, L. Slater, E. Atekwana, A. Endres, J. Geller, D. Lesmes, S. Nakagawa, A. Revil, M. M. Sharma, C. Straley, 2010, Geophysics at the interface: Response of geophysical properties to solid-fluid, fluid-fluid, and solid-solid interfaces: Reviews of Geophysics, **48** (4), RG4002.

Lakes, R., 2009, Viscoelastic materials. Cambridge University Press.

Landau, L. D., and E. M. Lifshitz, 1986, Course of theoretical physics, volume 7: Theory of elasticity, 3rd ed.: Butterworth-Heinemann.

Li, F., T. Zhao, T. Lin, and K. J. Marfurt, 2015a, Fracture Characterization based on Attenuation Estimation from Seismic Reflection Data using Well-log-based Localized Spectral Correction: URTeC Expanded Abstract.

Li, F., H. Zhou, L. Li, and K. J. Marfurt, 2015b, Seismic Spectral Attributes of Apparent Attenuation: Part 1 – Methodology: SEG Annual Meeting, New Orleans.

Lynn, H. B., 2004a, The winds of change: Anisotropic rocks — Their preferred direction of fluid flow and their associated seismic signatures — Part 1: The Leading Edge, **23**, 1156–1162.

Lynn, H. B., 2004b, The winds of change: Anisotropic rocks — Their preferred direction of fluid flow and their associated seismic signatures — Part 2: The Leading Edge, **23**, 1258–1268.

Mason, W. P., K. J. Marfurt, D. N. Beshers, and J. T. Kuo, 1978, Internal friction in rocks: J. Acoust. Soc. Am., **63**, 1596–1603.

McGrew, J. C. and C. B. Monroe, 2009, An introduction to statistical problem-solving in Geography: Waveland Press.

Mitchell, J. T., N. Derzhi, E. Lichman, E. N. Lanning, 1996. Energy Absorption Analysis: A case study. SEG Expanded Abstracts, 1785-1788.

Mavko, G., 2013, Relaxation shift in rocks containing poroelastic pore fluids: Geophysics, **78**, M19–M28.

Morozov, I. B., 2008, Geometric attenuation, frequency dependence of Q, and the absorption band problem: Geophysical Journal International, **175**, 239–252,

Morozov, I. B., 2010a, On the causes of frequency-dependent apparent seismological Q: Pure and Applied Geophysics, **167**, 1131–1146.

Morozov, I. B., 2010b, Attenuation coefficients of Rayleigh and Lg waves: Journal of Seismology, **14**, 803–822.

Morozov, I. B., 2011, Mechanisms of geometric attenuation: Annals of Geophysics, **54**, 235–248.

Morozov, I., and A.B. Ahmadi, 2015, Taxonomy of Q: Geophysics, **80**, T41-T49.

Murphy, W. F., K. W. Winkler, and R. L. Kleinberg, 1986, Acoustic relaxation in sedimentary rocks, dependence on grain contacts and fluid saturation: Geophysics, **51**, 757–766.

O'Doherty, R. F., and N. A. Anstey, 1971, Reflections on amplitudes: Geophysical Prospecting, **19**, 430–458.

Palmer I. D. and M. L. Traviolia, 1980, Attenuation by squirt flow in undersaturated gas sands: Geophysics, **45**, 1780-1792.

Parra, J. O., U. Iturrarán-Viveros, J. S. Parra, and P. Xu, 2015, Attenuation and velocity estimation using rock physics and neural network methods for calibrating reflection seismograms: Interpretation, **3**, SA121-SA133.

Perez, R., 2009, Quantitative petrophysical characterization of the Barnett shale in Newark east field, Fort Worth Basin: M. S. thesis, University of Oklahoma.

Perez, R., and K. J. Marfurt, 2014, Mineralogy-based brittleness prediction from surface seismic data: Application to the Barnett Shale: Interpretation, **2**, T255-T271.

Piane, C. D., C. Madonna, J. Sarout, E. H. Saenger, D. Dewhurst, 2014, Frequency-dependent seismic attenuation in shales: experimental results and theoretical analysis: Geophysical Journal International, **198**, 504-515.

Pollastro, R. M., Daniel M. Jarvie, Ronald J. Hill, and Craig W. Adams, 2007, Geologic framework of the Mississippian Barnett Shale, Barnett-Paleozoic total petroleum system, Bend arch–Fort Worth Basin, Texas: AAPG Bulletin, **91**, 405-436.

Quan, Y., and J. M. Harris, 1997, Seismic attenuation tomography using the frequency shift method: Geophysics, **62**, 895–905.

Raikes, S. A., and R. E. White, 1984, Measurements of earth attenuation from downhole and surface seismic recordings: Geophysical Prospecting, **32**, 892–919.

Sayar P. and C. Torres-Verdín, 2017, Effective medium modeling of velocity dispersion and attenuation in isotropic rocks: Geophysics, **82**, D135-D156.

Spencer J. and J. Shine, 2016, Seismic wave attenuation and modulus dispersion in sandstones: Geophysics, **81**, D211-D231.

Suzuki, H., and J. Matsushima, 2013, Quantifying uncertainties in attenuation estimation at methane-hydrate-bearing zones using sonic waveform logs: Geophysics, **78**, D339–D353.

Thompson, A., 2010, Induced fracture detection in the Barnett Shale FT. Worth Basin, Texas: M. S. thesis, University of Oklahoma.

Verma, S., A. Roy, R. Perez, K. J. Marfurt, 2012, Mapping high frackability and high TOC zones in the Barnett Shale: Supervised Probabilistic Neural Network vs. unsupervised multi-attribute Kohonen SOM: SEG Annual Meeting, Las Vegas.

Virieux, J., and S. Operto, 2009, An overview of full-waveform inversion in exploration geophysics: Geophysics, **74**, WCC1–WCC26

Wang, Y., 2015, Frequencies of the Ricker wavelet: Geophysics, **80**, A31-A37.

White, R. E., 1992, Accuracy of estimating Q from seismic data: Geophysics, **57**, 1508–1511.

Yao Q. and D.Han, 2013, Progresses on velocity dispersion and wave attenuation measurements at seismic frequency: SEG Technical Program Expanded Abstracts 2013: pp. 2883-2888.

Young, R.A., A.B. Pankratov, and J.F. Greve, 2004, Method of seismic signal processing: U.S. Patent 6,681,185.

Zhang, C. J., and T. J. Ulrych, 2002, Estimation of quality factors from CMP records: Geophysics, **67**, 1542–1547.

CHAPTER 5

SEISMIC SEQUENCE STRATIGRAPHY ENHANCEMENT USING SEISMIC VARIATIONAL MODE DECOMPOSITION[5]

ABSTRACT

Subtle variations in otherwise similar seismic data can be highlighted in specific spectral components. Highlighting repetitive sequence boundaries can help define the depositional environment, which in turn provides an interpretation framework. Variational mode decomposition is a novel data-driven signal decomposition method that provides several useful features compared to commonly used time frequency analysis. Rather than using predefined spectral bands, the variational mode decomposition method adaptively decomposes a signal into an ensemble of band-limited intrinsic mode functions, each with its own center frequency. Because it is data adaptive, modes can vary rapidly between neighboring traces. I address this shortcoming of previous work by constructing a laterally consistent variational mode decomposition method that preserves lateral continuity, facilitating the extraction of subtle depositional patterns. I validate the accuracy of our method using a synthetic depositional cycle example, and then apply it to identify seismic sequence stratigraphy boundaries for a survey acquired in the Dutch sector, North Sea.

---

[5]*This study is published as a journal paper- Li, F., B. Zhang, R. Zhai, H. Zhou, and K. J. Marfurt, 2016, Depositional sequence characterization based on seismic variational mode decomposition: Interpretation, **5**(2), SB97-SB106.*

INTRODUCTION

Seismic stratigraphy often forms one of the key components of seismic interpretation. Seismic stratigraphy requires the analysis of reflection amplitude, continuity, reflection configuration, and external form (Mitchum et al., 1977; Cross and Lessenger, 1988). Seismic stratigraphy provides a means to identify sequence stratigraphy and sedimentary cycles. Patterns in the seismic data, including onlaps, offlaps, downlaps, truncations and other features allow a skilled interpreter to define whether a given sequence corresponds to a transgressive, regressive, or other stage. Ligtenberg et al. (2006) used the Wheeler (or chronostratgraphic) transform based on the principal of superposition to define geologic events and lithologic units representing a relative geologic time scale. Such seismic stratigraphy and hence sequence stratigraphy information is buried in conventional seismic amplitude volumes (Hart, 2013), though sometimes the quality of seismic data itself limits the extraction of this information.

In the presence of coherent and random noise, sequence boundaries may be buried and thus overlooked on amplitude volumes. Fortunately, this noise may exhibit spectral responses different than those of the underlying signal, suggesting that one may be able to separate the two. Zeng (2013) finds the expression of sequence boundaries to be frequency dependent, where their seismic expression appears quite different if different frequency bands are used. For this reason, spectral decomposition should be able to aid in distinguishing between transgressive and regressive facies in seismic data (Liu et al., 2015). And, I wish to evaluate data-driven signal decomposition as an alternative to commonly used spectral decomposition methods.

The Fourier transform forms the basis of most spectral analysis tools, and provides stationary (not time variant) frequency information. Han and van der Baan (2013) report that since the seismic spectrum changes with time, that non-stationary data analyzed using time frequency analysis (TFA) methods can be beneficial. The short-time Fourier transform (STFT) (Partyka et al., 1999; Lu and Li, 2013) and the continuous wavelet transform (CWT) (Sinha et al., 2005) are two popular TFA tools. These linear analysis methods are constrained by the Heisenberg uncertainty principal that trades off increased temporal resolution with decreased spectral resolution, or increased spectral resolution with decreased temporal resolution (Tary et al. 2014). Matching pursuit (MP) based TFA approaches achieve the highest vertical resolution, whereby the waveforms that are drawn from a mother wavelet library are matched to a seismic trace in an iterative process favoring events with the highest spectral energy (Wang, 2007; Wang et al., 2016). The choice of wavelet library and fitting methods is critical to the performance of MP methods, which sometimes fail to match lower energy events at the low/ high frequencies.

Huang et al. (1998) proposed the popular data-driven empirical mode decomposition (EMD) signal decomposition method to analyze non-stationary signals (Kaplan et al., 2009; Han and van der Baan, 2013; Tary et al., 2014; Honorio et al., 2016). Because EMD decomposes the data into non bandlimited intrinsic mode functions (IMF), it suffers from frequency mixture issues, making the meaning of the results more difficult to interpret. To address this drawback, Dragomiretskiy and Zosso (2014) developed the variational mode decomposition (VMD) to decompose a non-stationary signal into an ensemble of band-limited IMFs. Liu et al. (2016) compared VMD to the alternative of EMD based methods, and found that VMD can express the same seismic data with fewer

intrinsic modes. The STFT, CWT, and MP spectral decompositions provide laterally consistent images for each spectral component. Unfortunately, since each trace is decomposed independently, the characteristics of the "first" or most important EMD or VMD component will vary laterally. While one can use these trace-by-trace algorithms to suppress noise components (Li et al., 2017), vertical slices through any given VMD or EMD component provides little interpretational value. It is the lateral continuity that one wishes to improve.

First, there is a review of the basic theory of VMD. I then describe a laterally consistent VMD method designed to better delineate laterally continuous seismic stratigraphic patterns. I use a synthetic sedimentary model to validate VMD's capability in sedimentary pattern recognition. Finally, I apply VMD to a survey containing deltaic facies acquired in the Dutch sector, North Sea, and conclude with an evaluation of adaptive signal decomposition in analyzing its seismic sequence stratigraphy.

VARIATIONAL MODE DECOMPOSITION (VMD)

Huang et al. (1998) proposed EMD to decompose a data series into a finite set of IMFs. In EMD, the IMF, which represents different oscillations embedded in the data, is calculated in the time domain. To be an IMF, a signal must satisfy two criteria: 1) the number of local maxima and the number of local minima differ by at most one, and 2) the mean of its upper and lower envelopes (a smooth curve outlining signal extremes) must equal zero. EMD has the form:

$$s(t) = \sum_{k=1}^{K} IMF_k(t) + r_K(t), \tag{5.1}$$

where IMF_k is the k^{th} IMF of the signal, and r_K stands for the residual trend. The number, *K*, of EMD outputs cannot be controlled. Liu et al. (2016) also finds that very small unexpected oscillatory interference patterns can change the number of final output modes.

In contrast to EMD, VMD obtains IMFs that exhibit specific sparsity properties in the frequency domain. In VMD, the IMFs are defined as elementary amplitude/frequency modulated harmonics that can model the non-stationarity and the nonlinearity of the data (Appendix 5.A). The frequency spectrum of every IMF is shifted to the baseband by mixing with an exponential function tuned to the respective estimated center frequency. The sparsity of every IMF is constrained by its bandwidth in the frequency domain with the IMF relatively compact about an "oscillation" ω_k, which needs to be determined as part of the decomposition.

In VMD, the IMFs are extracted concurrently instead of recursively, which is achieved by solving the following optimization problem:

$$\begin{aligned} &\min_{\{u_k,\ \omega_k\}} \left\{ \sum_k \left\| \partial_t \left[\left(\delta(t) + \frac{j}{\pi t} \right) * u_k(t) \right] e^{-j\omega_k t} \right\|_2^2 \right\}, \\ &s.\ t. \quad \sum_k u_k = s(t) \end{aligned} \tag{5.2}$$

where u_k and ω_k are modes and their center frequencies, respectively. $\delta(\bullet)$ is a Dirac impulse. $s(t)$ are the data to be decomposed. The term $\left(\delta(t) + \frac{j}{\pi t} \right) * u_k(t)$ is the Hilbert transform of u_k, which is defined in Appendix 5.B. The constraint condition requires that the summation over all modes should approximate the input data.

To solve the optimization problem in Equation 5.2, the alternate direction method of multipliers (ADMMs) (Hestenes, 1969) is employed to estimate IMFs (modes) in the frequency domain as:

$$\hat{u}_k^{n+1}(\omega) = \frac{\hat{s}(\omega) - \sum_{i=1}^{k-1} \hat{u}_i^{n+1}(\omega) - \sum_{i=k+1}^{K} \hat{u}_i^{n}(\omega) + \frac{\hat{\lambda}^n(\omega)}{2}}{1 + 2\alpha\left(\omega - \omega_k^n\right)^2}, \tag{5.3}$$

where, $\hat{s}(\omega)$, $\hat{u}_i(\omega)$ and $\hat{\lambda}(\omega)$ are the Fourier transform of $s(t)$, $u_i(t)$ and $\lambda(t)$, respectively, and n denotes the iterations, λ denotes the Lagrangian multiplier for rendering the problem unconstrained, while α represents the balancing parameter of the data-fidelity constraint.

Traditionally, VMD determines the IMFs trace by trace, such that lateral consistency across the survey may not be preserved. Because seismic data represent the depositional environment, preserving lateral continuity where it exists is critical. Honoro et al. (2016) apply the EMD based methods trace by trace, and observe gaps and "jumps" between neighboring traces. To address this problem, I add lateral consistency constraints in the optimization object function. VMD is achieved by solving the following problem:

$$\left| \begin{array}{l} \underset{\{u_k,\ \omega_k\}}{\mathbf{min}} \left\{ \sum_k \left\{ \left\| \nabla \left[u_{k,A}(\vec{t})\, e^{-j\langle \overrightarrow{\omega_k}, \vec{t} \rangle} \right] \right\|_2^2 + \left\| \mathbf{P}_s\, u_{k,A}(\vec{t}) \right\| \right\} \right\} \\ s.\ t. \quad \sum_k u_k = s(\vec{t}) \end{array} \right. , \tag{5.4}$$

where ∇ is the gradient operator, and where $u_k(\vec{t})$ are the 2D modes and their analytic formats $u_{k,A}(\vec{t})$ described by Equation 5.B-3. $\overrightarrow{\omega_k}$ are the center frequency vectors. $s(\vec{t})$ is the signal to be decomposed, and in the seismic application, it is the vertical seismic section. $\mathbf{P}_s$ is the 2D Wiener prediction filter based on $u_{k,A}(\vec{t})$. (Besides the constraint in

Equation 5.3, for the 3D application, I adopt the mode center frequencies from the neighboring lines as the initial value of the current line, which strengthens the continuity between different lines.)

Figure 5.1 displays a vertical seismic section with IMF-1, IMF-2 and IMF-3 computed using the traditional trace-by-trace VMD method. Note that the lateral consistency is lost. Even a small oscillation can totally change the decomposition results. Such instabilities are a common drawback of high resolution decomposition methods, where it is difficult to suppress noise and structural artifacts can appear. IMF-2 and IMF-3 in Figure 5.1 have almost no interpretational value because of these artificial discontinuities between neighboring traces. Figure 5.2 shows the IMFs from the laterally consistent VMD. The events in Figures 5.2c and 5.2d are continuous and reasonable. Note, the events in Figure 5.2b-5.2d can be combined to explain the reflection changes in Figure 5.2a, which can be helpful for seismic interpretation. Thus, the lateral consistency reinforcement is necessary and effective. In addition, Appendix 5.C explains why it is valid to decompose seismic data into IMFs.

SYNTHETIC DEPOSITIONAL SEQUENCE CHARACTERIZATION

Besides seismic reflection analysis, sequence stratigraphy interpretation can be made based on rock composition, grain size characteristics, spontaneous potential, and Gamma Ray log shapes (Rider, 1999). The transgressive/regressive facies recognition is the key for the stratigraphic sequence division. Well logging, which is usually the source of the geology information, is limited to discrete and widely spaced sampling points

within a survey area. For this reason, one wishes to determine the sedimentary and depositional environment for most areas of interest from the seismic data.

Following Rider (1999) and Martins-Neto and Catuneanu (2009), I build a single cycle of a delta progradational model. The percentage of sandstone increases upward, grain size changes from fine to coarse, with the sandstone interbedded with similar thick shale layers. Figure 5.3 shows the Gamma Ray log decreases upward, annotated by the depositional settings. Figure 5.4 shows the synthetic reflectivity series and corresponding 60ms long seismic amplitude response. The reflectivity series follow the same pattern as the Gamma Ray in Figure 5.3. Because the grain size changes, the seismic reflectivity between shale and sandstone also changes with depth. I apply VMD to the synthetic seismic data, and obtain IMF-1, IMF-2, and IMF-3, shown in Figure 5.4. Note the IMF-1 exhibits the same trend as the Gamma Ray log in Figure 5.3. IMF-2 and IMF-3 display other high frequency information.

FIELD APPLICATIONS

The field data set used in the examples is from the Southern North Sea Basin. After complex multiple stages of orogeny, rift and subsidence that occurred during Paleozoic and Mesozoic time, the Southern North Sea Basin experienced an inversion during the Tertiary. High sediment influx from neighbouring highlands that uplifted in late Miocene filled the basin, resulting in a prograding fluvio-deltaic system. This system (part of the giant Eridanos delta) constitutes the siliciclastic shelf deposits within the Pliocene interval, the thickness is from 350 m to 430m in study area (Overeem et al.,

2001). Several localized unconformities were formed during the deposition process (Sales, 1992; Ghazi, 1992; Gautier, 2003).

The 3D prestack time migration seismic data clearly image the large scale sigmoidal stratal configuration. The dominant frequency is approximate 45Hz, effective bandwidth is from 10Hz to 60 Hz in the study time window. Four wells are used in seismic-to-well calibration (Figure 5.5a). The deltaic cycles in the Dutch sector range from a river-dominated to wave-tide dominated stages. These cycles exhibit classic clinoform geometries prograding towards the basin (Petruno et al., 2015). Figure 5.5b shows our sequence stratigraphy interpretation. Based on the recognition of seismic reflection termination patterns (toplap, onlap, downlap and truncation, shown in Figure 5.5b), five regional and local subaerial unconformities, two maximum regressive surface, two maximum flooding surface and three basal surface of forced regression are defined using a seismic sequence stratigraphic interpretation workflow (Vail et al., 1977, 1987; Mitchum et al., 1977; Posamentier et al., 1999). According to sequence boundaries, position and parasequence stacking pattern, the Pliocene strata of study area can be divided into four third- order sequences. Furthermore, a complete depositional sequence is divided into four system tracks: Lowstand Systems Tracts (LST), Transgressive Systems Tracts (TST), Highstand Systems Tract (HST) and Falling Stage Systems Tract (FSST), on the basis of the principles of quadripartite division for sea level cycle (Hunt and Tucker,1992, 1995; Plint and Nummedal, 2000), such as SQ-1 and SQ-2 in Figure 5.5b. Because of the erosion when relative sea level dropped, SQ-3 and SQ-4 form incomplete depositional records. The delta system that prograded across the continental

shelf during the FSST stage deposited thick sandstone. In the base level rising stage (TST and HST), nonuniform thickness mudstone draped over the delta sandstone.

THE DRAWBACK OF FILTER BANK

The most common spectral component extraction method is to bandpass filter the seismic data. The vertical seismic section in Figure 5.5a shows deltaic facies. I extract a trace (denoted by a red triangle on Figure 5.5a) and display its spectrum in Figure 5.6, and note that the main energy of the spectrum falls between 3 and 80Hz. I design a suite of bandpass filters (0-27Hz, 28-55Hz, and 56-83Hz) to separate the spectral components. Figure 5.7a demonstrates the bandpass filter design. Figure 5.7b displays the filtered spectra of the different spectral bands (SB), which have been normalized on every SB. Figure 5.8 shows the bandpass filtered data. Similar expressions can be found on different SBs. As expected, the thicknesses of the seismic events change from large to small with the frequency increasing. Figure 5.8a displays the low frequency component, which is relatively continuous. However, there are discontinuous artifacts between neighboring traces on Figures 5.8b and 5.8c, which should be brought from the bandpass spectral decomposition. The filter bank breaks the seismic spectrum based on the predefined frequency ranges instead of the intrinsic modes of the data, resulting in discontinuities of waveforms.

THE VALUE OF ADAPTIVE MODE DECOMPOSITION

To obtain the sequence stratigraphy interpretation in Figure 5.5b, I spend efforts on sequence boundary identification, especially when the seismic reflections are not clear.

As discussed above, signal decomposition methods can highlight specific components commonly buried in the seismic data. Since the filter bank method failed in assisting seismic stratigraphy interpretation, I apply VMD, a data-driven mode decomposition method, on the seismic data. Figure 5.9 shows the spectra of IMFs of the trace denoted by a red triangle on Figure 5.5a. Unlike the spectra in Figure 5.7b, every IMF is an ensemble spectral component, which is not strictly limited to a certain band. Figures 5.10a - 5.10c display the vertical sections of IMF-1, IMF-2, and IMF-3, respectively. The IMF-1 in Figure 5.10a shows the low frequency background. Compared to Figure 5.8a, IMF-1 has a lower dominant frequency, but it also shows some details brought from the high frequencies. The IMFs from VMD are more continuous, as there are no artificial discontinuities between neighboring traces. Compared with the results in Figure 5.8 and those in Figure 5.10, the conflicts between human defined methods and data-driven approaches are obvious. The parameter pre-defined decomposition arbitrarily divides seismic data into spectral bands, and could result in the deformation of a geological structure in waveform. Nonetheless, the adaptive decomposition I adopted can keep the relative completeness of intrinsic modes buried in the seismic signal, which reveals hidden geology information.

On Figure 5.10, stratigraphic terminations, such as onlap, toplap, downlap, and truncation, are labelled, like Figure 5.5b. In Figure 5.10a, the subaerial unconformities (SUs), maximum flooding surfaces (MFSs) and basal surface of forced regression (BSFR) show strong energies. One can also observe the onlap, toplap, downlap, and truncation features. In Figure 5.10b, the onlaps, toplaps and downlaps are very clear, as well as the stratal clinoforms, which is low amplitude and hard to observe on Figure 5.5a.

The SUs and MFSs show high amplitudes on IMF-3. Though the stratigraphy details are not clear on Figure 5.10c, one can have a rough conception where is the clinoform. In Figure 5.10d, IMF-1 and IMF-2 are color blended together. Two depositional sequences, SQ-1 and SQ-2, show up more clearly, compared to the original seismic section. Thanks to the new details, the VMD does assist the stratigraphy interpretation.

DISCUSSIONS

Machine learning facies analysis tools usually project *n* attributes residing in an *n*-dimensional space onto a lower (in my case, 2D) dimensional deformed manifold. In general, there is little large scale spatial information provided to the classification. Since the IMFs provided by VMD provide such large scale (specifically, sedimentary layering) patterns. Because of the improved lateral consistency, VMD IMF components form an excellent candidate as input to machine learning based seismic facies classification (Zhao et al., 2017). I also hypothesize that by their addition, one can incorporate the seismic stratigraphy patterns effectively used by skilled interpreters into the classification result. such patterns into the result (Li et al., 2016b). The choice of which IMF or collection of IMFs to use requires calibration with geologic control. Ideally, well logs provide the necessary ground truth.

CONCLUSIONS

Using the seismic data and a limited number of well logs, I evaluate the use of VMD in the identification of the depositional sequences. I find laterally consistent VMD provides images amenable to detailed sequence stratigraphic interpretation, providing components that are easier to interpret than either the broad band input data, or more commonly used band-pass filtered (spectral voices) versions of the data.

APPENDIX

5.A INTRINSIC MODE FUNCTION (IMF)

Intrinsic Mode Functions (IMFs) are amplitude-modulated-frequency-modulated (AM-FM) signals, written as:

$$u_k(t) = A_k(t)\cos\left(\phi_k(t)\right), \tag{5.A-1}$$

where the phase $\phi_k(t)$ is a non-decreasing function, $\phi_k'(t) \geq 0$, the envelope is non-negative $A_k(t) \geq 0$. Both the envelope $A_k(t)$ and the instantaneous frequency $\omega_k(t) = \phi_k'(t)$ vary slower than the phase $\phi_k(t)$ (Gilles, 2013). In other words, on a sufficiently long interval, the mode $u_k(t)$ can be considered as a pure harmonic signal.

5.B ANALYTIC SIGNAL

Let $s(t)$ be a real signal, then the complex analytic signal is defined as

$$s_A(t) = s(t) + iH\left(s(t)\right) = s(t) * \left(\delta(t) + \frac{i}{\pi t}\right), \tag{5.B-1}$$

where $H(\bullet)$ is the Hilbert transform, and $*$ denotes the convolution operation .

The analytic signal of IMF in Equation 5.A-1 can be expressed as

$$u_{k,A}(t) = u_k(t) * \left(\delta(t) + \frac{i}{\pi t}\right). \tag{5.B-2}$$

Following a definition in Bülow and Sommer (1999), we can define the 2D analytic signal of IMF as:

$$u_{k,A}(\vec{t}) = u_k(\vec{t}) * \left(\delta\left(\left\langle \vec{t}, \overrightarrow{\omega_k} \right\rangle\right) + \frac{i}{\pi\left\langle \vec{t}, \overrightarrow{\omega_k} \right\rangle}\right)\delta\left(\left\langle \vec{t}, \overrightarrow{\omega_k}, \perp \right\rangle\right), \tag{5.B-3}$$

where $\overrightarrow{\omega_k}$ is the frequency vector in 2D plane. Here, the transform is separable: the analytic signal is calculated line-wise along the direction of $\overrightarrow{\omega_k}$. The two dimensions are processed independently, and show the properties as 2D Fourier transform.

5.C SEISMIC SPECTRUM WITH LINEAR EVENTS

I adopt plane wave assumption to characterize seismic propagation. If there is a linear event, the seismic signal can be expressed as a plane wave:

$$d(t,x) = w\left(t - \frac{x}{c}\right), \tag{5.C-1}$$

where x, t stand for the coordinates of offset axis and time axis. The w is the waveform, such as Ricker wavelet. c is the wave propagation velocity.

Applying Fourier transform along t axis of Equation 5.C-1, the f-x spectrum can be obtained:

$$D(f,x) = W(f)e^{i\frac{2\pi fx}{c}}, \tag{5.C-2}$$

where f is the frequency, W is the Fourier transform of w.

For the discrete situation, I assume the sampling interval in x axis is Δx, then

$$D_f(m) \equiv D(m\Delta x, f), \qquad m = 1,2,\ldots,M, \tag{5.C-3}$$

where m is the trace number, M is the total number of the traces.

In addition, there is a constant exponential relationship between two adjacent traces:

$$D_f(m) = D_f(m-1)e^{i\frac{2\pi f\Delta x}{c}}. \tag{5.C-4}$$

From Equation 5.C-4, I know the frequency slice D_f includes one complex harmonic in f-x domain. Bekara and van der Baan (2009) conclude that the superposition of p linear events in the t-x domain is equivalent to the superposition of p complex harmonics in f-x domain.

Thus, based on the IMF definition in Appendix 5.A and the series theory, it is valid to decompose seismic data into IMFs.

CHAPTER 5 FIGURES

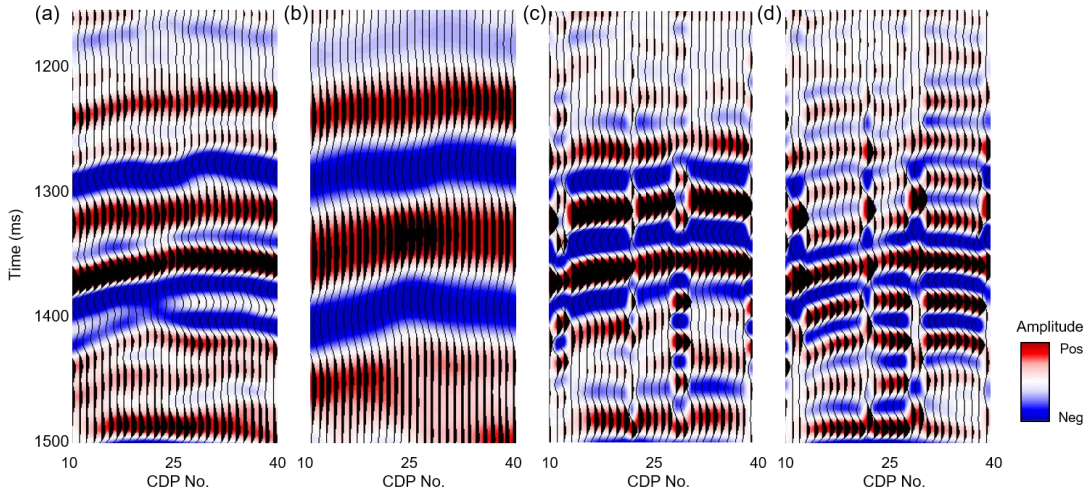

Figure 5.1. IMFs from traditional VMD. (a) Seismic and (b-d) IMF-1, IMF-2, and IMF-3. Note that the low frequency mode section is continuous, but IMF-2 and IMF-3 show poor lateral consistency.

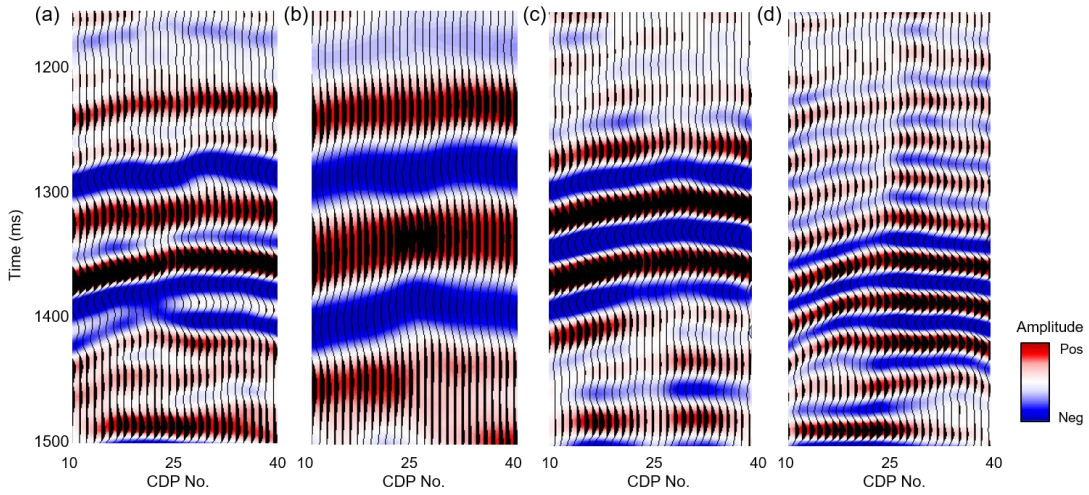

Figure 5.2. IMFs from laterally consistency constrained VMD. (a) Seismic and (b-d) IMF-1, IMF-2, and IMF-3, corresponded with Figures 5.1b-5.1d, respectively. All the decomposed modes are continuous laterally because of the constraint in the VMD calcuation equation.

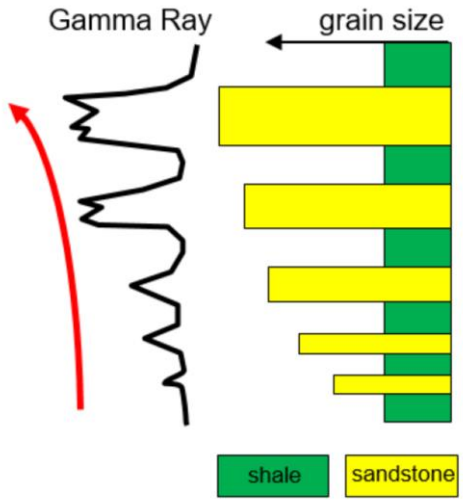

Figure 5.3. Gamma Ray log shape and depositional setting of deltaic progradational depositional trends, modified from Rider (1999). The sandstone is coarsening upward, and its thickness is also increasing upward interbeded with similar thick shale. The Gamma Ray value becomes smaller upward.

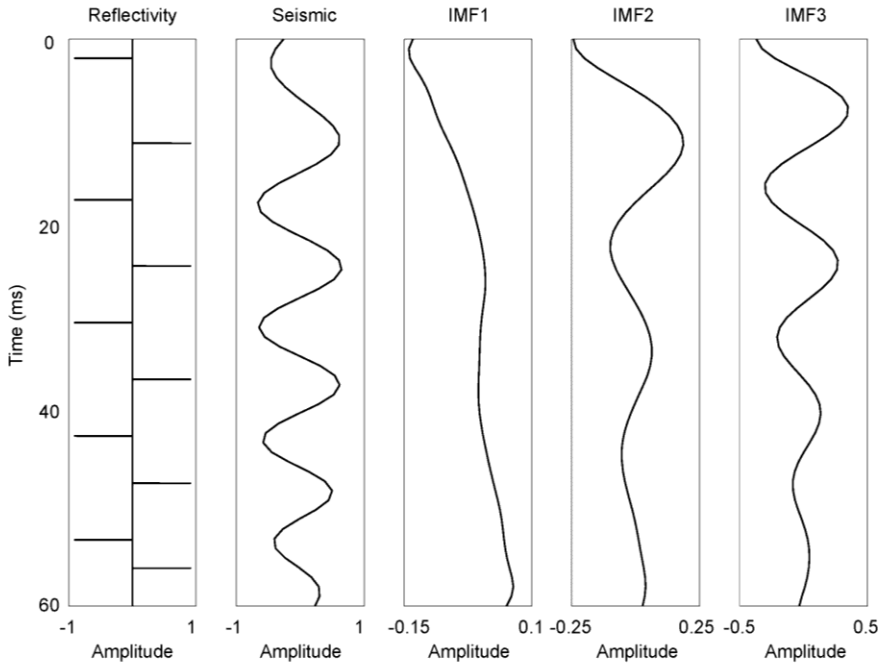

Figure 5.4. Reflectivity series, corresponding seismic trace, and IMF-1, IMF-2 and IMF-3 of the delta progradational model in Figure 5.3. Note that the amplitude of IMF-1 decreases upward like the Gamma Ray log in Figure 5.3.

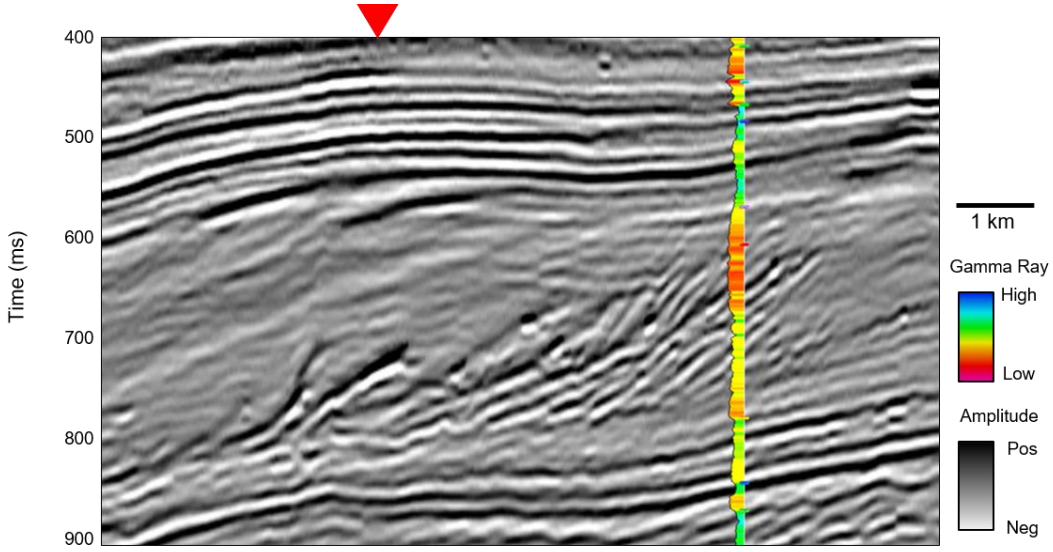

Figure 5.5a

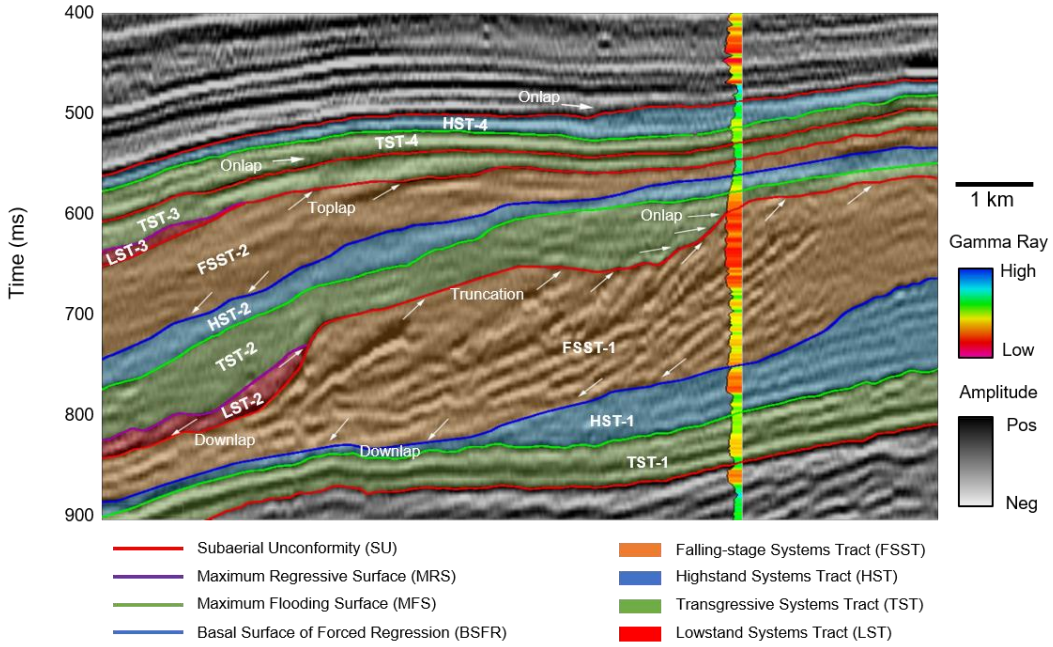

Figure 5.5b

Figure 5.5. A vertical well with posted Gamma Ray log, and a vertical slice through the seismic amplitude volume perpendicular to the shore face (a) without, and (b) with sequence stratigraphy interpretation. According to the recognized isochronous stratigraphic interfaces, the Pliocene strata are divided into four third-order sequences (SQ). From the onset of base level rise to the end of base level fall, one complete base level cycle is divided into four stages, LST, TST, HST, and FSST. SQ-1 and SQ-2 contain relative complete system tracts, SQ-3 and SQ-4 only retain the strata records of base level rising because of regional erosion.

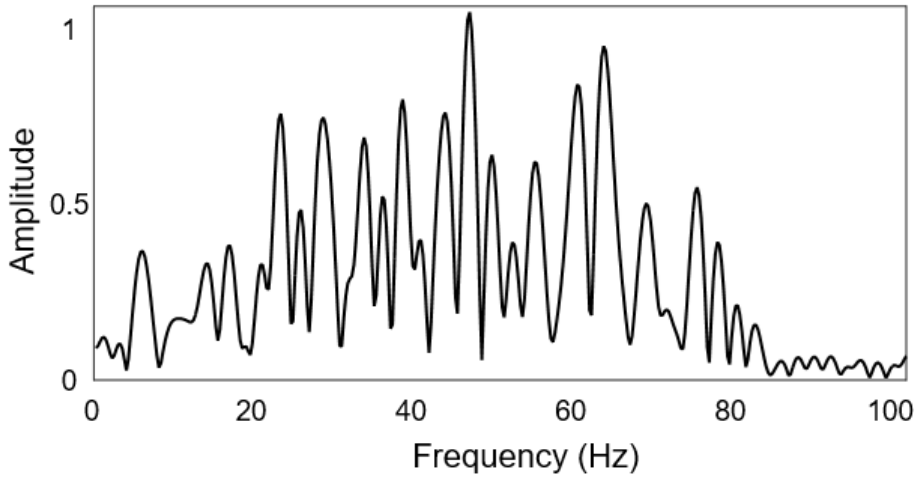

Figure 5.6. Spectrum of the trace denoted by a red triangle on Figure 5.5a.

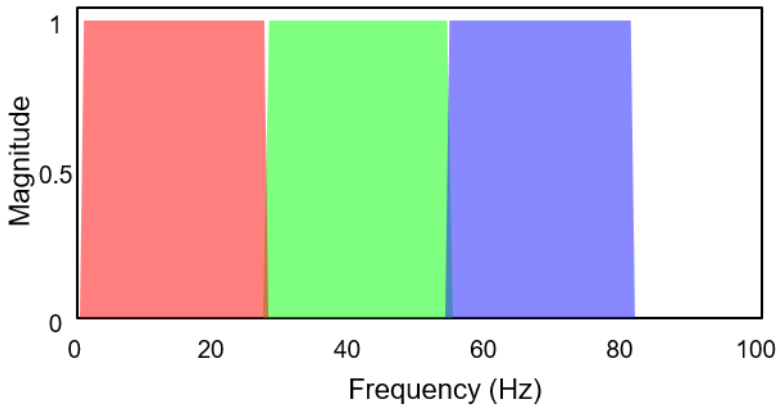

Figure 5.7a

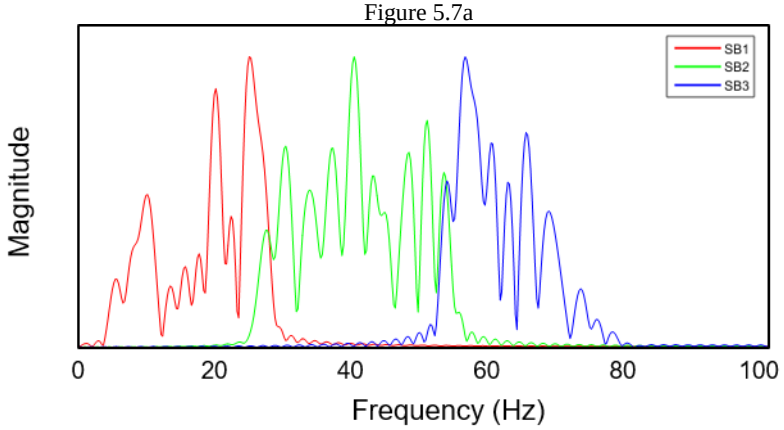

Figure 5.7b

Figure 5.7. (a) Bandpass filter design with three spectral bands (SB): 0-27Hz, 28-55Hz, and 56-83Hz. (b) Filtered spectra with normalization on every spectral band.

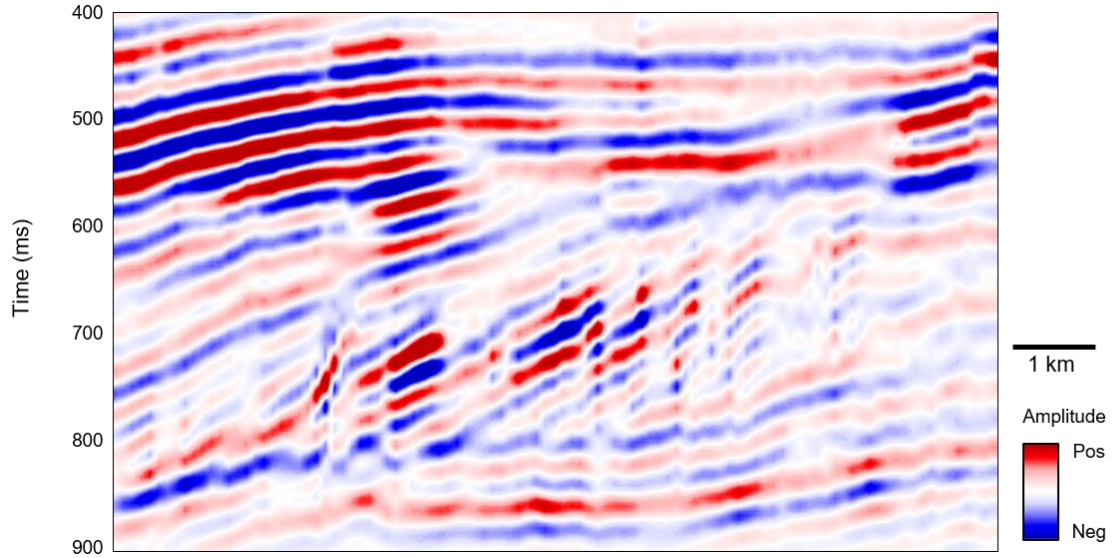

Figure 5.8a

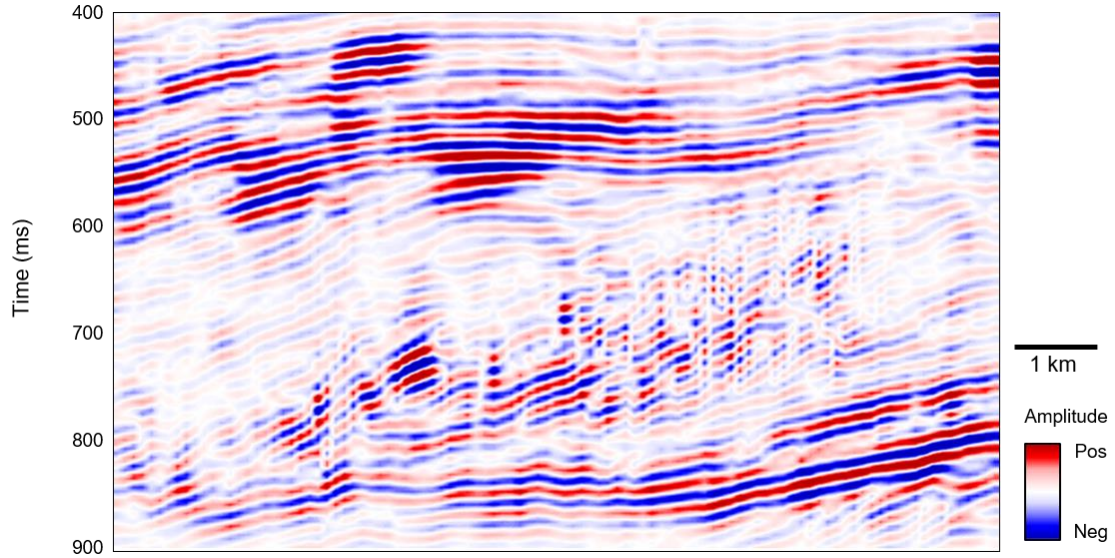

Figure 5.8b

Figure 5.8. Bandpass filtered components: (a) 0-27Hz, (b) 28-55Hz, and (c) 56-83Hz. The apparent vertical discontinuities in the resulting images are due to changes in tuning and have little to do with the depositional environment or structural changes, making analysis of such images difficult.

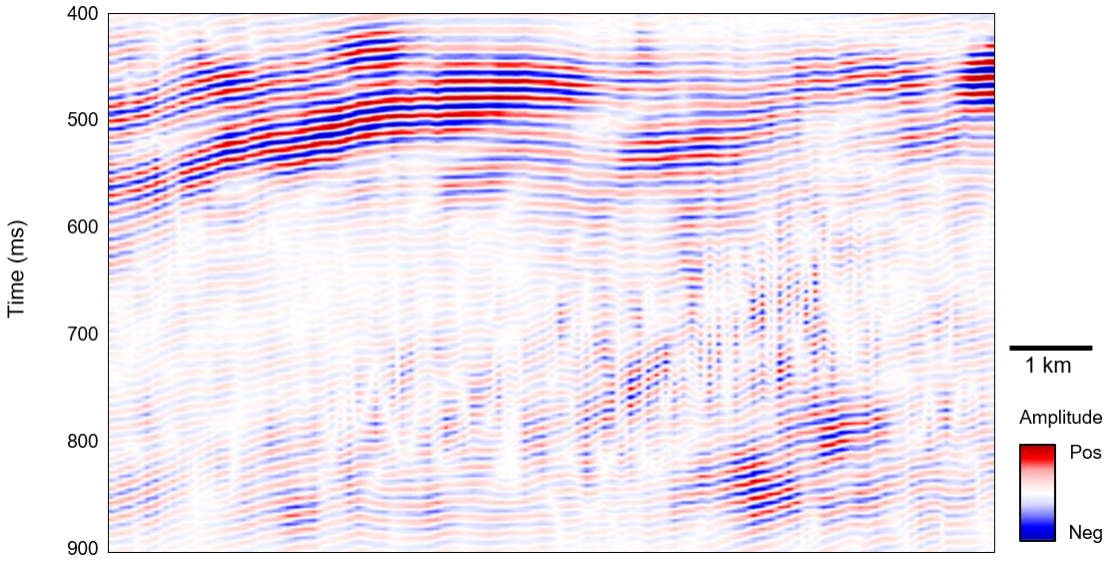

Figure 5.8c

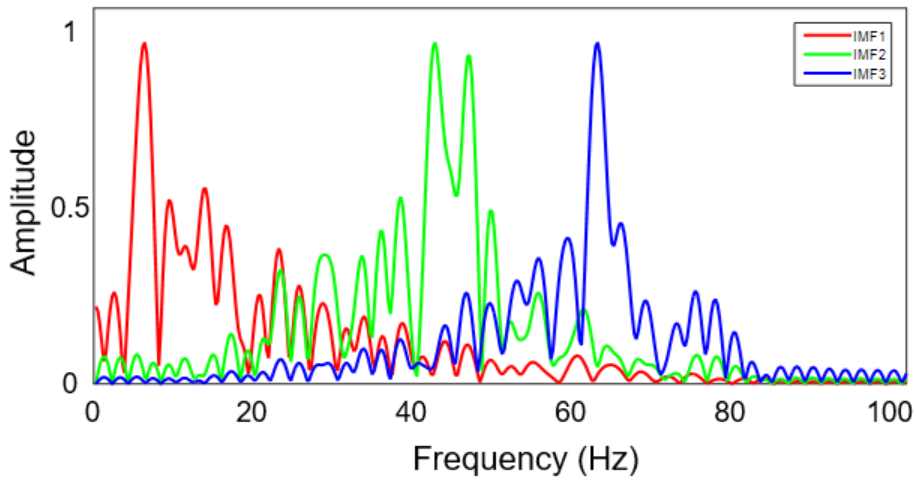

Figure 5.9. Spectra of IMFs of the trace denoted by the red triangle on Figure 5.5a with normalization of each mode.

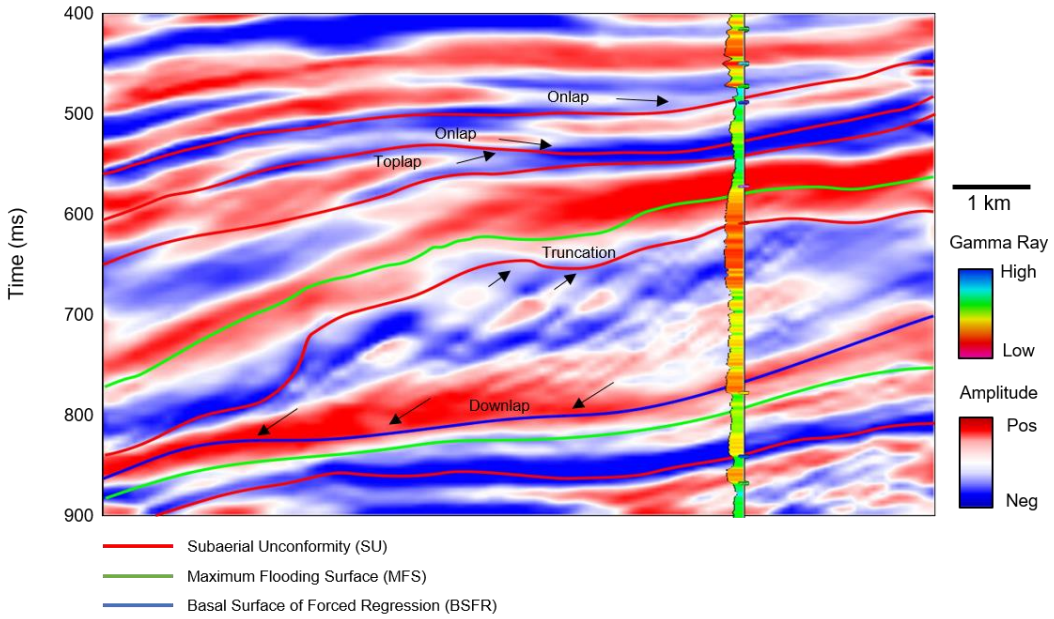

Figure 5.10a

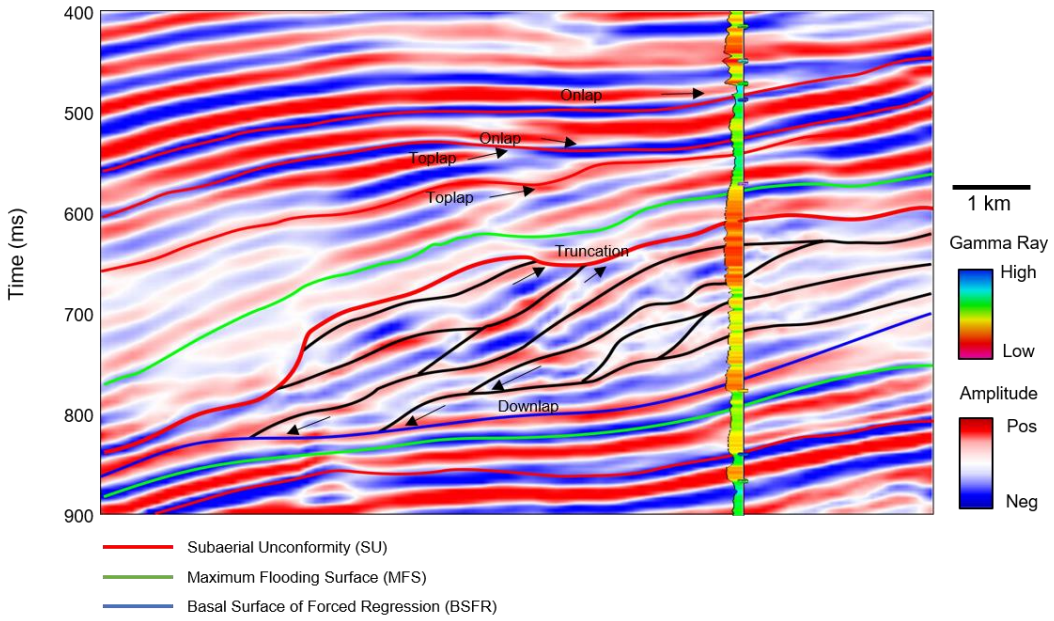

Figure 5.10b

Figure 5.10. Sequence stratigraphy interpretation on (a) IMF-1, (b) IMF-2, and (c) IMF-3, corresponding to Figure 5.5b. Note the improved lateral continuity compared to the spectral decomposition image shown in Figure 5.8. The high amplitudes on IMF-1 highlight SUs, MFSs and BSFR. Stratigraphy terminations are clear in both IMF-1 and IMF-2, with the clinoform more clearly imaged by IMF-2. The SUs and MFSs exhibit high amplitudes on IMF-3, but the stratigraphy details seen in IMF-1 and IMF-2 are not clear. In general, the components needed to generate a sequence stratigraphic interpretation are more clearly imaged on IMFs than in the broad band input data shown in Figure 5.5a and bandpass filtered data in Figure 5.8. (d) By blending addition IMF-1 and IMF-2, one can delineate the two depositional sequences, SQ-1 and SQ-2 (dotted triangle).

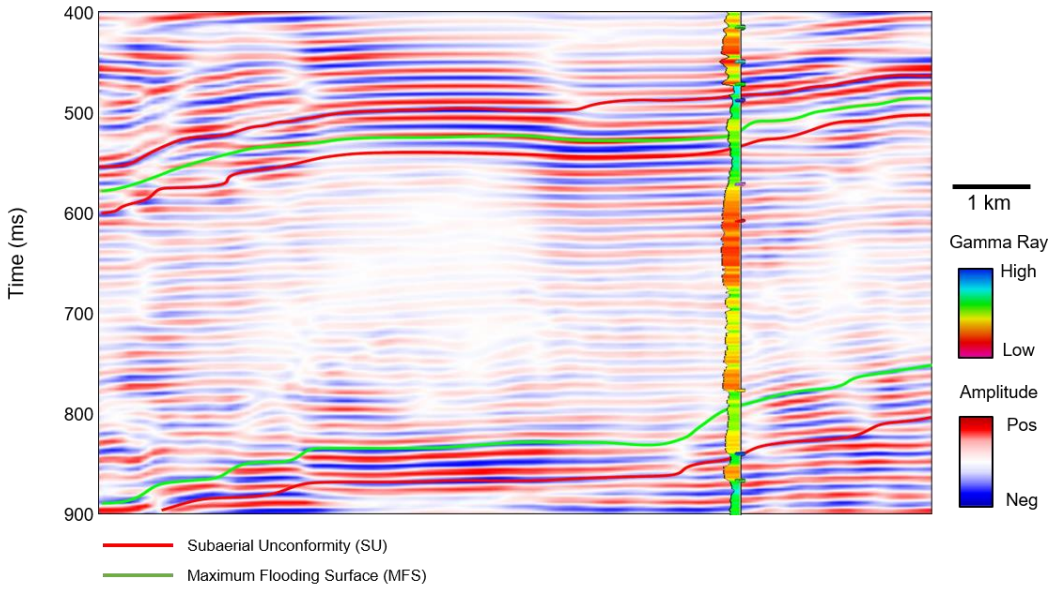

Figure 5.10c

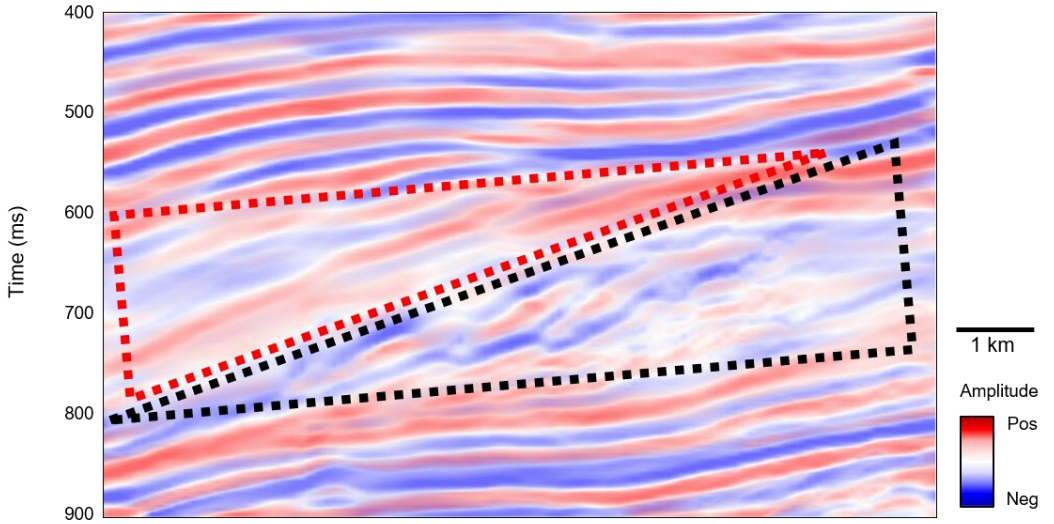

Figure 5.10d

REFERENCES

Bekara, M. and M. van der Baan, 2009. Random and coherent noise attenuation by empirical mode decomposition: Geophysics, **74**(5), V89-V98.

Bülow, T. and G. Sommer, 1999, A novel approach to the 2D analytic signal: Computer Analysis of Images and Patterns, 25-32.

Cross, T. A., and M. A. Lessenger, 1988, Seismic stratigraphy: Annual Review of Earth and Planetary Sciences, **16**, 319.

Dragomiretskiy K. and D. Zosso, 2014, Variational mode decomposition: IEEE Transactions on Signal Processing, **62**(3), 531-544.

Gautier, D. L., 2003, Carboniferous-Rotliegend Total Petroleum System Description and Assessment Results Summary: USGS Bulletin.

Ghazi, S.A., 1992, Cenzoic uplift in the Stord Basin area and its consequences for exploration. In: Jense L. N., and Riis F. (eds) Post-Cretaceous uplift and sedimentation along the western Fennoscandia Shield: Norsk Geologisk Tidsskrift, **72**, 3, 285-290.

Gilles, J., 2013, Empirical wavelet transform: IEEE Transactions on Signal Processing, **61**(16), 3999-4010.

Han, J. and M. Van der Baan, 2013, Empirical mode decomposition for seismic time-frequency analysis: Geophysics, **78** (2), O9-O19.

Hart, B.S., 2013, Whither seismic stratigraphy?: Interpretation, **1**(1), SA3-SA20.

Hestenes, M. R., 1969, Multiplier and gradient methods: Journal of Optimization Theory and Applications, **4**, 303–320.

Honorio, B., A. Vidal, and M. Matos, 2016, Progress on empirical-mode decomposition-based techniques and its impacts on seismic-attribute analysis: SEG Technical Program Expanded Abstracts, 2118-2122.

Huang, N. E., Z. Shen, S. R. Long, M. C. Wu, H. Shih, Q. Zheng, N.-C. Yen, C. Tung, and H. Liu, 1998, The empirical mode decomposition and the Hilbert spectrum for nonlinear and non-stationary time series analysis. Proceedings of the Royal Society of London: Mathematical, Physical and Engineering Sciences, **454**, 903-995.

Hunt, D., M.E. Tucker, 1992, Stranded parasequences and the forced regressive wedgesystems tract: deposition during base-level fall: Sedimentary Geology, **81**, 1–9.

Hunt, D., M.E. Tucker, 1995, Stranded parasequences and the forced regressive wedgesystems tract: deposition during base-level fall—reply: Sedimentary Geology, **95**, 147–160.

Kaplan, S. T., M. D. Sacchi, and T. J. Ulrych, 2009, Sparse coding for data-driven coherent and incoherent noise attenuation: SEG Annual Meeting, 3327-3331.

Li, F., S. Verma, H. Zhou, T. Zhao, K.J. Marfurt, 2016a, Seismic attenuation attributes with applications on conventional and unconventional reservoirs: Interpretation, **4**(1), SB63-SB77.

Li, F., T. Zhao, Y. Zhang, K.J. Marfurt, 2016b, VMD based sedimentary cycle division for unconventional facies analysis: UrTeC expanded abstract, 1311-1319.

Ligtenberg, H., G. de Bruin, and N. Hemstra, 2006, Sequence Stratigraphic Interpretation in the Wheeler Transformed (Flattened) Seismic Domain: 68th EAGE Conference & Exhibition, Vienna.

Liu, W., S. Cao, and Y. Chen, 2016, Applications of variational mode decomposition in seismic time-frequency analysis: Geophysics, **81**, 5, V365–V378.

Liu Y., G. Yang, and W. Cao, 2015, The Division of Sedimentary Cycle based on HHT: SEG Technical Program Expanded Abstracts, 1902-1906.

Lu, W. K., and F. Y. Li, 2013, Seismic spectral decomposition using deconvolutive short time Fourier transform spectrogram: Geophysics, **78**, 2, V43–V51.

Martins-Neto, M. A., and O. Catuneanu, 2010, Rift sequence stratigraphy: Marine and Petroleum Geology, **27**(1), 247-253.

Mitchum, R.M., P.R. Vail Jr., and S. III. Thompson, 1977, Seismic stratigraphy and global changes of sea level; Part 2, The depositional sequence as a basic unit for stratigraphic analysis, in Payton, C.E., ed., Seismic stratigraphy; applications to hydrocarbon exploration: American Association of Petroleum Geologists (AAPG) Memoir **26**, 53–62.

Overeem I., G. J. Weltje, C. BishopKay, and S. B. Kroonenberg, 2001, The Late Cenozoic Eridanos delta system in the Southern North Sea Basin: a climate signal in sediment supply?: Basin Research, **13**, P293-312.

Partyka, G., J. Gridley, and J. Lopez, 1999, Interpretational applications of spectral decomposition in reservoir characterization: The Leading Edge, **18,** 353–360.

Patruno, S., G.J. Hampson, and C.A. Jackson, 2015, Quantitative characterisation of deltaic and subaqueous clinoforms: Earth-Science Reviews, **142**, 79-119.

Perez, R., and K. J. Marfurt, 2014, Mineralogy-based brittleness prediction from surface seismic data: Application to the Barnett Shale: Interpretation, **2**(4), T255-T271.

Plint, A.G., and D. Nummedal, 2000, The falling stage systems tract: recognition and importance insequence stratigraphic analysis. In: Hunt, D., Gawthorpe, R.L. (Eds.), Sedimentary Response toforced regression, vol. 172: Geol. Soc. London Speci. Publ, 1–17.

Posamentier, H.W., G.P. Allen, 1999, Siliciclastic sequence stratigraphy: concepts and applications: SEPM Concepts in Sedimentology and Paleontology, **7**, 210.

Rider, M.H., 1999, Geologic interpretation of well logs: Whittles Publishing Services.

Sales J. k., 1992, Uplift and subsidence of northwestern Europe: causes and influence on hydrocarbon entrapment. In: Jense L. N., and Riis F. (eds) Post-Cretaceous uplift and sedimentation along the western Fennoscandia Shield: Norsk Geologisk Tidsskrift, **72**, 3, 253-258.

Sinha, S., P. S. Routh, P. D. Anno, and J. P. Castagna, 2005, Spectral decomposition of seismic data with continuous-wavelet transform: Geophysics, **70**, P19–P25.

Tary, J. B., Herrera, R. H., Han, J., and M. van der Baan, 2014, Spectral estimation-what is new? what is next?: Reviews of Geophysics, **52**(4), 723-749.

Vail, P. R., R. M. Mitchum Jr, and S. III. Thompson, 1977, Seismic stratigraphy and global changes of sea level, part 3: relative changes of sea level from coastal onlap. In: PAYTON, C. E. (ed.) Seismic Stratigraphy -Applications to Hydrocarbon Exploration: American Association of Petroleum Geologists Memoirs, **26**, 63-81.

Vail, P.R., 1987, Seismic stratigraphy interpretation procedure. In: Bally, A.W. (Ed.), Atlas of Seismic Stratigraphy, **27**: American Association of Petroleum Geologists (AAPG) Studies in Geology, 1–10.

Wang, X., B. Zhang, F.Y. Li, J. Qi, and B. Bai, 2016, Seismic time-frequency decomposition by using a hybrid basis-matching pursuit technique: Interpretation, **4**(2), T239-T248.

Wang, Y., 2007, Seismic time-frequency spectral decomposition by matching pursuit: Geophysics, **72**, V13–V20.

Zhao, T., F.Y. Li, and K.J. Marfurt, 2017, Constraining self-organizing map facies analysis with stratigraphy: An approach to increase the credibility in automatic seismic facies classification: Interpretation, **5**(2), T163-T171.

Zeng, H., 2013, Frequency-dependent seismic-stratigraphic and facies interpretation: AAPG bulletin, **97**(2), 201-221.

CHAPTER 6
SEISMIC SIGNAL DENOISING USING THRESHOLDED VARIATIONAL MODE DECOMPOSITION[6]

ABSTRACT

Noise reduction is an important step prior to seismic interpretation. In this chapter, I describe an adaptive denoising method based on data-driven signal mode decomposition, where the noise is represented by the residual. First, I use signal mode decomposition methods to decompose noisy data. I assume that the residual/last mode component represents noise, which is determined by detrended fluctuation analysis. Then, I subtract the residual/last mode from the noisy data to obtain the denoised result. The advantage of this approach is that the noise is adaptively extracted with depending on the statistics of data, rather than defining a fixed priori threshold. Removing the unwanted noisy component yields a signal with less noise while preserving its intrinsic characteristics. To illustrate the effectiveness of the proposed workflow, I apply it on both synthetics and field seismic data to demonstrate its potential in filtering noise and enhancing seismic data quality.

[6] *This chapter is accepted to Exploration Geophysics titled as "Seismic Signal Denoising Using Thresholded Variational Mode Decomposition" in June 12, 2017.*

INTRODUCTION

Seismic data are non-stationary because of intrinsic attenuation, attenuation from rugose surfaces, reverberations, and both random and coherent noise. Most filters represent the seismic data by a suite of components. The processor then identifies and mutes the noise components, where the simplest means of identification is to use a threshold (Donoho and Johnstone, 1994; Bekara and van der Baan, 2009; Chkeir et al., 2010; Fang et al., 2011; Kabir and Shahnaz, 2012; Gan et al., 2014; Li et al., 2015). Lahmiri and Boukadoum (2014) and He and Bai (2016) summarize the advantages and disadvantages of spectral filtering, wavelet transform and adaptive filters. Based on the Fourier transform, (shown in Figure 6.1), these algorithms underperform when the signal is composed of multi-frequency and/or non-stationary components; Wavelet transform based denoising methods (in Figure 6.2) requires choosing an appropriate wavelet library and decomposition level, which in return requires considerable expertise and experience, and are therefore difficult to use by an average interpreter(Mert and Akan, 2014; Liu et al., 2016b).

Empirical mode decomposition (EMD) is a data-driven signal decomposition method. It analyzes non-stationary signals and adaptively decomposes the data into a suite of oscillatory components called intrinsic mode functions (IMF) and a residual (Huang et al., 1998). Recently, several researchers have applied EMD to contruct a “hybrid” denoising algorithm, which combines signal decomposition and thresholding (Bekara and van der Baan, 2009; Chkeir et al., 2010; Gan et al., 2014; Li et al., 2015). Figure 6.3 shows a typical workflow of the mode decomposition based methods. The IMFs are adaptively obtained from the input data, giving EMD-based hybrid denoising methods

some advantages over wavelet thresholding techniques, avoiding the need to select a priori an appropriate basis function. However, as it is not based on an assumption of bandlimited data, EMD suffers from mode mixing issues, especially in low SNR environments (Huang et al., 1998; Kabir and Shahnasz, 2012). To overcome this drawback, several improments to EMD have been developed, including ensemble empirical mode decomposition (EEMD) (Wu and Huang, 2009), complete ensemble empirical mode decomposition (CEEMD) (Torres et al., 2011) and improved complete ensemble empirical mode decomposition (ICEEMD) (Colominas et al., 2014). Although the mode-mixing problem is significantly reduced using the EEMD, CEEMD, and ICEEMD techniques, all these methods still extract local extrema and require interpolating the envelopes. Furthermore, the empirical nature of EMD lacks a solid mathematical foundation (Gilles, 2013; Colominas et al., 2014; Liu et al., 2016a).

To address these limitations, Dragomiretskiy and Zosso (2014) proposed a variational mode decomposition (VMD) algorithm. VMD decomposes a signal into an ensemble of band-limited IMFs. The IMFs are acquired by solving an optimization problem in the frequency domain to best isolate different spectral components. Thus, VMD has a solid mathematical foundation and is less sensitive to noise (Liu et al, 2016a). This transform has been successfully applied to ground roll attenuation (Liu et al., 2015), seismic time-frequency analysis (Liu et al., 2016a) and seismic stratigraphy analysis (Li et al., 2017).

Working on the adaptively decomposed data components, EMD-and VMD-based denoising methods require a criterion to separate noise from the signal (Li et al., 2015; Liu et al., 2016b). In general, the decomposed IMFs represent most of the signal while

the residual and some of the mode components represent the noise. Peng et al. (1994) proposed detrended fluctuation analysis (DFA) to analyze different trends of unknown duration. The scaling exponent, α, estimated from DFA is then used to evaluate the variation of the average root mean square (RMS) fluctuation around the local trend. The scaling exponent value is also an indicator of signal roughness: the larger the value, the smoother the time series or the slower the fluctuations (Horvatic et al., 2011; Berthouze and Farmer, 2012). Hu et al. (2001) and Chen et al. (2002) applied DFA to complex noisy signals exhibiting varying local characteristics and investigated the strategies for nonstationary signal analysis. I use DFA to characterize different components to adaptively separate the noise residual from the signal IMFs. In general, the seismic signal is a harmonic signal or a combination of harmonic signal components, while the noise component is random and uncorrelated with the signal component.

In this chapter, I propose an adaptive signal denosing method based on VMD and DFA. First, I introduce the basic principles of EMD methods and VMD method. Then, I compare VMD with EMD as well as its derivations, including EEMD, CEEMD, and ICEEMD using synthetic signals and field seismic traces. Next, I provide an empirical equation based on the DFA to adaptively determine the number of IMFs required for accurate signal reconstruction. Later, I use a scaling exponent obtained from the DFA as a threshold to distinguish random noise and signal between the multiple IMFs and the residual. Finally, I apply the proposed thresholded VMD denoising method to the synthetic examples and a noisy legacy 3D data volume acquired over a north Texas Mississippi Lime play.

THEORY

BRIEF REVIEW OF EMD AND ITS DERIVATIONS

To suppress the noise, one first needs to differentiate the signal from noise components in measured data, either in the original measurement domain or in an appropriate transform domain. EMD is one of the most popular signal analysis methods which adaptively decomposes a complex signal into a finite set of IMFs in the time domain (Huang et al., 1998; Han and van der Baan, 2013; Gan et al., 2014). In EMD, IMF components are the mean value of upper and lower envelopes interpolated from the local maxima and local minima of the original signal. The residual, obtained by subtracting the original measured data and the summation of the acquired IMFs, is used as input data in the next iteration. EMD will stop when the residual satisfies a certain stoping criterion. In this manner, EMD acts as a sifting process. The original signal can be reconstructed by the IMF components with the following representation:

$$s(t) = \sum_{k=1}^{K} IMF_k(t) + r_K(t), \tag{6.1}$$

where, IMF_k is the kth IMF of the data, and r_K stands for the residual trend. In EMD, low order IMFs represent faster oscillations (high-frequency modes), and high order IMFs represent slower oscillations (low-frequency modes).

EMD is a fully data-driven separation of data into fast and slow oscillation components. Although EMD has shown numerous successful applications in different fields of signal processing, the lack of a mathematically defined model and the mode-mixing problem affect its reliability (Han and van der Baan, 2013; Liu et al., 2016a).

Wu and Huang (2009) proposed a noise-assisted EEMD to overcome the mode mixing problem by injecting Gaussian white noise into the decomposition algorithm to stabilize its performance. Summing the ensemble IMFs, which are an average of all the corresponding IMFs generated from different realizations of noise-assisted EMD, does not perfectly reconstruct the original signal, although the reconstruction error decreases with the increasing number of noise realizations. Unfortunately, increasing the number of noise realizations also increase the computation expense.

The CEEMD technique is also noise-assisted, aiming at simultaneously solving the mode-mixing problem and maintaining the reconstruction performance at the same time (Torres et al., 2011). In the first iteration, CEEMD adds a fixed percentage of Gaussian white noise and obtains a unique first residual. The sifting process continues with the next modes obtained by adding the corresponding average EMD modes of white noise until a stopping criterion is reached. The recently developed ICEEMD approach helps avoid the spurious modes and reduces the amount of noise contained in the modes compared with the CEEMD approach, which grants more physical meaning to the decomposed IMFs (Colominas et al., 2014).

VARIATIONAL MODE DECOMPOSITION

VMD decomposes the input data into intrinsic modes in the frequency domain, with each IMF is compact around their respective central frequencies (Dragomiretskiy and Zosso, 2014). In VMD, the IMFs are defined as elementary amplitude/frequency modulated (AM-FM) harmonics to model the non-stationarity and the nonlinearity of the data:

$$u_k(t) = A_k(t)\cos\left[\phi_k(t)\right], \tag{6.2}$$

where the phase $\phi_k(t)$ is a non-decreasing function, $\phi_k'(t) \geq 0$, and the envelope is non-negative, $A_k(t) \geq 0$. Both the envelope $A_k(t)$ and the instantaneous frequency $\omega_k(t) = \phi_k'(t)$ vary slower than the phase $\phi_k(t)$ (Gilles, 2013). In other words, on a sufficiently long interval, the mode $u_k(t)$ can be considered to be a pure harmonic signal (Dragomiretskiy and Zosso, 2014). In contrast, noise is assumed to be additive Gaussian random noise. The IMFs are extracted by solving the following optimization problem:

$$\begin{aligned} &\min_{\{u_k,\ \omega_k\}} \left\{ \sum_k \left\| \partial_t \left[\left(\delta(t) + \frac{j}{\pi t} \right) * u_k(t) \right] e^{-j\omega_k t} \right\|_2^2 \right\}, \\ &s.\ t. \quad \sum_k u_k = d(t) \end{aligned} \tag{6.3}$$

where u_k and ω_k are modes and their central frequencies, respectively, $\delta(\bullet)$ is a Dirac impulse. $s(t)$ are the data to be decomposed, with the constraint that the summation over all modes should be the input signal.

To solve the optimization problem in Equation 6.3, the alternate direction method of multipliers (ADMMs) (Hestenes, 1969) is employed to estimate IMFs (modes) in the frequency domain:

$$\hat{u}_k^{n+1}(\omega) = \frac{\hat{d}(\omega) - \sum_{i=1}^{k-1} \hat{u}_i^{n+1}(\omega) - \sum_{i=k+1}^{K} \hat{u}_i^{n}(\omega) + \frac{\hat{\lambda}^n(\omega)}{2}}{1 + 2\beta\left(\omega - \omega_k^n\right)^2}, \tag{6.4}$$

where, $\hat{d}(\omega)$, $\hat{u}_i(\omega)$ and $\hat{\lambda}(\omega)$ are the Fourier transform of $d(t)$, $u_i(t)$ and $\lambda(t)$, respectively, and *n* denotes the iteration number, and λ denotes the Lagrangian multiplier for rendering the problem unconstrained, while β represents the balancing parameter of

the data-fidelity constraint. In VMD, low order IMFs represent slower oscillations (low-frequency modes), and high order IMFs represent faster oscillations (high-frequency modes).

CHARACTERIZING SEISMIC SIGNAL USING VMD

Since the noise components are not harmonic, the mode decomposition methods can be used to distinguish signal and noise.

The seismic signal of a linear event can be expressed as a plane wave (Schuster, 2007):

$$d(t,x) = w\left(t - \frac{x}{c}\right), \tag{6.5}$$

where (x, t) are the coordinates of offset and time, w is the waveform (such as a Ricker wavelet), and c is the wave propagation velocity.

The f-x spectrum can be obtained by applying a Fourier transform along the t axis:

$$D(f,x) = W(f)\mathbf{exp}\left(j\frac{2\pi fx}{c}\right), \tag{6.6}$$

where f is the frequency, and $W(f)$ is the Fourier transform of $w(t)$.

For the discrete situation, if one assumes the sampling interval along x axis to be Δx, then

$$D_f(m) \equiv D(m\Delta x, f), \qquad m = 1,2,\ldots,M, \tag{6.7}$$

where m is the trace number, and M is the total number of traces.

In addition, there is an exponential relationship between two adjacent traces:

$$D_f(m) = D_f(m-1)e^{i\frac{2\pi f \Delta x}{c}}. \quad (6.8)$$

From Equation 6.8, I know the frequency slice D_f includes one complex harmonic in the *f-x* domain. Bekara and van der Baan (2009) concluded that the superposition of p linear events in the *t-x* domain is equivalent to the superposition of p complex harmonics in the *f-x* domain. According to the definition of IMF in Equation 6.2 and the series theory, it is valid to decompose seismic data into IMFs. Since the seismic signal can be expressed as the combination of different IMFs, the residual will be interpreted as noise.

THRESHOLDED DENOISING METHOD

Previous sections suggest that signal decomposition is a straightforward way to express a singal in terms of different components. One can also use the noise thresholding estimator to determine which components are noise and which are signal (Fang et al., 2011; Gan et al., 2014; Mert and Akan, 2014). Peng et al. (1994) proposed DFA to estimate the data non-stationary properties based on scaling exponent. Because it obtains reliable estimators for signals with different trends and unknown duration (Horvatic et al., 2011), DFA is a good candidate for non-stationary signal analysis.

The DFA method is implemented in the following steps:

(1) $y(k)$ is the cumulative sume of a series $x(i)$, which has the mean value removed:

$$y(k) = \sum_{i=1}^{k}\left[x(i) - \bar{x}\right], \quad 1 \le k \le N, \quad (6.9)$$

where $\bar{x}$ is the average of the time series in the range [1, N]， and N is the total number of samples.

(2) The integrated series $y(k)$ is then divided into $N_n = [N/n]$ non-overlapping segments of length *n*, called window size. For each window the local $y_n(k)$ is calculated by a polynomial fitting, which in this study is of order 2.

(3) The RMS fluctuation $F(n)$ is expressed as:

$$F(n) = \sqrt{\frac{1}{N}\sum_{k=1}^{N}\left[y(k) - y_n(k)\right]^2} \quad . \tag{6.10}$$

It is apparent that the fluctuation will increase with increasing segment duration *n* (Peng et al., 1994; Hu et al., 2001).

(4) If the data are long-range power-law correlated, the fluctuation increases following a power law:

$$F(n) \propto n^{\alpha} . \tag{6.11}$$

The scaling exponent α is defined as the slope of the curve $\log\left[F(n)\right]/\log(n)$, which is estimated in a similar way with the Hurst exponent in log-log scale (Mert and Akan, 2014). The special case, α =0.5, corresponds to uncorrelated white noise. When 0 < α < 0.5, the signal is called “anti-correlated” such that large fluctuations are followed by small ones and vice versa (Hu et al., 2001; Chen et al., 2002). When 0.5 < α < 1.0, temporal correlations are possible(Mert and Akan, 2014). Using DFA, I determine which IMF is signal and which level exhibits noise. In signal mode decomposition analysis, the decomposition stops at this point with most of the incoherent noise components remaining in the residuals (Li et al., 2015).

SYNTHETIC EXAMPLES

First, I apply EMD, EEMD, CEEMD, ICEEMD and VMD to decompose a noise-free artificial mixed signal, containing a lower background frequency (s_1) and a gapped higher 51Hz frequency (s_2). The analyzed signal is $d = s_1 + s_2$ with

$$s_1 = \sin(13t) \quad if \quad 1 \le t \le 1000ms$$
$$s_2 = \begin{cases} \sin[51(t-300)] & if \quad 300 \le t \le 700ms \\ 0 & t < 300ms \quad t > 700ms \end{cases}, \tag{6.12}$$

Full decompositions of signal *d* for EMD and its noise-assisted derivations are presented in Figure 6.4. EMD presents strong mode mixing. Note that when mode mixing occurs in one mode, the entire subsequent decomposition process will be affected. For EEMD, IMF 3 as well as the following IMFs have little energy. For CEEMD, IMF 4 and onwards do not represent relevant information of the signal, and have little energy. The redundant IMFs or modes in EEMD and CEEMD appear because different realizations of signal plus noise have produced a different number of IMFs. Notice, CEEMD also produces a spurious IMF2. The ICEEMD nicely recovers the two components of the original signal. The VMD also accurately decomposes the two components. Because ICEEMD performs the best among the alternative EMD derivations, I only compare ICEEMD and VMD in the following sections.

Second, I design noisy signal decomposition experiments based on the previous artificial mixed signal in Figure 6.4. In Figure 6.5, 10 dB noise has added. Because of the noise assisted sifting process, ICEEMD produces some redundant IMFs. Compared to VMD, which was constructed with only two components, the number of IMFs from ICEEMD changes from 2 to 7, and IMF1 as well as IMF2 becomes different with noise in the modes from those in Figure 6.4. Note that the noises included in IMFs from VMD

are much less than those obtained from ICEEMD. It is clear that VMD is a more robust signal mode decomposition method compared with ICEEMD, which is the best method among EMD derivations.

Next, in Figures 6.6 and 6.7, I use a field seismic trace with additive synthetic noise to validate that seismic data can be decomposed using IMFs from VMD. Figure 6.6a shows the measured seismic trace. Figures 6.6b-6.6d show the IMF1, IMF2, and IMF3, respectively. Figure 6.6e displays the reconstructed signal from IMF 1-3. To test the VMD algorithm on a noisy signal, I add 10dB band-limited Gaussian noise to the signal (Figure 6.6a). Figures 6.7b-6.7d display the decomposed IMFs of the noisy signal, which are harmonic. Figure 6.7e shows the residual, which contains the noise component. Figure 6.7f shows the reconstructed signal, which is very close to the original signal in Figure 6.6a.

HYBRID SIGNAL DENOISING WORKFLOW

As discussed above, a typical signal mode decomposition based denoising workflow is shown in Figure 6.3. I decompose noisy data with EMD and its derivations and VMD and reconstruct the denoised signal by ignoring the residual/last mode components. Since I have observed that VMD shows better performances in signal decomposition in both noise-free and noisy situations compared with EMD based methods, I investigate a thresholded VMD denoising method. In the following examples, I use the corresponding ICEEMD based results for comparison.

To make the proposed method adaptive, I need to determine the optimal VMD parameters in a data-driven way. In the VMD approach, β and K are the two most important parameters in Equations (6.3) and (6.4). The β controls data fidelity, which

could compromise the signal preservation of the decomposed IMFs if not well defined. In practice, the β value can be obtained by several trials.

In addition, some researchers use the number of IMFs from EMD to be the K for VMD (Liu et al., 2016b). However, Figures 6.4 and 6.5 demonstrate that the IMF number of VMD could be very different from that of EMD. A larger value of parameter *K* possibly results in mode mixing, whereas a lower value greatly affects capturing the correct center frequencies of different modes (Liu et al., 2016a). Inspired by the empirical equation for wavelet based denoising methods (Mert and Akan, 2014), I propose an empirical equation to determine the optimal *K* (number of VMD outputs of a seismic signal decomposition):

$$K = \min\left\{ n \in Z^{+} \mid n \geq 2\alpha \ln\left(N\right) \right\} , \tag{6.13}$$

where α is the scaling exponent from DFA of the signal.

To validate Equation 6.13, I apply VMD to the nonstationary seismic trace shown in Figure 6.6a. According to Equation 6.13, K = 6 in this case. Figure 6.8 shows the variation of α values with different IMF numbers, and the values are listed in Table 6.1. The first IMFs with larger scaling exponent values contain the signal information, while the last IMFs with smaller scaling exponent values carry irrelevant noise components. As mentioned above, if the *K* is small, for example 3, 4 and 5 in Figure 6.8a, the IMFs contain both signal and noise components, so the scaling exponent values are larger than 0.1. Whereas, when the *K* is large, for example 9 and 10 in Figure 6.8c, mode mixing occurs, which causes the scaling exponent values to not decrease with the IMF number, and it is more obvious when *K* equals 10. Figure 6.8b shows the scaling exponent plots of *K* equals 6, 7 and 8, where the α values of the last IMFs are always smaller than 0.1. Based on

these observations, I suggest adopting K equals 6, 7 or 8 to distinguish noise from signal. Therefore, in this application, 6 is an appropriate number of VMD outputs.

Figure 6.9 illustrates the proposed denoising workflow. I use VMD to decompose the signal, and DFA to determine the number of IMFs from VMD, as well as the threshold for every IMF in the reconstruction process. In the end, the filtered signal is obtained by summing the first several IMFs with larger α values.

FIELD APPLICATIONS

First in this section, I show a 1D field seismic trace denoising example. The testing signal is the same seismic trace from Figure 6.6a. I consider different SNR situations and test VMD and ICEEMD based approaches in 10 dB, 3 dB, 0 dB and -3 dB. Figures 6.10 and 6.11 show the results from ICEEMD and VMD, respectively. I carry out 100 times random experiments.

To numerically evaluate the filtering results, I measure the differences between the original signal and the filtered results from ICEEMD and VMD by means of mean squared error (MSE), mean absolute error (MAE), SNR and peak signal to noise ratio (PSNR).

MSE can be estimated by

$$\mathrm{MSE} = \frac{1}{N}\sum_{n=1}^{N}\left[d(t)-\hat{s}(t)\right]^2, \tag{6.14}$$

where N is the number of samples, $d(t)$ is the original signal, and $\hat{s}(t)$ is filtered results.

MAE is given by

$$\mathrm{MAE} = \frac{1}{N}\sum_{n=1}^{N}\left|d(t)-\hat{s}(t)\right|. \tag{6.15}$$

SNR is defined as the ratio of the power of the signal and the power of noise:

$$\mathrm{SNR} = \frac{P_{d(t)}}{P_{\hat{n}(t)}} = \left(\frac{A_{d(t)}}{A_{\hat{n}(t)}} \right)^2, \tag{6.16}$$

where $\hat{n}(t)$ is the filtered noise defined as

$$\hat{n}(t) = s(t) + n(t) - \hat{s}(t), \tag{6.17}$$

where $n(t)$ is the additive noise.

The definition of PSNR is

$$\mathrm{PSNR} = \frac{\max\left(s^2(t)\right)}{\mathrm{MSE}}. \tag{6.18}$$

Table 6.2 shows statistical comparison of the denoised results between ICEEMD and VMD based methods in terms of MSE, MAE, SNR and PSNR. Both methods can filter out noise and enhance the data quality, while the VMD based method outperforms for each measure. In addition, I evaluate the computation cost of ICEEMD and VMD for the synthetic signal and field trace. To further assess their performances, I also record the computational time of the two methods for the synthetic example in Figure 6.4 and field seismic trace example in Figure 6.6a, which is listed in Table 6.3. It can be seen that VMD is faster than the ICEEMD, which is very appealing for practical applications. All experiments are done on a PC station equipped with an Intel Core CPU clocked at 2.20 GHz and 8 GB RAM.

In the end, I apply the proposed method on a low-fold (The fold number for most of the CMPs is 15), noisy seismic survey acquired over North Central Texas, USA. The target formation is the high porosity Mississippian Chert (Verma et al., 2016). The originally acquired seismic data were contaminated with highly aliased ground roll.

Figures 6.12a and 6.13a show two vertical seismic sections after ground roll suppression by Verma et al. (2016), whose location is highlighted by dashed lines AA' and BB' in Figure 6.14a. Although a significant amount of ground roll was suppressed in this process, this low-fold seismic data are still contaminated with some residual ground roll, along with other noises. Figures 6.12b and 6.12c show the filtered result and rejected noise from a bandpass filter (0-10-60-70 Hz), Figures 6.12d and 6.12e show the filtered result and rejected noise from ICEEMD, while Figures 6.10f and 6.10g show the filtered result and rejected noise from VMD, respectively. The bandpass filter can filter out the noise within a specific band, or keep the signal within a given band, but it is not suitable for complicated seismic data. The ICEEMD can remove the random noise but VMD has better results with more continuouse events. Figure 6.13 has more dips, but VMD has better performance.

Figure 6.14a shows the representative amplitude time slices through the target formation, Figures 6.14b and 6.14c display the filtered results from ICEEMD and VMD, respectively. The VMD based method suppresses the noise and keeps the reflections. In addition, compared with the ICEEMD based method, the reflections are more continuous, with more migration artifacts have been removed by the proposed method. Finally, I calculate the coherence attributes from the original seismic data (Figure 6.15a), ICEEMD filtered result (Figure 6.15b) and VMD filtered result (Figure 6.15c). Note that the discontinuities in Figure 6.15c are clearer and more continuous than those shown in Figures 6.15a and 6.15b, so the noise and artifacts have been suppressed and geologic edges are enhanced.

CONCLUSIONS

I propose a DFA thresholded VMD based hybrid denoising method. A few IMFs of a noisy signal may be components of the noiseless signal, and the residuals belong to the noise. I adopt DFA as a metric to determine which IMFs are noisy oscillations and should be excluded in the reconstruction process, while other IMFs are utilized to reconstruct the signal. Compared with EMD, EEMD, CEEMD, and ICEEMD, VMD demonstrates its advantage on robustness, stability and computational efficiency. Synthetics and field examples show that the denoising performance of the proposed method is promising and appealing.

CHAPTER 6 TABLES

	IMF1	IMF2	IMF3	IMF4	IMF5	IMF6	IMF7	IMF8	IMF9	IMF10
3	0.585393	0.543584	0.246131	N/A	N/A	N/A	N/A	N/A	N/A	N/A
4	0.589725	0.550062	0.2218	0.13916	N/A	N/A	N/A	N/A	N/A	N/A
5	0.594477	0.533924	0.400774	0.271459	0.153827	N/A	N/A	N/A	N/A	N/A
6	0.596208	0.533465	0.402735	0.272168	0.150676	0.07497	N/A	N/A	N/A	N/A
7	0.599355	0.531316	0.413215	0.264233	0.155463	0.126394	0.068536	N/A	N/A	N/A
8	0.654647	0.542995	0.511074	0.322758	0.272833	0.172611	0.137281	0.078486	N/A	N/A
9	0.655028	0.542467	0.511613	0.323984	0.271989	0.160099	0.122185	0.163124	0.016255	N/A
10	0.808021	0.599917	0.251621	0.500771	0.314992	0.269573	0.151582	0.124273	0.168361	0.020371

Table 6.1. Scaling exponent table for different IMFs when the VMD output number changes.

Methods	SNR = 10 dB				SNR = 3 dB			
	MSE	MAE	SNR	PSNR	MSE	MAE	SNR	PSNR
ICEEMD	57.2894	5.9643	12.3697	18.6933	167.1248	10.2940	7.5104	15.4616
VMD	40.5518	4.9971	13.7824	21.7061	102.9655	8.2835	9.7253	17.6189
Methods	SNR = 0 dB				SNR = -3 dB			
	MSE	MAE	SNR	PSNR	MSE	MAE	SNR	PSNR
ICEEMD	257.3871	12.7715	5.6837	13.6074	603.2600	19.5069	1.9789	9.9026
VMD	170.2557	10.4972	7.4521	15.3758	376.3135	15.2072	3.9719	11.9206

Table 6.2. Comparison between ICEEMD and VMD based denoising methods in terms of mean squared error (MSE), mean absolute value (MAE), signal to noise ratio (SNR) and peak signal to noise ratio (PSNR) of 100 times random experiments at different SNR situations.

Methods	Synthetic example	Field seismic trace
ICEEMD	3.64 s	1.92 s
VMD	0.12 s	0.29 s

Table 6.3. Computational costs of the ICEEMD and VMD methods for the examples shown.

CHAPTER 6 FIGURES

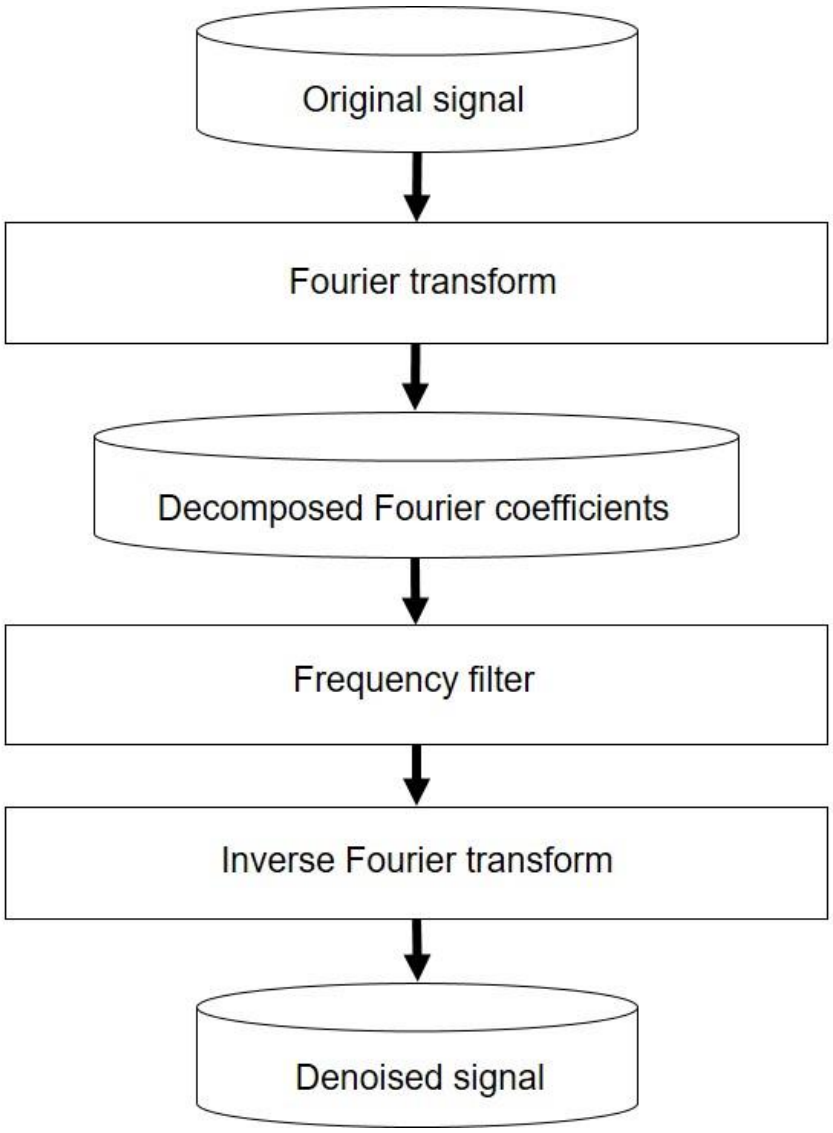

Figure 6.1. Workflow of Fourier filtering method. The frequency filter determines whether to keep or mute the certain Fouier coefficients.

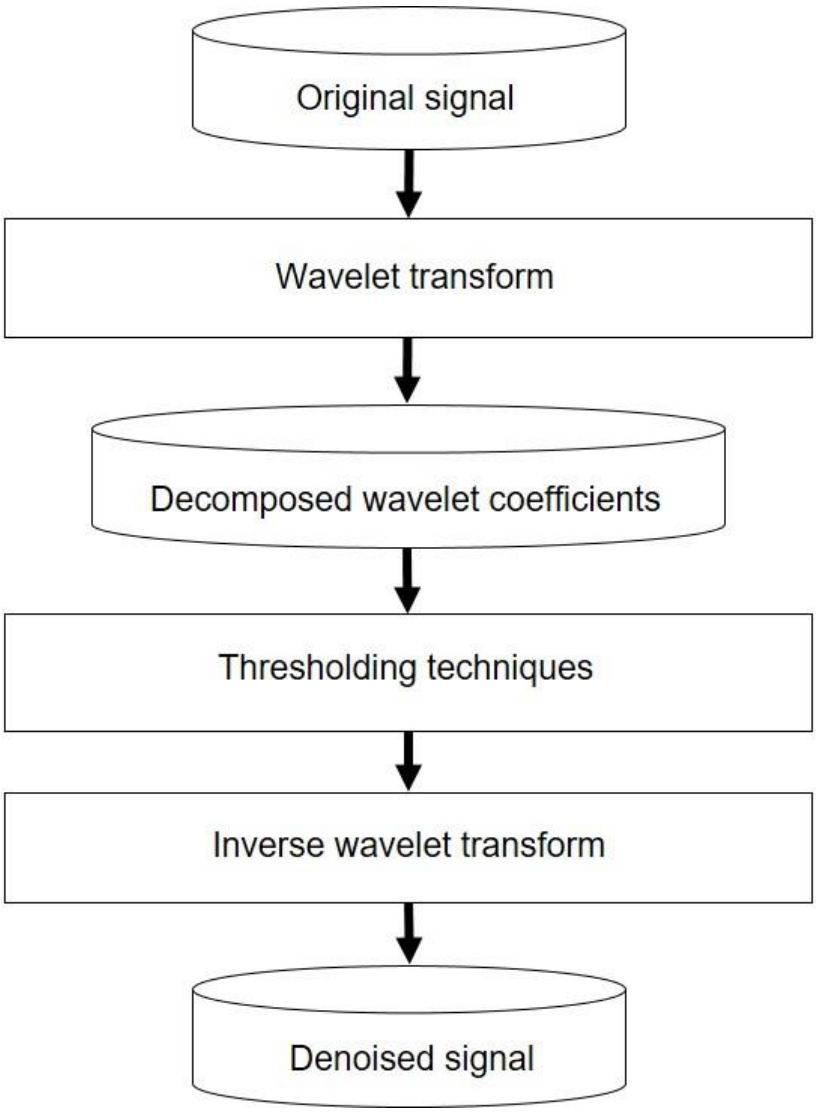

Figure 6.2. Workflow of wavelet transform based filtering methods, which involves the thresholding rules applied to wavelet coefficients, and the inverse wavelet transform reconstruction. It shows straightforward like the Fourier filtering in Figure 6.1, however, the wavelet denoising efficiency depends on the choice of the mother wavelet, the level of decomposition, and the threshold methods.

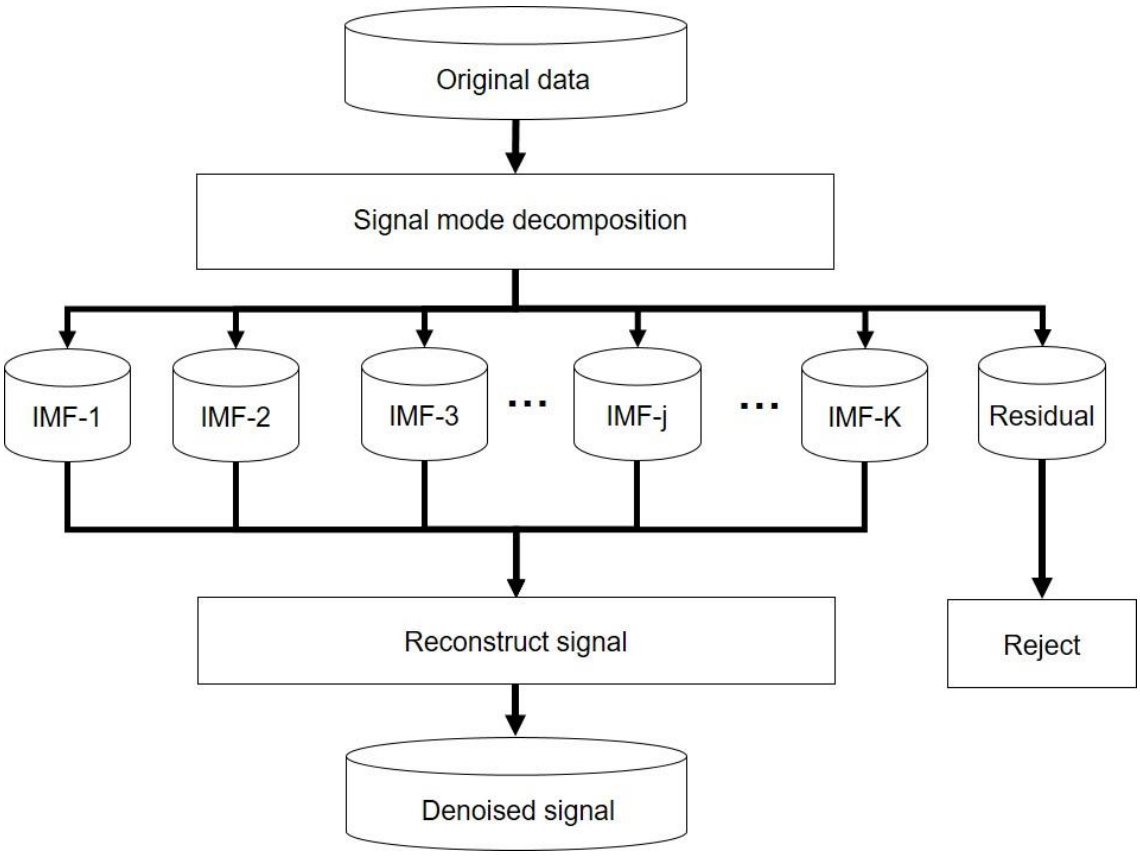

Figure 6.3. Typical signal denoising workflow using signal mode decomposition methods, such as EMD and its deriviations as well as VMD.

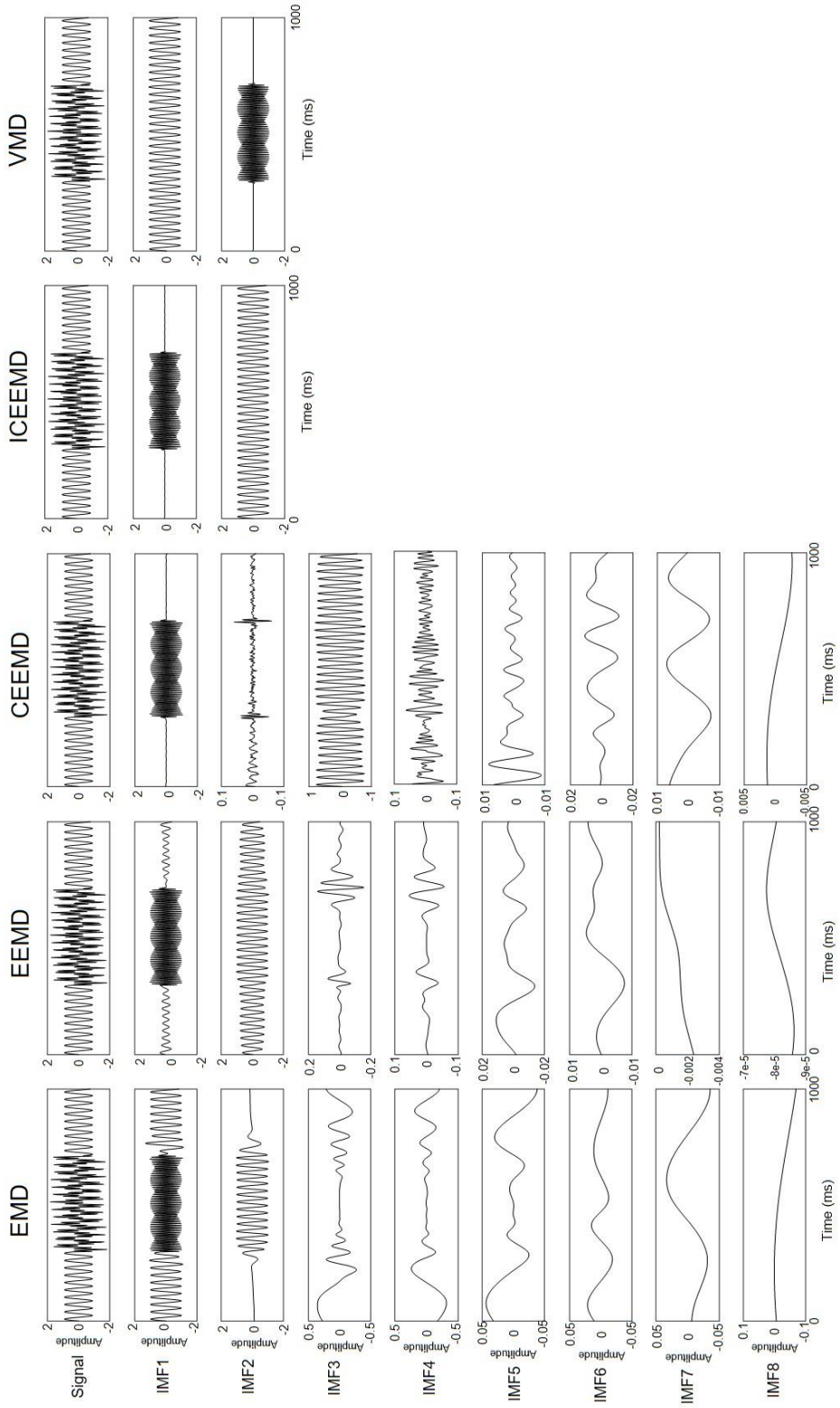

Figure 6.4. Decomposition of the artificially mixed signal by EMD, EEMD, CEEMD, ICEEMD and VMD.

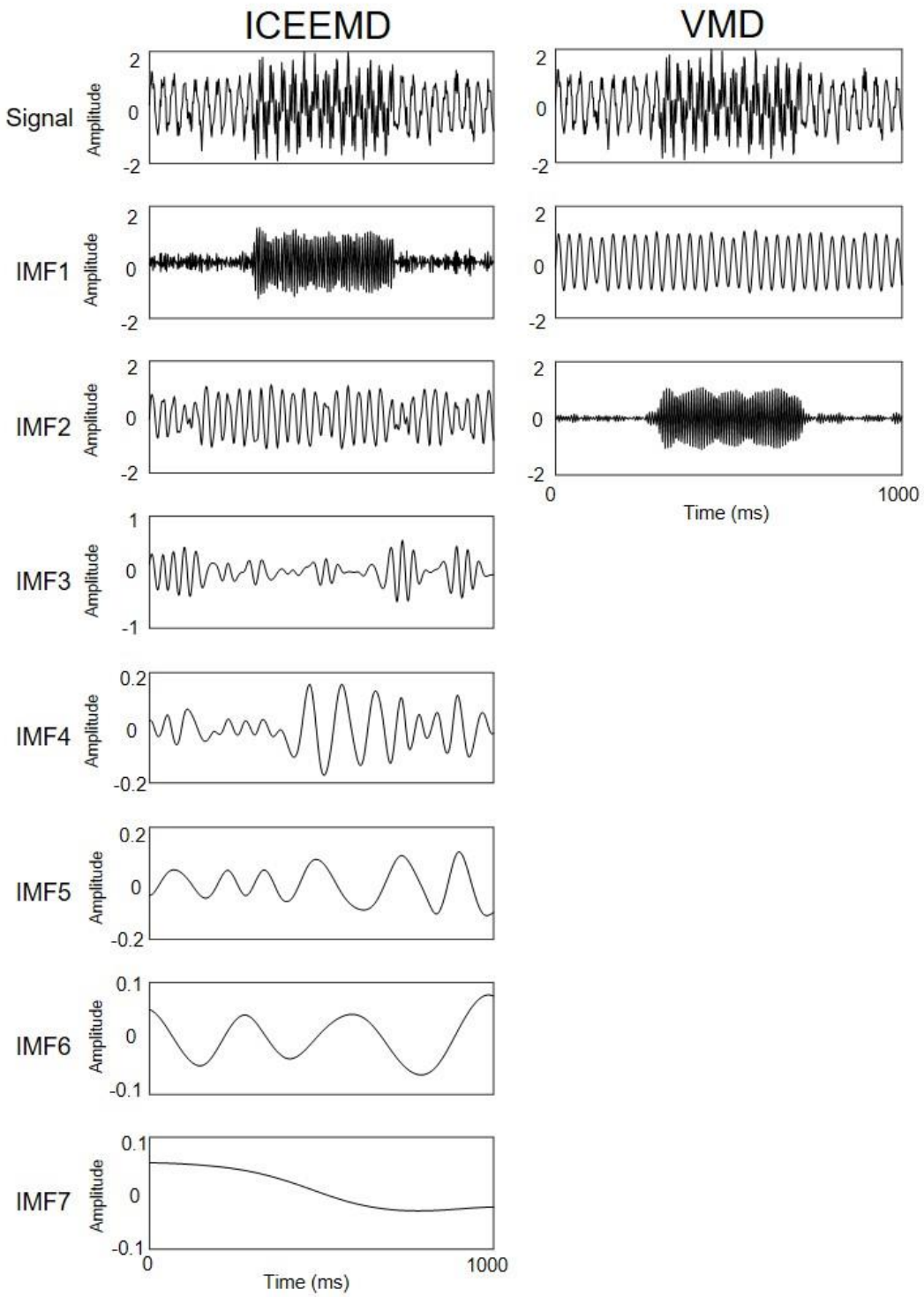

Figure 6.5. Decomposition of the artificially mixed signal with 10 dB additive noise by ICEEMD and VMD.

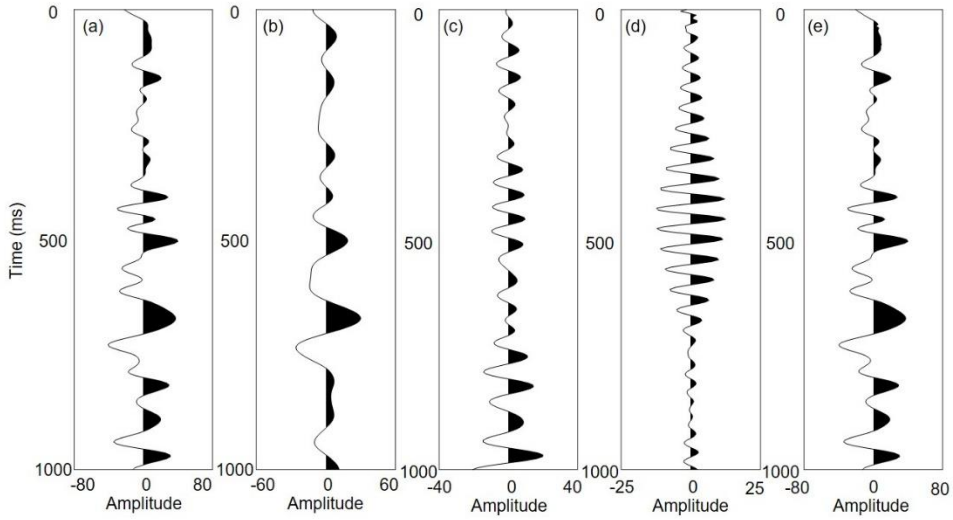

Figure 6.6. Seismic trace (a) and IMFs from VMD (b-d). The reconstructed signal is shown in (e).

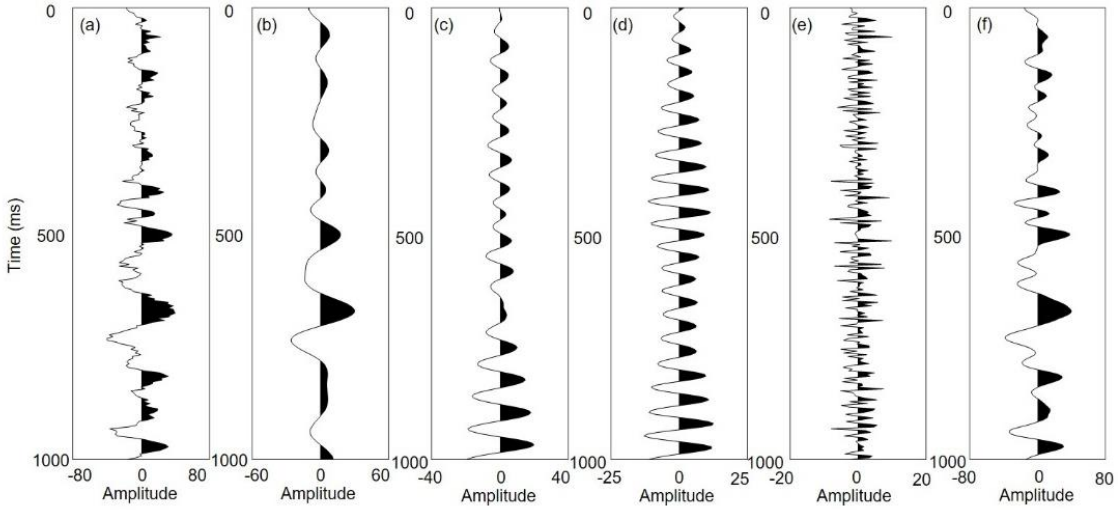

Figure 6.7. Noisy seismic trace with 10dB additive Gaussian noise (a) and IMFs from VMD (b-d). The residual between the noisy signal and summation of IMFs is displayed in (e). The reconstructed signal is shown in (f).

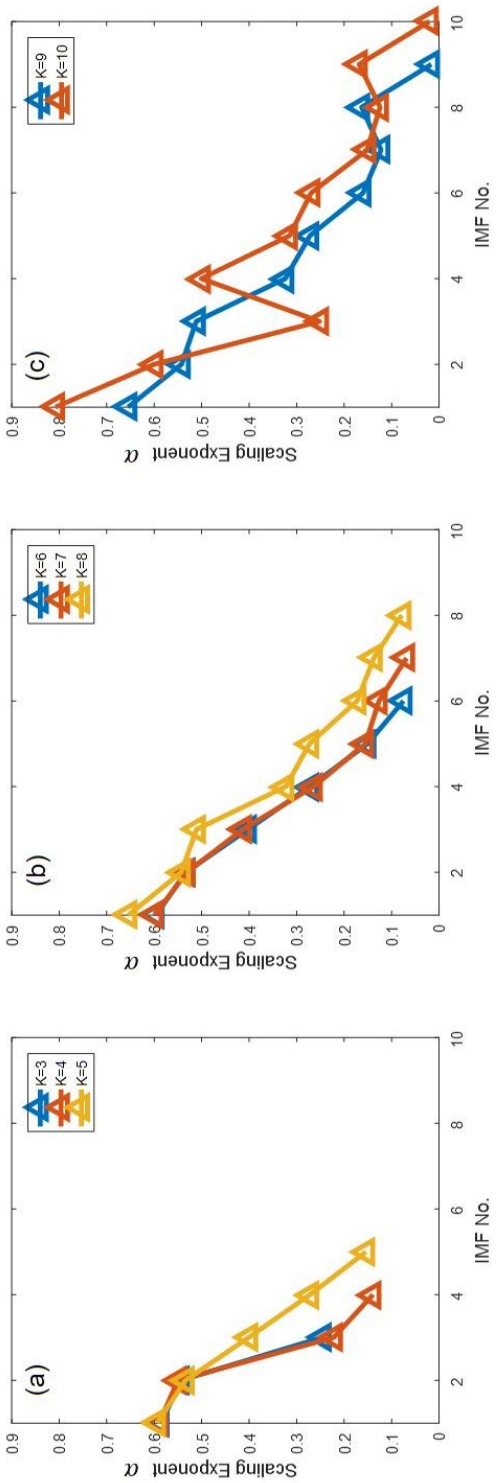

Figure 6.8. Scaling exponents α , defined in Equation 6.11 on different IMFs, as a function of the number VMD components used.

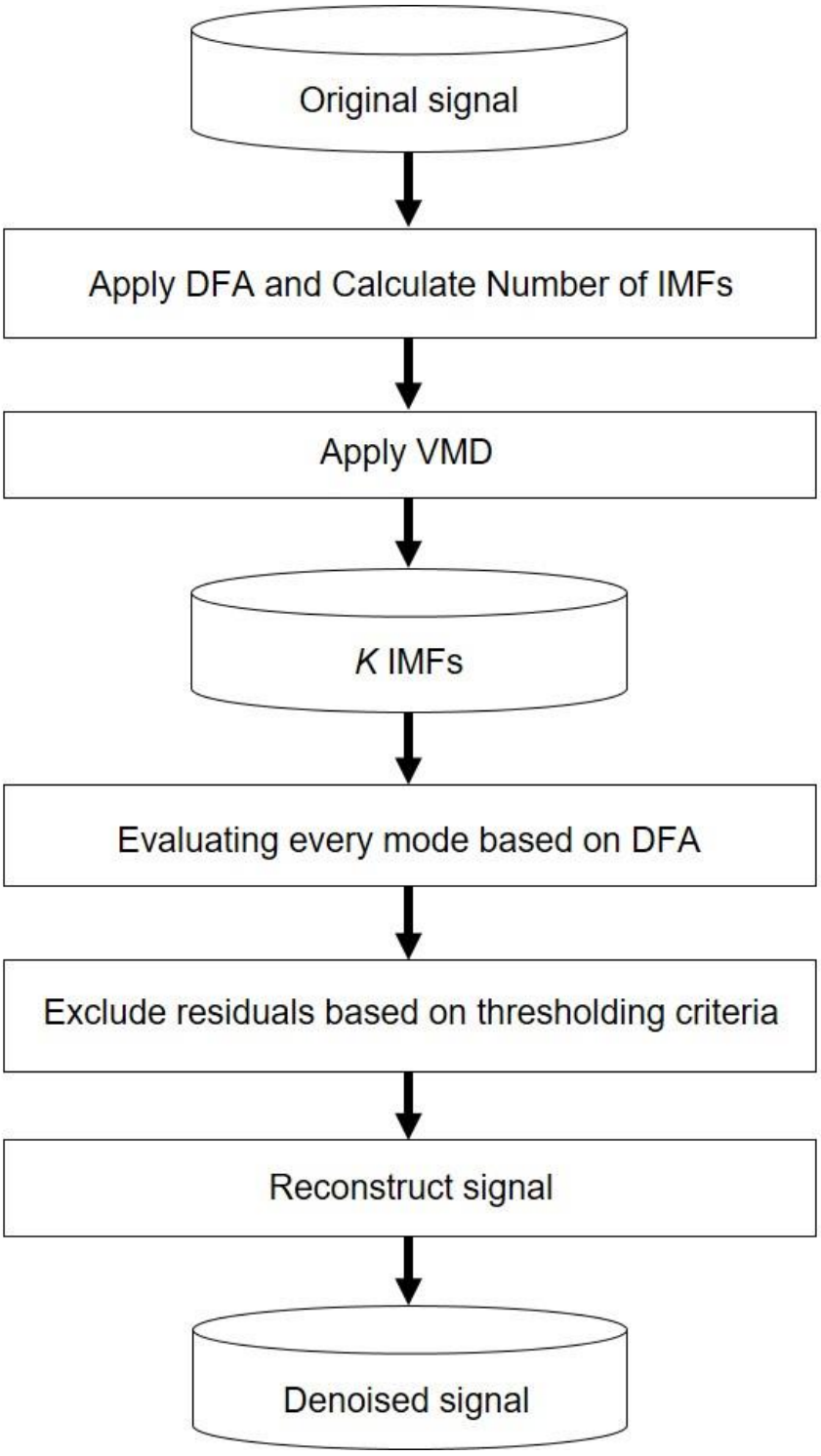

Figure 6.9. Workflow of the proposed thresholded VMD denoising method.

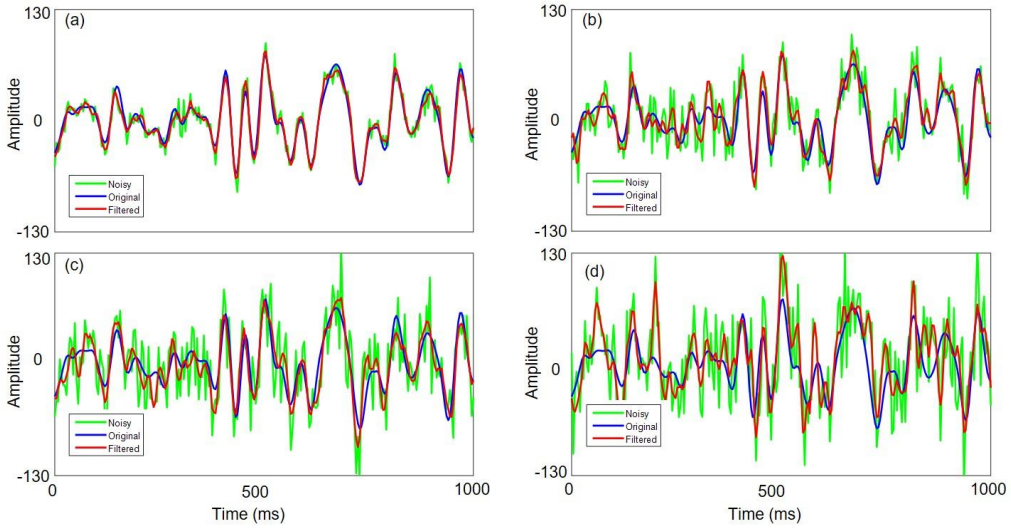

Figure 6.10. ICEEMD based denoising method on the real seismic signal in Figure 6.6a at different SNRs: (a) 10 dB, (b) 3 dB, (c) 0 dB and (d) -3 dB.

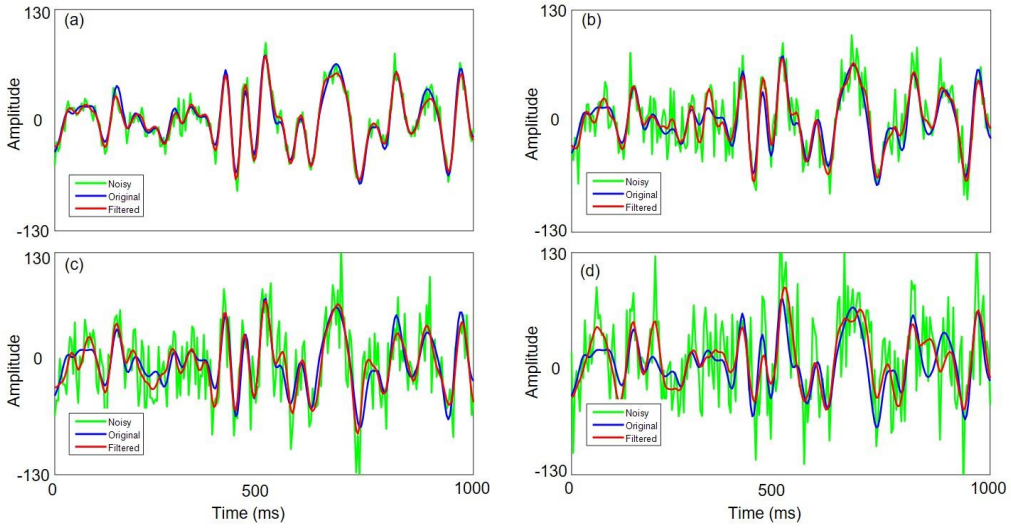

Figure 6.11. VMD based denoising method on the real seismic signal in Figure 6.6a at different SNRs: (a) 10 dB, (b) 3 dB, (c) 0 dB and (d) -3 dB.

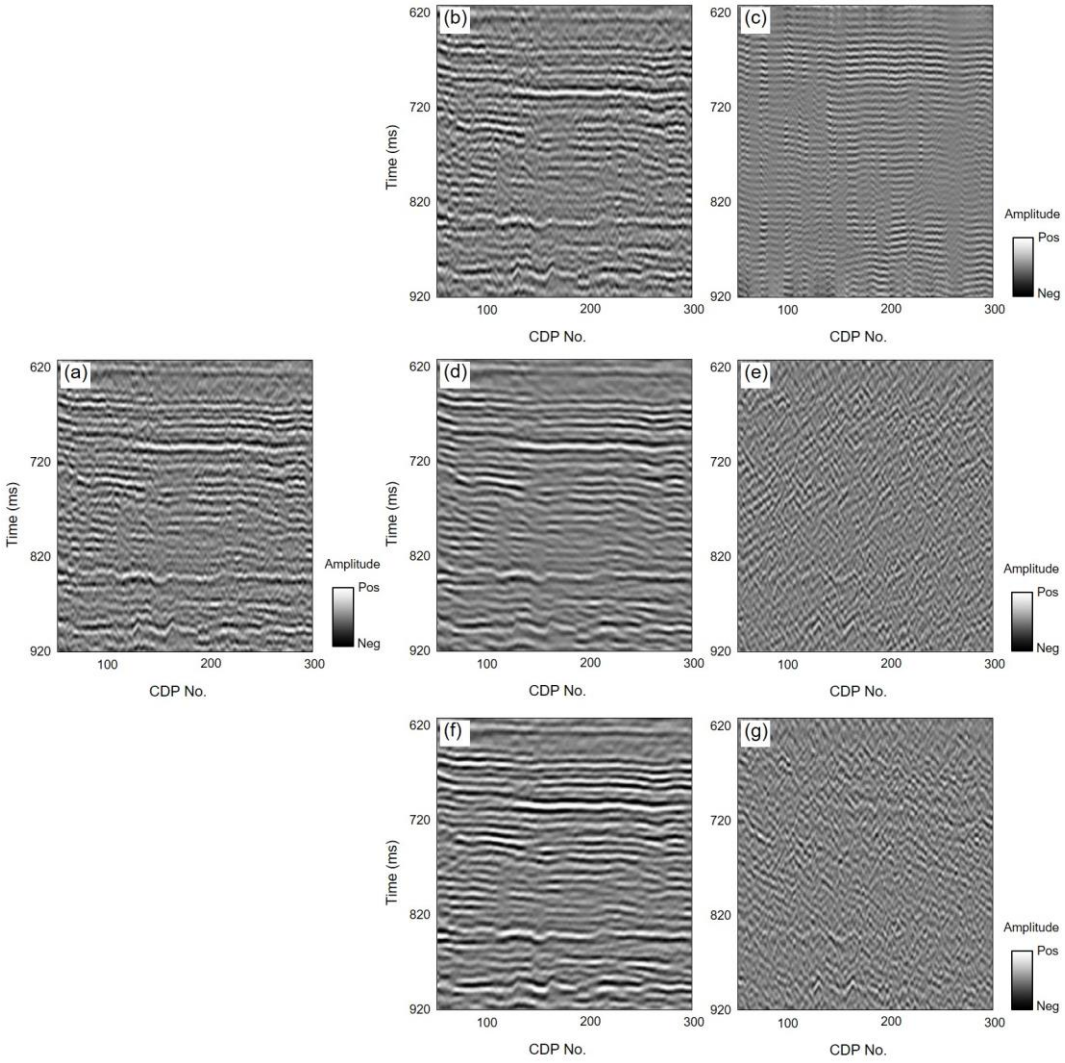

Figure 6.12. Vertical sections along AA' line through (a) noisy seismic data, (b) filtered result from a bandpass filter (0-10-60-70 Hz) and (c) difference between (a) and (b). (d) Filtered result from ICEEMD and (e) difference between (a) and (d). (f) Filtered result from VMD and (g) difference between (a) and (f). Location of line AA' shown in Figure 6.14. (Data coustesy of Eagle Energy).

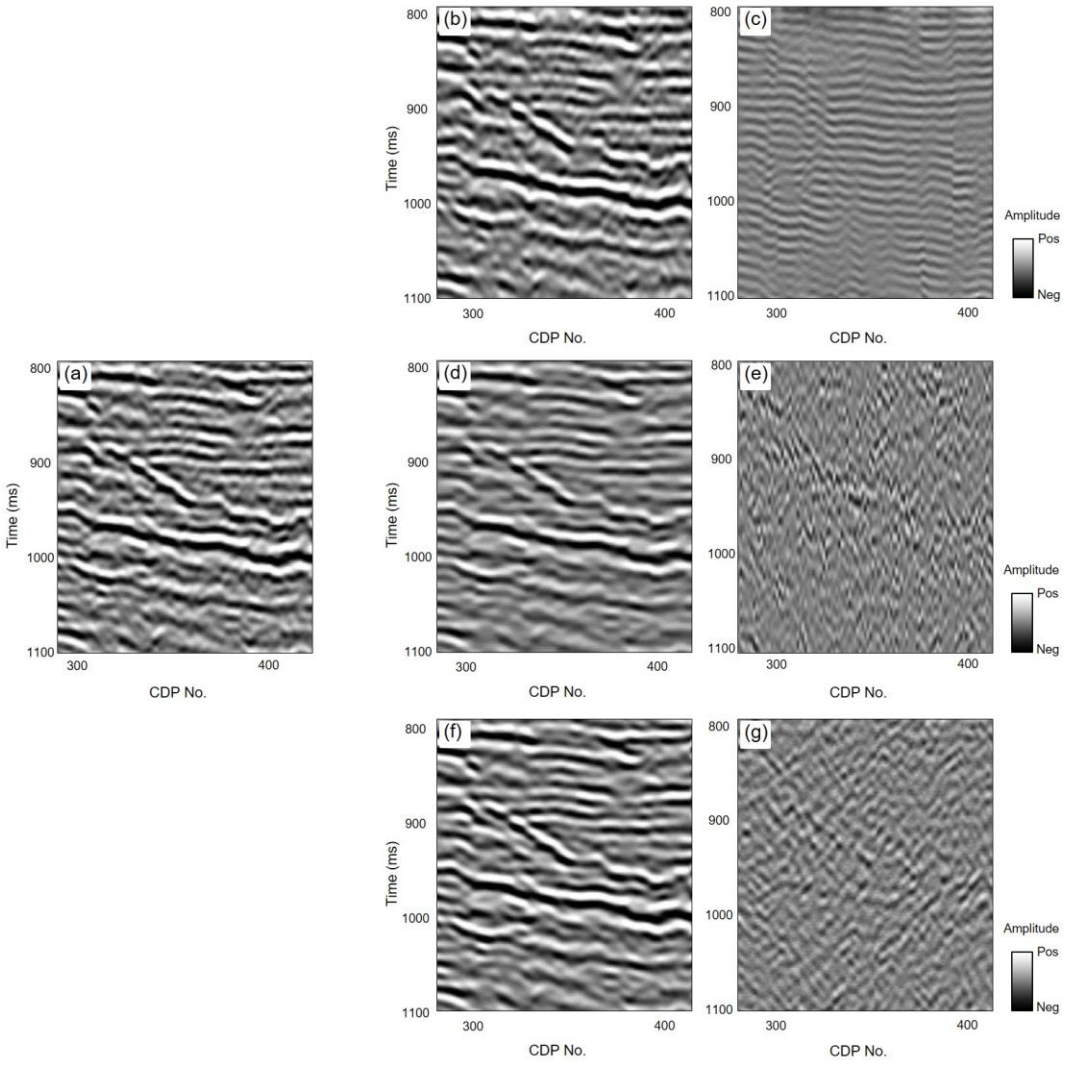

Figure 6.13. Vertical sections along as BB' line through (a) noisy seismic data, (b) filtered result from a bandpass filter (0-10-60-70 Hz) and (c) difference between (a) and (b). (d) Filtered result from ICEEMD and (e) difference between (a) and (d). (f) Filtered result from VMD and (g) difference between (a) and (f). Location of line BB' shown in Figure 6.14. (Data coustesy of Eagle Energy).

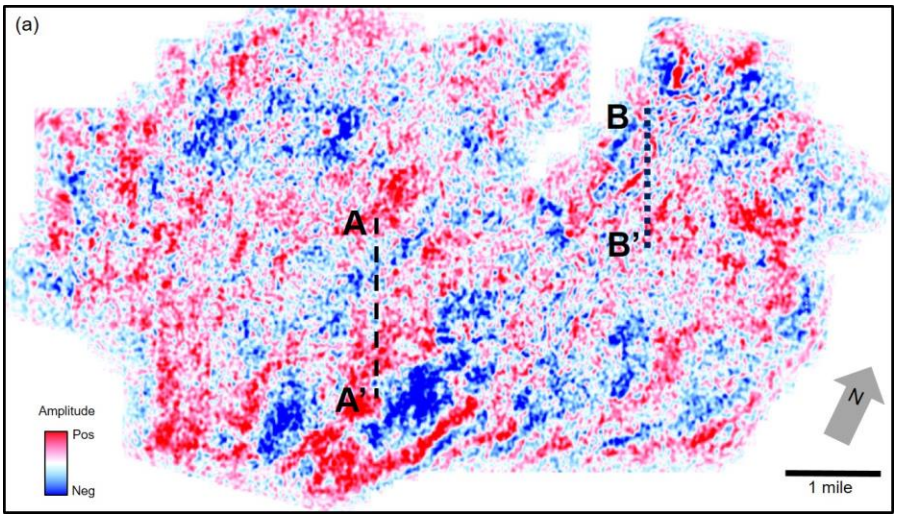

Figure 6.14a

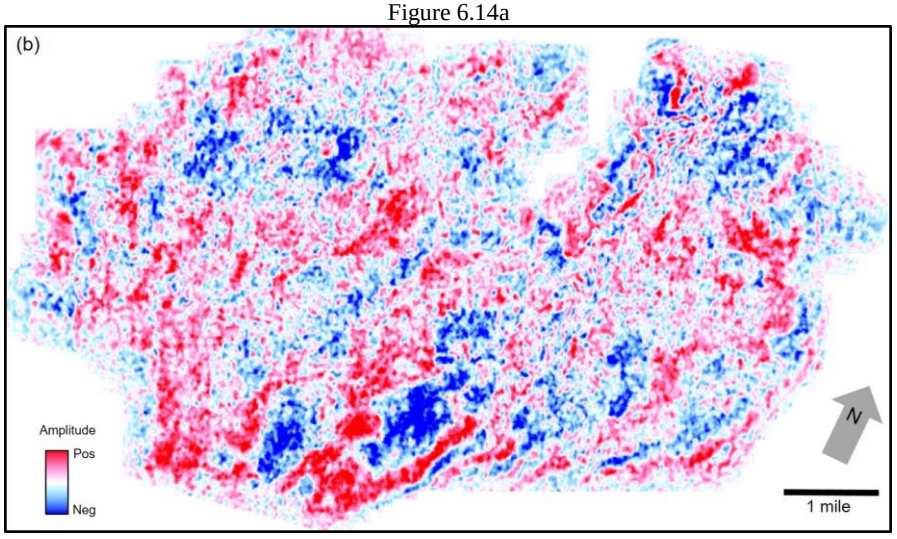

Figure 6.14b

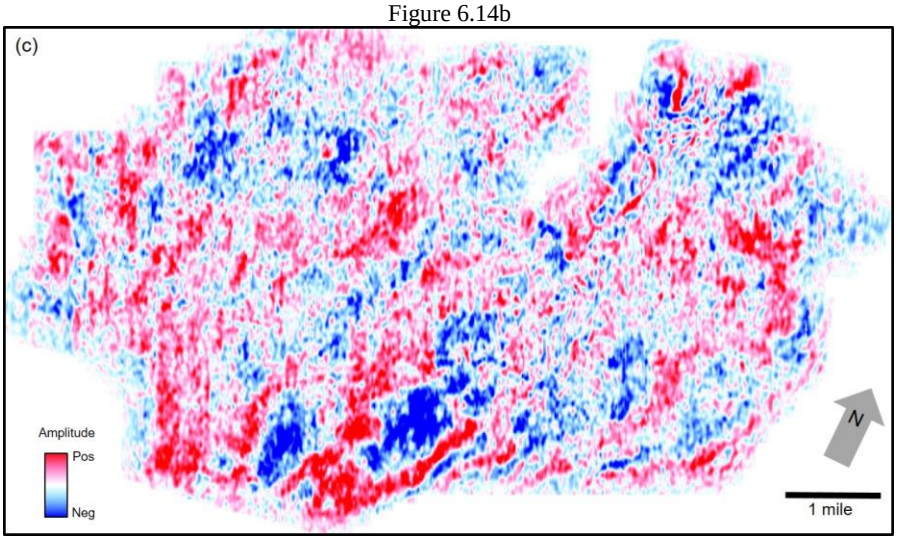

Figure 6.14c

Figure 6.14. Time slices at t=820 ms at the top Mississipi Lime interval through (a) original seismic amplitude data and filtered results using (b) ICEEMD and (c) VMD.

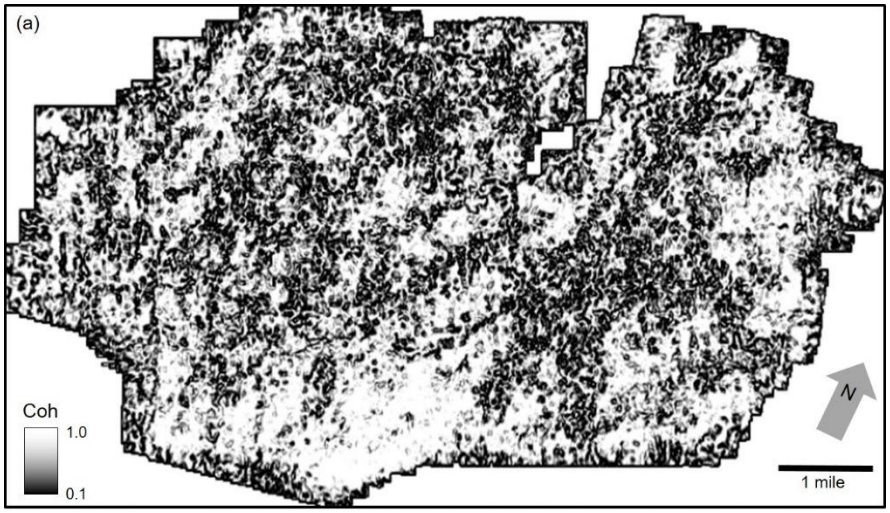

Figure 6.15a

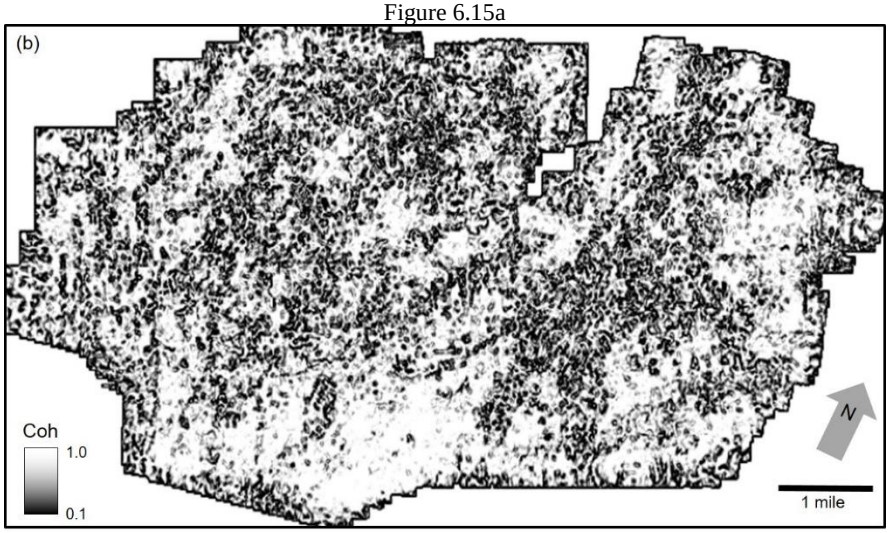

Figure 6.15b

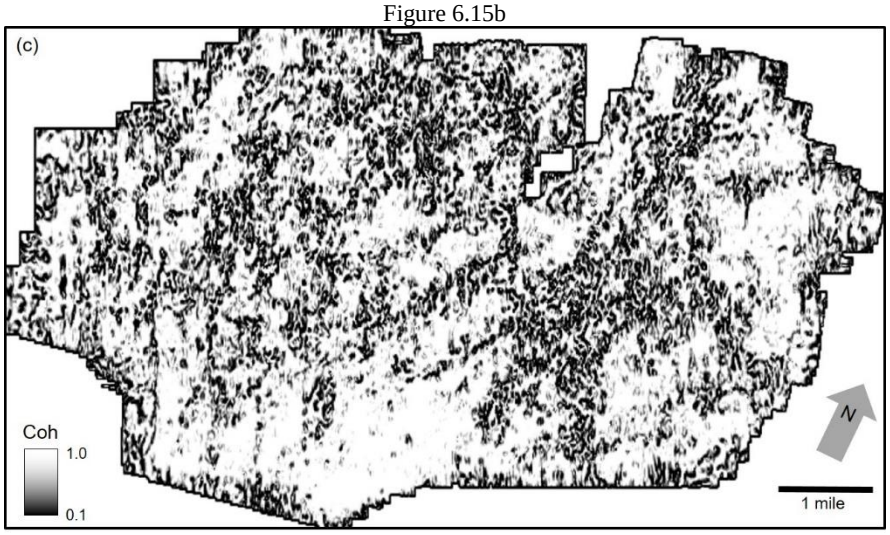

Figure 6.15c

Figure 6.15. Coherence slices at t=820ms of (a) original seismic data and filtered results from ICEEMD (b) as well as VMD (c). Note that less noise interference makes the attribute clearer.

REFERENCES

Bekara, M. and M. van der Baan, 2009. Random and coherent noise attenuation by empirical mode decomposition: Geophysics, **74**(5), V89-V98.

Berthouze, L. and S.F. Farmer, 2012. Adaptive time-varying detrended fluctuation analysis: Journal of Neuroscience Methods, **209**(1), 178-188.

Chen, Z., P.C. Ivanov, K. Hu, and H.E.Stanley, 2002. Effect of nonstationarities on detrended fluctuation analysis: Physical Review E, **65**(4), 041107.

Chkeir, A., C. Marque, J. Terrien, and B. Karlsson, 2010, Denoising electrohysterogram via empirical mode decomposition: PSSNIP Biosig. And Biorobot. Conf, 32-35.

Colominas, M. A., G. Schlotthauer, and M. E. Torres, 2014, Improved complete ensemble EMD: A suitable tool for biomedical signal processing: Biomedical Signal Processing and Control, **14**, 19–29.

Donoho, D. L., and J.M. Johnstone, 1994, Ideal spatial adaptation by wavelet shrinkage: Biometrika, **81**, 425-455.

Dragomiretskiy, K., and D. Zosso, 2014, Variational mode decomposition: IEEE Transactions on Signal Processing, **62**, 531-544.

Fang, Y. M., H. L. Feng, J. Li, and G. H. Li, 2011, Stress wave signal denoising using ensemble empirical mode decomposition and an instantaneous half period model: Sensors, **11**, 7554-7567.

Gan, Y., L. Sui, J. Wu, B. Wang, Q. Zhang, and G. Xiao, 2014, An EMD threshold denoising method for inertial sensors: Measurement, **49**, 34-41.

Gilles, J., 2013, Empirical wavelet transform: IEEE Transactions on Signal Processing, **61**(16), 3999-4010.

Han, J., and M. van der Baan, 2013, Empirical mode decomposition for seismic time-frequency analysis: Geophysics, **78**(2), O9–O19.

He, B., and Y. Bai, 2016, Signal-noise separation of sensor signal based on variational mode decomposition: In Communication Software and Networks (ICCSN), 8th IEEE International Conference on IEEE, 132-138.

Hestenes, M. R., 1969, Multiplier and gradient methods: Journal of Optimization Theory and Applications, **4**, 303–320.

Horvatic, D., H. E. Stanley, and B. Podobnik, 2011, Detrended cross-correlation analysis for non-stationary time series with periodic trends: EPL (Europhysics Letters), **94**, 18007.

Hu, K., P.C. Ivanov, Z. Chen, P. Carpena, and H.E. Stanley, 2001, Effect of trends on detrended fluctuation analysis: Physical Review E, **64**(1), 011114.

Huang, N. E., Z. Shen, S. R. Long, M. C. Wu, H. H. Shih, Q. Zheng, and H. H.Liu, 1998, The empirical mode decomposition and the Hilbert spectrum for nonlinear and non-stationary time series analysis: Proceedings of the Royal Society of London A: Mathematical, Physical and Engineering Sciences, **454**, 903-995.

Kabir, M.A. and C. Shahnaz, 2012. Denoising of ECG signals based on noise reduction algorithms in EMD and wavelet domains: Biomedical Signal Processing and Control, **7**(5), 481-489.

Lahmiri, S. and M. Boukadoum, 2014, October. Biomedical image denoising using variational mode decomposition: IEEE Biomedical Circuits and Systems Conference (BioCAS) Proceedings, 340-343.

Li, C., L. Zhan, and L. Shen, 2015. Friction Signal Denoising Using Complete Ensemble EMD with Adaptive Noise and Mutual Information: Entropy, **17**(9), 5965-5979.

Li, F., B. Zhang, R. Zhai, H. Zhou, and K. J. Marfurt, 2017, Depositional sequence characterization based on seismic variational mode decomposition: Interpretation, **5**(2), SE97-SE106.

Liu, W., S. Cao, and Y. He, 2015, Ground roll attenuation using variational mode decomposition: 77th Annual International Conference and Exhibition, EAGE, Extended Abstracts, Th P6 06.

Liu, W., S. Cao, and Y. Chen, 2016a, Applications of variational mode decomposition in seismic time-frequency analysis: Geophysics, **81**(5), V365-V378.

Liu, Y., G. Yang, M. Li, and H. Yin, 2016b, Variational mode decomposition denoising combined the detrended fluctuation analysis: Signal Processing, **125**, 349-364.

Mert., A., and A. Akan, 2014, Detrended fluctuation thresholding for empirical mode decomposition based denoising: Digital Signal Processing, **32**, 48-56.

Peng, C. K., S. V. Buldyrev, S. Havlin, M. Simons, H. E. Stanley, and A. L. Goldberger, 1994, Mosaic organization of DNA nucleotides: Physical review, **49**, 1685.

Rilling, G., P. Flandrin, and P. GoncalvGès, 2003, On empirical mode decomposition and its algorithms: IEEE-EURASIP Workshop on Nonlinear Signal and Image Processing, 3.

Schuster, G. T., 2007, Basics of Seismic Wave Theory: Notes for the Lecture Courses, University of Utah.

Torres, M. E., M. A. Colominas, G. Schlotthauer, and P. Flandrin, 2011, A complete ensemble empirical mode decomposition with adaptive noise: IEEE International Conference on Acoustics, Speech and Signal Processing (ICASSP), 4144–4147.

Verma, S., S. Guo, T. Ha, K. J. Marfurt, 2016, Highly aliased groundroll suppression using a 3D multiwindow KL filter: Application to a legacy Mississippi Lime survey: Geophysics, **81**(1), 1-10.

Wu, Z., and N. E. Huang, 2009, Ensemble empirical mode decomposition: A noise-assisted data analysis method: Advances in Adaptive Data Analysis, **1**, 1–41.

CHAPTER 7
CONCLUSIONS

In this dissertation, I analyse the information provided by both traditional Fourier transform and most recently introduced variational mode decomposition techniques. Fourier components provide a measure of enhancing discontinuities and estimating attenuation. In Chapter 1, I use spectral decomposition to highlight stratigraphic edges not seen in the original broad-band data. Combining covariance matrices to generate multi-spectral coherence provides improved images over traditional broad-band coherence images. In Chapter 2, I use spectral components to compute a novel frequency shift method for *Q* estimation built on time variant estimates of the dominant and central frequencies. The statistical analysis and application to both the synthetic data and field data calibrate the effectiveness of the proposed method. In Chapter 3, I showed how one can improve *Q* estimation by first correcting the spectra for elastic effects. I applied the correction to synthetic and field examples, and found *Q* values computed using the corrected spectra have less variability and fewer negative values than those computed using uncorrected spectra. In Chapter 4, I apply a suite of seismic attenuation attributes to both conventional and unconventional field data to detect hydrocarbons and delineate fracture system. The attributes appear to be useful for both seismic interpretation and reservoir characterization. In Chapter 5, I developed a variational mode decomposition algorithm to better map depositional sequences. The resulting components provided images amenable to detailed sequence stratigraphic interpretation. In Chapter 6, I showed how variational mode decomposition algorithm can be used to denoise seismic data.